

**EXPLORING ANALOGIES BETWEEN  
GRANULAR MATERIALS AND FLUIDS**

by

**Isabel Margarita Figueroa Amenábar**

Magister en Ingeniería Química, Universidad Técnica Federico  
Santa Maria, Chile, 2005

Ingeniero Civil Químico, Universidad Técnica Federico Santa  
Maria, Chile, 2005

Submitted to the Graduate Faculty of  
the Swanson School of Engineering in partial fulfillment  
of the requirements for the degree of

**Doctor of Philosophy**

University of Pittsburgh

2009

UNIVERSITY OF PITTSBURGH  
SWANSON SCHOOL OF ENGINEERING

This dissertation was presented

by

Isabel Margarita Figueroa Amenábar

It was defended on

September 22, 2009

and approved by

Joseph J. McCarthy, Associate Professor

J. Karl Johnson, Professor

George E. Klinzing, Professor

Laura Schaefer, Associate Professor

Dissertation Director: Joseph J. McCarthy, Associate Professor

# EXPLORING ANALOGIES BETWEEN GRANULAR MATERIALS AND FLUIDS

Isabel Margarita Figueroa Amenábar, PhD

University of Pittsburgh, 2009

The direct application of fluid-system approaches to particles oftentimes leads to spectacular failures; e.g. shaking mixes miscible fluids, while it can result in extreme segregation of particles. Nevertheless, much can be learned through analogies between these disparate systems and here we adapt concepts from fluid behavior and explore their application in industrially-relevant particle processes—such as mixing/segregation, heat transfer and flowability.

Adhesion is commonly found in operations involving fine powders and strongly impacts mixing/segregation of these materials. We develop both a Particle Dynamics (PD) model capable of simulating dry adhesive interactions as well as a characterization tool—the van der Waals Granular Bond Number. Using these tools we predict the asymptotic state of materials in a mixing drum and subsequently test these predictions.

Beyond predicting the asymptotic state of a system, the next natural step is to explore controlling that state. With this purpose, we propose the addition of “helper” particles to either promote mixing or segregation. These amphiphilic helper particles—also called Janus particles—act as bridges between the base particles, alternatively promoting mixing in a system that would otherwise segregate (surfactant helpers) or separating a specific kind of particle from a mixture (extractant helpers). Again, predictions are made and then tested against results obtained by simulation.

The presence of adhesive forces in granular materials can also affect the flowability of a granular material. Flow aids are frequently added to dry cohesive powders to improve their flow properties/handling, but are identified purely on an *ad hoc* basis industrially. Using our PD model and characterization tools, flow aids are, instead, rationally designed.

Finally, we study heat transfer within granular materials. Specifically, we examine the conditions necessary to achieve conduction-dominated versus convection-dominated heat transfer. Interestingly, when conduction is the dominant mechanism, increasing the mixing rate seems to have a positive impact on the heating rate, while under convection-dominated conditions the opposite is often true. Dimensionless numbers are used to correlate the results and a surprising degree of similarity is found when compared to analogous fluid correlations.

**Keywords:** granular materials, mixing, segregation, adhesion, flowability, heat transfer mechanisms.

## TABLE OF CONTENTS

<b>PREFACE</b> . . . . .	xiv
<b>1.0 INTRODUCTION</b> . . . . .	1
<b>2.0 BACKGROUND</b> . . . . .	5
2.1 Particle Dynamics . . . . .	5
2.1.1 Adhesive forces . . . . .	8
2.1.1.1 Normal impact of adhesive particles . . . . .	12
2.1.1.2 Tangential impact of adhesive particles . . . . .	14
2.1.1.3 Collision tests . . . . .	19
2.1.2 Thermal Particle Dynamics . . . . .	22
2.1.3 Method of quaternions . . . . .	24
2.2 Mixing and mixing measures . . . . .	28
2.2.1 Mixing and segregation . . . . .	28
2.2.1.1 Segregation mechanisms . . . . .	28
2.2.1.2 Practices to avoid segregation . . . . .	30
2.2.1.3 Segregation studies . . . . .	31
2.2.2 Mixing measures . . . . .	32
2.2.2.1 Intensity of Segregation . . . . .	33
2.2.2.2 Lacey mixing index . . . . .	33
2.2.2.3 Poole mixing index . . . . .	33
2.2.3 Poincare sections . . . . .	34
<b>3.0 PREDICTING MIXING AND SEGREGATION OF ADHESIVE GRAN- ULAR MATERIALS</b> . . . . .	37

3.1	Theory . . . . .	37
3.1.1	Granular Bond number . . . . .	37
3.1.2	Phase diagrams . . . . .	38
3.2	Tumbler Simulations . . . . .	43
3.2.1	PD simulations vs. phase diagram prediction: systems $\beta > 0.5$ . . . . .	45
3.2.2	Effects of adhesion in tumbler simulations: systems $\beta = 0.5$ . . . . .	46
3.3	Conclusions . . . . .	53
<b>4.0</b>	<b>CONTROLLING MIXING AND SEGREGATION OF ADHESIVE GRANULAR MATERIALS . . . . .</b>	<b>57</b>
4.1	Theory . . . . .	58
4.1.1	Granular Bond Number for binary systems with Janus beads . . . . .	58
4.1.2	Phase Diagrams . . . . .	59
4.1.3	Selection of Janus Beads properties . . . . .	62
4.2	Tumbler Simulations . . . . .	67
4.2.1	Extractant particles . . . . .	69
4.2.2	Surfactant particles . . . . .	75
4.3	Conclusions . . . . .	78
<b>5.0</b>	<b>FLOW AIDS . . . . .</b>	<b>80</b>
5.1	Theory . . . . .	81
5.1.1	Granular Bond number . . . . .	81
5.1.2	Phase Diagrams . . . . .	82
5.2	PD Simulations . . . . .	83
5.2.1	Hopper simulations . . . . .	83
5.2.2	Tumbler simulations . . . . .	86
5.3	Conclusions . . . . .	93
<b>6.0</b>	<b>MIXING AND HEATING IN GRANULAR MATERIALS . . . . .</b>	<b>94</b>
6.1	Mixing rate analysis . . . . .	95
6.1.1	Measuring radial mixing . . . . .	96
6.1.2	Analyzing heating mechanisms . . . . .	98
6.1.3	Apparent heat transfer coefficient . . . . .	101

6.1.4 Heating and mixing rate . . . . .	104
6.1.5 A scaling attempt . . . . .	106
6.2 Mixing topology and heat transfer . . . . .	109
6.3 Conclusions . . . . .	112
<b>7.0 SUMMARY AND OUTLOOK . . . . .</b>	<b>115</b>
7.1 Mixing & segregation . . . . .	116
7.2 Heat transfer . . . . .	117
7.3 Flowability . . . . .	119
<b>APPENDIX. NOTATION . . . . .</b>	<b>120</b>
<b>BIBLIOGRAPHY . . . . .</b>	<b>124</b>

## LIST OF TABLES

1	Van der Waals Granular Bond numbers for cases <i>b</i> , <i>e</i> , <i>f</i> , <i>h</i> and <i>i</i> . . . . .	45
2	Van der Waals Granular Bond numbers for cases <i>a</i> , <i>c</i> , <i>d</i> , and <i>g</i> . . . . .	56
3	Summary of Granular Bond Numbers for systems containing Janus Particles .	60
4	PD simulation parameters for tumbler simulations . . . . .	67
5	Summary of Granular Bond Numbers for systems containing Janus Particles .	68
6	Granular Bond numbers for systems containing flow aids (1 is host powder, <i>a</i> is conditioner powder). . . . .	82
7	Summary of Granular Bond number values for uniform systems (1) with flow aids ( <i>a</i> ). . . . .	88
8	Computational rates of mixing, $k_{mix}[s^{-1}]$ . . . . .	98
9	Regression values for correlations of curves in Figure 41. . . . .	104
10	Apparent heat transfer coefficient, $h_T$ in $[W/m^2K]$ , and Péclet numbers for both glass and aluminum particle simulations at 5 and 18 [rpm]. . . . .	108
11	TPD simulation parameters and mixing rates. . . . .	109

## LIST OF FIGURES

1	Forces in a particle-particle contact. . . . .	7
2	(a) Contact radius between two spheres in absence ( $a_0$ ) and in presence ( $a_1$ ) of adhesion under a normal load equal to $F_n$ . (b) Stress distribution in the contacting surfaces. Distribution A is the Hertz stress for $F_n = F_1$ and respective contact area $a_1$ . Distribution B is the actual stress distribution for $F_n$ . Distribution C is the Hertzian distribution for a contact radius $a = a_1$ (Ref. [74]) . . . . .	11
3	Adhesive normal force $F_n$ versus normal approach $\eta$ : (a) Initial contact point where $\eta = 0$ and $F_n = -\frac{8}{9}F_c$ ; (b) Yield point, $\eta_y$ is determined by equation 2.18; (c) and (d) are maximum elastic and plastic normal force, respectively, (e) Maximum attractive force, $F_n = -F_c$ ; and (f) Point of contact breakage, $F_n = -\frac{5}{9}F_c$ and $\eta = \eta_P$ . . . . .	15
4	Peeling and sliding failure. . . . .	16
5	Force-displacement curve for normal impact of elastic (thin line) and plastic (thick line) contacts with adhesion. Particle snapshots depict the particle overlapping (normal approach) and arrows indicate the relative magnitude and direction of the normal force. . . . .	20
6	Force evolution for tangential plastic collisions with impact angles $15^\circ$ , $30^\circ$ , $45^\circ$ , $60^\circ$ , and $75^\circ$ for non-adhesive (thin line) and adhesive (thick line) particles	21
7	Contact damping for (a) a normal impact, (b) a tangential impact. . . . .	23
8	Non-symmetric particle rotation during a tangential collision. . . . .	25
9	Segregation mechanisms. . . . .	29

10	Schematic picture of half-filled rotating tumbler showing the shear layer (grey), its thickness ( $\zeta$ ) and length ( $L$ ). The free surface forms a $\chi$ angle with the horizontal. . . . .	34
11	Three possible interactions in a binary system characterized by $Bo_{vdw_{11}}$ , $Bo_{vdw_{22}}$ , and $Bo_{vdw_{12}}$ . . . . .	39
12	Schematic phase diagram showing regions where interactions 1-1, 2-2 and 1-2 predominate. . . . .	41
13	Phase diagrams exhibiting E (Enhanced segregation) and M (Mitigated Segregation) phases for density ratio (a) $\alpha = 0.52$ , (b) $\alpha = 1.00$ , and (c) $\alpha = 1.92$	42
14	Mixing progress for tumbler cases $e$ and $f$ ( $\bullet$ and $\blacksquare$ , respectively) and the corresponding free-flowing case ( $\Delta$ ). The tumbler snapshots at the bottom corresponds to the mixing state after 5 revolutions. . . . .	47
15	Intensity of Segregation for cases $h$ and $i$ ( $\bullet$ and $\blacksquare$ , respectively) and the corresponding free-flowing case ( $\Delta$ ). . . . .	48
16	Intensity of Segregation for case $b$ ( $\bullet$ ) and its corresponding free-flowing counterpart ( $\circ$ ). . . . .	49
17	Mixing progress for systems corresponding to case $a$ with low ( $\bullet$ ) and high ( $\blacksquare$ ) degree of adhesion and the corresponding free-flowing case ( $\Delta$ ). . . . .	51
18	Intensity of Segregation for case $c$ and all related cases. . . . .	52
19	Mixing progress for tumbler case $d$ with different degrees of adhesion (freeflow ( $\Delta$ ), base case ( $\bullet$ ) and more adhesion ( $\blacksquare$ )). . . . .	54
20	Mixing progress for tumbler case $g$ with different degrees of adhesion: freeflow ( $\Delta$ ), base case ( $\bullet$ ) and more adhesion ( $\blacksquare$ ). . . . .	55
21	The strength ( $Bo_{iJj}$ ) of a Janus particle interaction is calculated as the weakest interaction where the bridge can break. . . . .	59
22	Phase-space diagrams for van der Waals adhesive systems with Janus beads. The binary phase-space diagram shows in grey the region corresponding to the materials that tend to mix and closed symbols have been placed if Janus can be used as extractant ( $\blacktriangleright$ ). The white region indicate systems that tend to segregate and open symbols cover the Janus surfactant ( $\circ$ ) region. . . . .	63

23	Density-size feasible values for extractant (left) and surfactants (right) Janus particles for binary systems chosen in Figure 22, respectively. Open circles indicate the existence of functional (extractant/surfactant) Janus particles with those density and size properties, if surface energies are chosen appropriately. In each case, a closed symbol indicate the properties chosen for PD simulations.	65
24	Allowed values of surface energies for extractant (left) and surfactant (right) Janus particles for systems shown in Figure 22. These $\phi_A$ - $\phi_B$ values correspond the surface energy ratios that will lead to functional particles with the densities and sizes selected in Figure 23.	66
25	Intensity of Segregation and tumbler snapshots for system <i>a</i> . Snapshots for adhesive without Janus particles [○] and systems with Janus particles when the initial state is mixed [●] and segregated [■].	70
26	Intensity of Segregation and tumbler snapshots for system <i>b</i> . Snapshots adhesive without Janus particles [□] and systems with Janus particles when the initial state is mixed [●] and segregated [■].	71
27	System <i>c</i> : Intensity of Segregation and respective snapshots for adhesive case without Janus particles [○] and with Janus particles [●].	72
28	System <i>c</i> : Intensity of Segregation and respective snapshots for system <i>c</i> with less [■], base [●] and more [▶] Janus particles.	73
29	Intensity of Segregation for system <i>e</i> and respective snapshots for adhesive case without Janus particles [○] and with Janus particles [●].	76
30	Intensity of Segregation and tumbler snapshots for system <i>f</i> . Snapshots for adhesive without Janus particles [○] and systems with Janus particles when the initial state is mixed [●] and segregated [■].	77
31	Flow aid phase diagram for density ratio $\alpha$ equal to 0.5, 1.0 and 2.0, respectively. Darker shades of grey indicate regions where better mixing is expected. Contour lines showing the flowability values (lower $\mathfrak{R}_3$ , higher ability to flow) are shown as dotted lines.	84

32	Hopper discharge simulation: Particles are randomly placed inside the device and let to be settled. The orifice is open and material starts to flow. The angle of repose of the remaining heap is used to asses the cohesiveness of the material.	85
33	Heaping result for pure host powder (left, AOR = 24°), with aids D (center, AOR = 19°) and B (right, AOR = 21°).	87
34	Heaping result for host with 25% (left) and 33% (right) aids D.	87
35	Dynamic angle of repose for host powder with aids <i>E</i> (center), <i>A</i> (top), <i>D</i> (bottom). From left to right the content of aids increases from no-aids to pure aids.	91
36	Dynamic angle of repose for systems containing aids <i>A</i> , <i>C</i> <sub>1</sub> , <i>C</i> <sub>2</sub> , <i>C</i> <sub>3</sub> . As value of $\mathfrak{R}_3$ increases, the flow properties of the mixture deteriorate.	92
37	System with aids B: as the drum tumbles, the host and the aids particles (originally pre-mixed) start segregating, and the aid particles become inefficient.	93
38	Schematic of a rotating cylinder with heat exchange at the wall, showing the definition of the shear layer thickness $\delta$ . The shear layer defines the region within the bed where the main motion of the particles is taking place (heat advection region), and defines the boundary from the region of solid-body rotation (heat conduction region). Representative streamlines, the coordinate system and the relevant system parameters are also shown.	97
39	Variation of the Intensity of Segregation with different rotation rates at constant filling degree $f = 0.37$ and $f = 0.5$ . For a half filled tumbler $f = 0.5$ , the circulation time of the material in the bed is independent of radial position thus mixing takes place at a very low rate. In contrast, for less than half filled drums ( $f \rightarrow 0$ ), the circulation time varies with radial position and therefore mixing is more rapid [160].	99
40	Variation of the bulk temperature in a rotating tumbler a three different extents of filling. The bulk temperature within the drum varies in a logarithmic fashion, although the local temperature evolution of individual particles is highly nonlinear. The rate of change is dependent on both the filling level ( $f$ ) and the rotation rate ( $\Omega$ ).	100

41	Logarithmic heating curves for systems with low (left) and high (right) values of Péclet. This figure shows cases where the conductance between the bed particles and the wall is negligible ( $H_{CWP}/H_{CPP} = 0.01$ ), comparable to ( $H_{CWP}/H_{CPP} = 1$ ) and larger than ( $H_{CWP}/H_{CPP} = 100$ ) the conductance between in-bed particles. . . . .	103
42	Apparent heat transfer coefficient for (a) glass and (b) aluminum particle simulations as a function of the mixing rate (left) and the wall-particle collision time (right). Two different tumbler rotation rates are shown: 5 [rpm] ( $\circ$ ) and 18 [rpm] ( $\bullet$ ), as are several tumbler geometries (see symbol shape; noting that the ellipse with a vertical line has an axis ratio of 0.7, with a horizontal line has a ratio of 0.5, and no line corresponds to a ratio of 0.6). . . . .	105
43	Nusselt vs. Péclet number for aluminum (left) and glass (right) particle systems for a tumbler rotation rate of 5 and 18 [rpm] and several tumbler geometries (see symbol shape). . . . .	107
44	Mixing and heat conduction in drums with different cross section. Poincaré sections from continuum model (center column). Computational heat transfer snapshots and contour plots using TPD for glass particles (right columns) and aluminum particles (left columns). Note that the colors in all thermal plots denote varying dimensionless particle temperature (see top scale). . . . .	110
45	Temperature profile along three different tumbler radial planes for aluminum (top) and glass (bottom) particle simulations. The combination symbol (open and filled) denotes a plane perpendicular to the free surface (i.e., vertical); while the open and filled symbols, respectively, denote planes $\pm 45^\circ$ (circle and square) or $\pm 60^\circ$ (ellipse) with respect to the free surface. . . . .	113

## PREFACE

I would like to thank my research advisor, Dr. Joseph McCarthy, for his guidance, encouragement, infinite patience, countless ideas and suggestions during the completion of this project. Especially, I thank him for sharing his enthusiasm for research with his students, and for teaching me how we can always learn from our results even when they are not what we expected. I thank Dr. George Klinzing for his constant support since I came to Pitt and the members of my dissertation committee—Dr. Karl Johnson, Dr. Klinzing and Dr. Shaefer—for their valuable comments about my work. I thank my current and past colleagues at the Granular Transport Group for the time and ideas shared.

My deep gratitude goes also to my friends at Pitt who always made me feel at home, and to Matthias for his unconditional loyalty. Most of all, I would like to thank my parents, Isabel Amenábar and Alejandro Figueroa, for showing me the value of education, the immense power of hard work and the beauty of doing something you enjoy. This dissertation is dedicated to them.

## 1.0 INTRODUCTION

Processing and handling of granular materials is a crucial operation in a wide variety of industries (cosmetics, powder metallurgy, abrasives, manufacture of solid rocket propellants, solid state combustion ceramics, etc.): approximately one half of the products and more than three quarters of the raw materials used in chemical industries are in granular form [1]. A better understanding of the phenomena governing their behavior could dramatically change the analysis and design of industrial operations such as packing, tableting, conveying, crushing, granulating, separation, coating, drying, multiphase reactions, fluidization, storage [2]. For example, mixing of powders is critical in industries such as pharmaceutical [3] and food [4]. Moreover, operations like the calcining of minerals and the drying of fruits or grains involve two or more simultaneous transport processes—transfer of heat within the granular materials, mass transfer, chemical reactions, mixing [5].

Despite the fact that granular materials have been the focus of attention in the last several decades, a fundamental understanding of their behavior has not been reached. No universal set of equations are capable to describe them. When applicable, the continuum approach is the simplest method of description and consists of a set of governing partial differential equations that uses effective properties of the material instead of the absolute values (that apply for individual components). The continuum hypothesis is applied at large scales where the ‘control volume’ contains a large enough number of microscopic constituents for the macroscopic properties to be continuous. Effective properties not only can enable the use of the fundamental transport equations, but also introduces the use of dimensionless numbers—and their correlations—to compare, scale and estimate these phenomena in different systems.

However, because of the fluctuations in the inter-particle force network and the nonlinear nature of the contact interactions, the applicability of the continuum approach cannot be assured [6].

Granular materials can be considered ‘complex systems’. A complex system is one whose global behavior cannot be determined by studying the many units and interactions that conform it individually; instead, they need to be studied collectively (*e.g.*, particle self-organization in segregating patterns [7, 8]). The fact that the intuition we have gained from our knowledge of fluids oftentimes lead us to incorrect guesses does not prevent us from using techniques and strategies originally developed for continuum media to study granular materials. Perhaps the most obvious and successful example is the use of kinetic theory. In gas-kinetic theory, molecules are assumed to move randomly at speeds that depend on the gas temperature. The kinetic theory approach for granular materials is based on the analogy between the molecules in a gas and the grains conforming a powder. When the flow is fast enough, the velocity of the particles can be approximated by a continuous distribution [9, 10]. Variations of each particles’s velocity from the average are related to the ‘granular temperature’ [10] because they reflect the kinetic energy of the flow. This theory have been used to estimate thermal conductivity [11, 12], viscosity [13], self-diffusivity [12], and develop equations of state [14].

Mixing two dissimilar materials is not a trivial operation: segregation can exist when particles differ in any physical property. Segregation is a major problem in industries that rely on the creation of granular mixtures. In the pharmaceutical industry, for example, a batch that cost hundreds of thousands of dollars can be rejected if the composition of as few as five tablets do not meet the FDA requirements [15]. Moreover, investing more and more energy in the process may have a counterintuitive result: more energy could lead to more segregation [16, 17]. A substantial amount of the work in this field has been devoted to find strategies to avoid segregation rather than understand its causes [18]. Reducing or increasing the particle size, modifying the handling/operating equipment are common practices to mitigate segregation. Adding a small amount of liquid can help by reducing the relative movement of particles through the introduction of capillary cohesive forces between particles. Cohesion can also exist in dry granular materials. If the particle size is relatively

small, van der Waals interactions may prevail and govern the granular flow. In Chapter 3, we will aim to understand and predict when a granular material of this kind mixes or segregates. In the following chapter, we will propose a strategy to control this asymptotic state based on adding mixing/segregating “helper” particles (Chapter 4).

The angle of repose (AOR) of a granular material is the maximum stable slope that a pile can have before the material starts sliding. A granular material whose surface angle is lower than the material’s AOR behave as a solid: there is no relative movement of grains even when the gravitational force exerts a stress on its surface. Conversely, if the surface angle of the pile is a few degrees above the angle of repose, particles on the surface start to flow [19]. The AOR seems to determine the transition from one behavior to the other and also indicates the degree of cohesiveness of the material. In general, a more ‘flowable’ (less cohesive) powder will exhibit a lower surface slope and a less ‘flowable’ material, a steeper slope. Our aim in Chapter 5 is to engineer aid particles capable of manipulating the degree of “flowability” of the material, i.e. change its repose angle.

Industrially, powders can be mixed not only to create a granular mixture but also to favor transport of heat or mass or to achieve faster kinetics of a multiphase chemical reaction, as is commonly done with fluids. Heat transfer in fluidized bed [20, 21, 22, 23, 24], dryers [25, 26, 27, 28], rotary reactors and kilns [29, 30, 31], packed beds [32, 33, 34] have extensively been studied to understand mechanisms and to obtain estimates of heat transfer coefficients. The magnitude of the heat exchanged depends on the thermo-physical properties of the particles and the walls, the interstitial fluid, the shape of the particles and the contact time [35], among other variables. Depending on the process and material variables, heat transfer between heated surfaces and particles in motion may be dominated by contact conductance. This process constitutes one of the basic mechanisms of heat transfer in particulate systems [36]. In Chapter 6, we focus on the problem of heat transfer encountered in a rotating tumbler when the granular material is heated from the walls. Our goal is to understand the role of advection in the overall heating process.

The lack of a comprehensive theory has promoted the advance of numerical simulations in the field of granular materials. A big part of the work presented in the following chapters was carried out using a simulation methodology we call Particle Dynamics (PD). PD is a

Molecular Dynamics based simulation technique that (in the simplest case) considers purely mechanical interactions between the grains that form the granular material. The motion of each of the particles or grains is governed by Newton’s law and the key of this methodology is the calculation of the appropriate inter-particle forces. The main drawback of PD is that is computationally expensive: the estimated maximum number of particles that can be simulated is  $10^4$  [37] while a typical industrial device has at least  $10^9$  particles [38]. Therefore, the real challenge when using PD is to design meaningful sets of computational experiments to develop useful models and predicting tools.

This dissertation is organized in the following manner. Chapter 2 lays the background on the simulation methodology and fundamentals about mixing and segregation. Chapter 3 describes the use of scaling arguments to build phase diagrams to predict the mixed/segregated asymptotic state of binary mixture of dry-cohesive (also called in this document, ‘adhesive’) granular materials. The following chapter proposes a novel strategy to control this asymptotic state by using of mixing/segregating aids. These aids—also called ‘Janus particles’—can act as *surfactants* promoting mixing of two phases that are otherwise immiscible, or as *extractants* to recover one component from a mixture. In Chapter 5, we explore the use of aid-particles to control the flowability of granular materials. In liquids, better mixing usually means larger heat transport coefficient. Chapter 6 studies how mixing affects heating rates in granular materials. Finally, Chapter 7 discusses the outlook of this work.

## 2.0 BACKGROUND

### 2.1 PARTICLE DYNAMICS

Particle Dynamics (PD) has emerged as a successful Discrete Element Method (DEM) simulation technique for modeling granular flows [39, 40, 41, 42, 43, 44, 45, 46, 47, 48, 49, 50, 51, 52] giving insight to such diverse phenomena as force transmission [53], agglomerate formation and breakage [54] and segregation of cohesionless materials [55]. In PD, the global flow of the granular material is determined by the time evolution of the trajectory of each individual particle governed by Newton’s second law of motion. The equations that describe the particle motion are:

Linear Motion:

$$m_p \frac{d\vec{v}_p}{dt} = -m_p \vec{g} + \vec{F}_n + \vec{F}_t \quad (2.1)$$

Angular Motion:

$$I_p \frac{d\vec{\omega}_p}{dt} = \vec{R} \times \vec{F}_t \quad (2.2)$$

where  $m_p$  is the particle mass,  $I_p$  is its moment of inertia,  $R$  is its radius and  $\vec{F}_n$  and  $\vec{F}_t$  are the inter-particle forces—normal and tangential, respectively—acting on the particle (See Figure 1). Modeling the contact mechanics of the particle interactions is the core of PD and can be accomplished using two different approaches. The first uses a ‘hard sphere’ model [56] (also known as ‘event driven’ simulation) and assumes that all collisions are binary and take an infinitely short time. The velocities of the two colliding particles are then updated by using a restitution coefficient. The second approach, the ‘soft particle model’ [57], is the one that is used in this work and is capable of modeling multiple particle long-lasting collisions. This technique is more appropriate for slow, more dense flows. Its main drawback

is that, as the force models can be dramatically more complex, the simulations become more computationally expensive. While a variety of force models may be used [58, 59, 50, 51], in this work and for adhesionless systems, the normal interactions are computed from an elastic-plastic model [60]. For elastic contacts, or elastic-plastic contacts at early stages, the normal force,  $F_n^e$  is calculated as:

$$F_n^e = k_n^e \eta^{3/2}, \quad (2.3)$$

where  $\eta$  is the overlapping between particles given by  $\eta = S_{ij} - (R_i + R_j)$  ( $R_i, R_j$  are the particle  $i$  and  $j$  radii respectively). The elastic normal contact stiffness  $k_n^e$  is related to the mechanical properties (Young's modulus,  $E_i$ , and Poisson ratio,  $\nu_i$ ) by [61]:

$$k_n^e = \frac{4}{3} E^* \sqrt{R^*}, \quad (2.4)$$

where  $R^*$  and  $E^*$  are

$$\frac{1}{E^*} = \frac{1 - \nu_1^2}{E_1} + \frac{1 - \nu_2^2}{E_2} \quad (2.5)$$

$$\frac{1}{R^*} = \frac{1}{R_1} + \frac{1}{R_2} \quad (2.6)$$

respectively. After the normal force reaches the yield point [62], plastic deformation occurs and the plastic normal force ( $F_n^p$ ) is calculated using:

$$F_n = F_y + k_n^p (\eta - \eta_y). \quad (2.7)$$

In this expression,  $\eta_y$  is the overlapping at the point of yield,  $k_n^p$  is the plastic normal stiffness, which is related to the yield force by  $k_n^p = (2/3)(F_y/\eta_y)$ , and  $F_y$  is the normal force between the particles when the yield stress is reached. If the contact unloading starts before the yield point is reached, particles bounce back with no energy dissipation according to equation 2.4 and 2.3. Unloading after the yield limit is given by

$$F_n^p = F_{nmax} - k_n^e \sqrt{\bar{R}} (\eta_{max} - \eta)^{3/2}, \quad (2.8)$$

where  $F_{nmax}$  and  $\eta_{max}$  are the maximum normal force and normal overlapping reached during

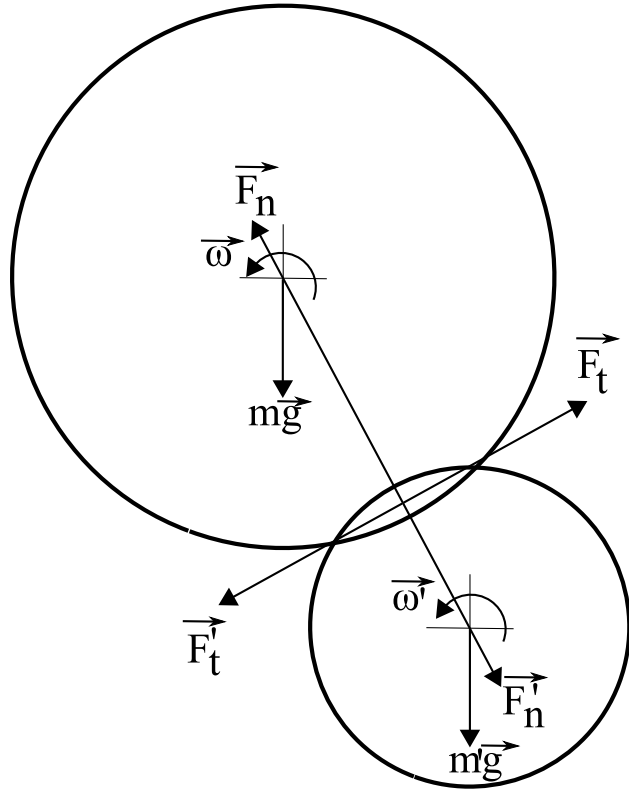


Figure 1: Forces in a particle-particle contact.

loading, respectively, and  $\bar{R}$  is the ratio of the new (local) contact radius of curvature after the plastic deformation has occurred,  $R^{*p}$ , to the initial effective particle radius  $R^*$ , that is,

$$\bar{R} = \frac{R^{*p}}{R^*} = \frac{F_y}{F_{nmax}} \left( \frac{2F_{nmax} + F_y}{3F_y} \right)^{3/2}. \quad (2.9)$$

The tangential or frictional force is derived from Walton and Braun [51, 63]. The tangential force acting at a particle-particle contact,  $F_t$ , is updated by

$$F_t = F_{told} - k_t \Delta\delta, \quad (2.10)$$

where  $F_{told}$  is the tangential force at the previous time step, and  $\Delta\delta$  is the displacement during the present time-step that is calculated from the component of velocity tangent to the contact surface,  $v_t$  (that is  $\Delta\delta = v_t \Delta t$  where  $\Delta t$  is the time-step). The frictional stiffness,  $k_t$ , depends on two history terms and is given by the non-linear expressions

$$k_t = k_{t_o} \left( 1 - \frac{F_t - F_t^*}{\mu F_n - F_t^*} \right)^\gamma, \quad \text{for increasing } F_t \quad (2.11)$$

$$k_t = k_{t_o} \left( 1 - \frac{F_t^* - F_t}{\mu F_n + F_t^*} \right)^\gamma, \quad \text{for decreasing } F_t. \quad (2.12)$$

where  $F_t^*$  is the tangential force value at the load reverse point. The first expression is used when the direction of the incremental change in the tangent force would result in an increase in the total  $F_t$  and the second corresponds to a decrease in  $F_t$ . This model is capable of mimic energy dissipation by micro-slip at the edge of the contact and sliding friction as described by Amoton's rule  $F_t \leq \mu F_n$ . The value  $\gamma$  is a constant which is typically set to (1/3) in agreement with Mindlin [64] and  $k_{t_o}$  is the initial tangential stiffness and is related to the Hertzian normal stiffness by

$$k_{t_o} = \frac{k_n(1 - \nu)}{1 - \nu/2}. \quad (2.13)$$

### 2.1.1 Adhesive forces

As we mentioned before, we will be studying fine granular materials where adhesive forces caused by electrostatic interactions are predominant. To the best of our knowledge, none

of the work focussed on modeling dry-adhesive interactions has aimed to study mixing and segregation. In this section, we describe different approaches that have been taken to model these kind of interactions in a variety of applications.

Much of the computational work focussed on dry-adhesive granular materials estimates the particle-particle interaction as a constant value [65] or a square-well potential [66]. The work of Alexander *et al.* [67] studies the avalanches of free-flow, wet-cohesive, and dry-cohesive powders and report how the latter present a different avalanching dynamics with respect to their wet counterparts: they present dilation, aperiodic avalanche frequencies and variable avalanches size. Their modeling work approximates the cohesive force to a constant value that can be tuned to agree with their experimental observations. The same approach in a different model was used by Gilbertson and Eames [68]. Interested in studying the effect of cohesion in fluidized beds of small particle sizes ( $\sim 4\text{-}6\ \mu\text{m}$ ), they used an increased value of stress between particles to model the effect of cohesion. Their results can reasonably predict the dynamics of these particle flows when cohesion is weak compared to drag or friction forces. Rhodes [69] used a similar strategy to model fluidized beds by DEM. The cohesive forces were adjusted to pin-point the region of onset of Geldart's [70] cohesive behavior, and focussed on how the flow changes by varying the particle size and density.

Weber and coworkers [66] also studied cohesive fluidized bed by DEM simulations. Their approach attempts to physically relate the square-well model with the Hamaker constant. They observed that at lower solids fractions, the presence of cohesive forces has little impact on the stress components. Rognon *et al.* [71] investigate the rheology (friction and dilation of the bed) of adhesive material by relating the cohesive force to a granular bond number, finding that increasing the cohesion of the material leads to its expansion. For high cohesion values, they observed the growth of heterogeneities (large voids separating dense granular areas), and an increase in the contact force anisotropy. Brewster *et al.* [72] chose a Gaussian well to simulate cohesive forces in an inclined flow. Using this model, they conclude that for cohesive materials the Bagnold scaling relation (the shear stress is proportional to the square of the rate of strain tensor and that the density is constant throughout the material) does not apply.

The main advantage of these formulations lies in their simplicity, in lower computational requirements and in capability to simulate larger (3D) systems in shorter computation times, etc; however, their parameters (for example, depth and width of the well) lack rigorous physical meaning and cannot predict the flow behavior of these materials from first principles. A notable exception is the work done by Severson [73] *et al.*, who used DEM to model a mechanical damping device based on micro or nano powder. Their model is based on the JKR theory and it is capable of mimicking some characteristic phenomena of adhesive contact as ‘peeling failure’ and ‘stretching contacts’. In the remainder of in this section, we describe the details of our computational model for dry-adhesive interactions. Based on the work of Johnson *et al.* [74] (i.e., JKR model), it models adhesive elastic spheres and assumes that the adhesion between particles results only in a change of surface energy over the contact areas; therefore, the attractive forces are of infinitely short range. The contact area (determined by the contact radius,  $a_1$ ) predicted by this model is larger than that predicted under the condition of no adhesion (contact radius,  $a_0$ ), as is shown in Figure 2, and results in an infinite tensile stress at the perimeter. This model leads to a finite negative load, i.e., pull-off force, that is required to separate the surfaces, given by  $F_c = 3\pi\Gamma R^*$ , where  $\Gamma$  is the surface energy of the particles.

An alternative model developed by Derjaguin *et al.* (DMT model) [75] instead argues that the adhesive normal forces should have a finite range outside the contact area. This model predicts a slightly larger pull-off force of  $F_c = 4\pi\Gamma R^*$ . Both models are complementary and apply to different regions of the adhesive solid-solid interactions that can be determined by a non-dimensional parameter, defined by Tabor [76],

$$\mu_T = \sqrt[3]{\frac{R^*\Gamma^2}{E^*\epsilon_0^3}} \quad (2.14)$$

where  $\epsilon_0$  is the interatomic equilibrium distance in the Lennard-Jones potential for solid-solid interactions. The JKR model is most appropriate for large values of the Tabor parameter, when soft materials with strong short-range adhesion are in elastic contact, while contacts between stiff materials with weaker attraction are better described by DMT [77].

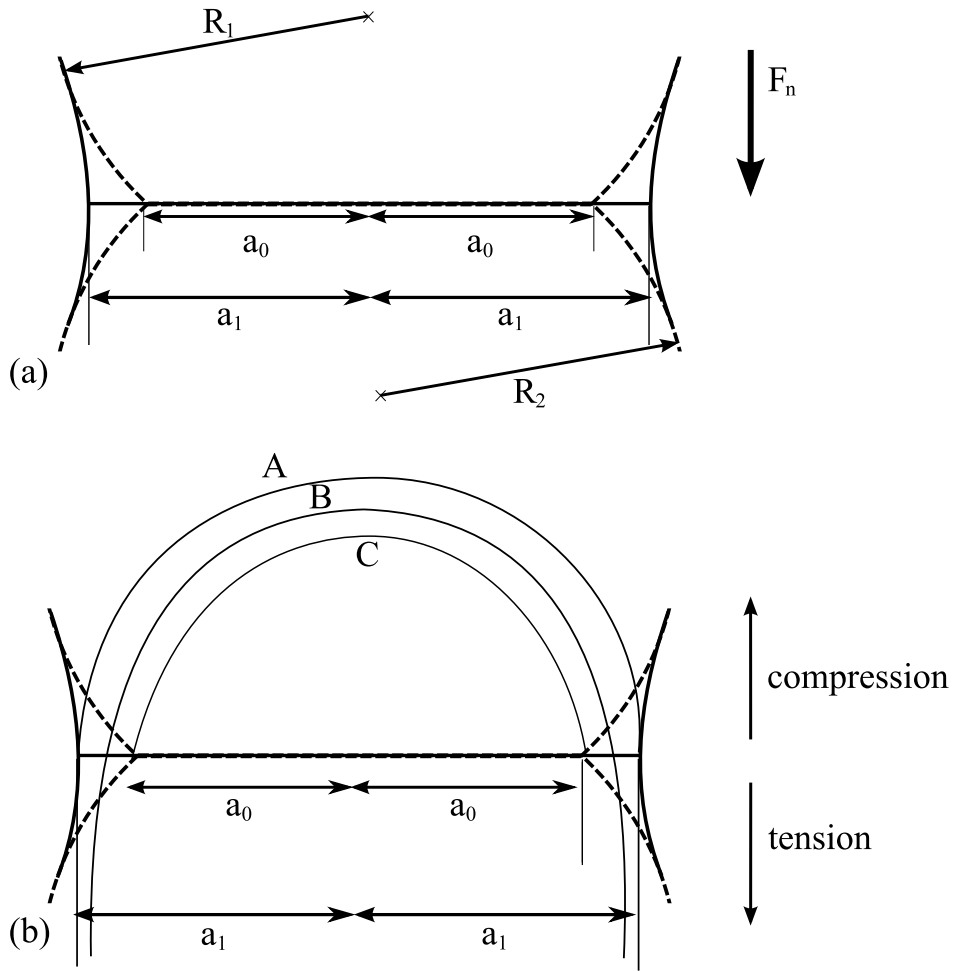


Figure 2: (a) Contact radius between two spheres in absence ( $a_0$ ) and in presence ( $a_1$ ) of adhesion under a normal load equal to  $F_n$ . (b) Stress distribution in the contacting surfaces. Distribution A is the Hertz stress for  $F_n = F_1$  and respective contact area  $a_1$ . Distribution B is the actual stress distribution for  $F_n$ . Distribution C is the Hertzian distribution for a contact radius  $a = a_1$  (Ref. [74])

The JKR model does not specify which short range interaction (forces of van der Waals, hydrogen bonding, steric forces, coulombic interactions, etc.) is the source of the surface energy. When van der Waals force are the source of adhesion, the surface energy, also called thermodynamic work of adhesion, can be obtained from the interaction laws for different geometries and the conventional Hamaker constant,  $A$ . For example: for two surfaces,  $\Gamma = A/24\pi D_0^2$  and for two spheres  $\Gamma = A/12D_0R^*$ . The value to be used as the interfacial contact separation,  $D_0$ , is not obvious; however, Israelachvili [78] estimates  $D_0$  as 0.16 [nm] (based on an energy balance) obtaining a remarkable agreement with measured values for a wide range of solids and liquids.

Savkoor and Briggs [79] addressed the effect of tangential forces on the size of the contact area and the normal contact stiffness. Thornton and Yin [80] combined the work of Savkoor and Briggs [79] and Mindlin and Deresiewicz [75] to describe the tangential behavior of elastic adhesive particles. A model for normal adhesive plastic collisions has been provided by Thornton and Ning [81]. In the following sections, we review how these theories are combined to form the force models we use in our PD simulations.

**2.1.1.1 Normal impact of adhesive particles** Before the yield stress is reached, particles in contact undergo elastic deformation. The elastic normal stiffness is given by:

$$k_n^e = \frac{dF_n}{d\eta} = 2E^*a \frac{3\sqrt{F_1} - 3\sqrt{F_c}}{3\sqrt{F_1} - \sqrt{F_c}} \quad (2.15)$$

The radius of the contact spot,  $a$ , is given as:

$$a = \sqrt[3]{\frac{3R^*F_1}{4E^*}} \quad (2.16)$$

where  $F_c$  is the pull-off force in the JKR model and  $F_1$  represents the effective Hertzian force which would produce the same contact area [54] in the absence of adhesion.  $F_1$  is given by

$$F_1 = F_n + 2F_c + \sqrt{4F_nF_c + 4F_c^2 - F_t^2E^*/4G^*} \quad (2.17)$$

where  $F_t$  is the magnitude of the tangential contact force. It should be noted that for non-adhesive contact (i.e.,  $\Gamma = 0$ ) equation 2.17 reduces to the elastic non-adhesive solution.

When the normal force increases beyond the yield point, plastic deformation occurs. First, the initial yield state is identified by testing whether the contact radius has reached the value associated with yield, given in the expression

$$\sigma_y = \frac{2E^*a_y}{\pi R^*} - \sqrt{\frac{2\Gamma E^*}{\pi a_y}} \quad (2.18)$$

where the subscript  $y$  represents the yield point, i.e.,  $\sigma_y$  is the yield stress. Then, the normal stiffness,  $k_n^p$ , for the subsequent plastic deformation is calculated using the contact stiffness at the yield point (point b in Figure 3), using

$$k_n^p = \frac{3\pi R^* \sigma_y \sqrt{F_1} - 2E^* a_y \sqrt{F_c}}{3\sqrt{F_1} - \sqrt{F_c}}. \quad (2.19)$$

The normal contact force,  $F_n$ , is updated using

$$F_n = F_{nold} + \Delta F_n = F_{nold} + k_n \Delta \eta, \quad (2.20)$$

both before and after the onset of yield where  $k_n$  is the corresponding elastic/plastic stiffness ( $k_n = k_n^e$ , if  $a < a_y$ ;  $k_n = k_n^p$ , if  $a \geq a_y$ ). Beyond the yield point, the adhesive plastic contact force,  $F_n$ , is continuously updated using equations 2.17 to 2.20 for each time step. Although in this stage the contact is plastic, the corresponding adhesive elastic force,  $F_n^e$ , that would be attained at the present level of deformation also needs to be computed since its maximum value (point c in Figure 3) will be used in the subsequent unloading calculations. Unloading of a contact that has not begun to plastically yield is purely elastic, so that equation 2.20 may be used ( $\Delta \eta$  now takes a negative value). Alternatively, the unloading stage beyond the yield limit is assumed to be elastic, except that the past plastic deformation has permanently altered the (local) radius of curvature. The new radius of curvature,  $R^{*p}$ , is given by

$$R^{*p} = \frac{R^* F_{1max}}{F_{max} + \sqrt{4F_c F_{1max} - F_t^2 E^* / 4G^*}}. \quad (2.21)$$

When  $4F_c F_{1max} - F_t^2 E^* / 4G^* < 0$ , an exception is made such that  $R^{*p} = \frac{R^* F_{1max}}{F_{nmax}}$ . This case corresponds to a discontinuity (peeling completion) in the tangential response that will be explained in the section 2.1.1.2.

Because of the change in apparent radius of curvature the post-yield unloading normal stiffness is changed and is now given by

$$k_{nU} = 2E^* a \frac{3\sqrt{F_{1U}} - 3\sqrt{F_{cU}}}{3\sqrt{F_{1U}} - \sqrt{F_{cU}}}, \quad (2.22)$$

where the subscript  $U$  stands for unloading. The contact radius, used in this expression, is given as

$$a = \sqrt[3]{\frac{3R^{*p}F_{1U}}{4E^*}}, \quad (2.23)$$

and here  $F_{1U}$  represents the effective Hertzian force for the unloading stage

$$F_{1U} = F_n + 2F_{cU} \pm \sqrt{4F_n F_{cU} + 4F_{cU}^2 - F_t^2 E^* / 4G^*} \quad (2.24)$$

with  $F_{cU}$  denoting the modified pull-off force,  $F_{cU} = 3\pi\Gamma R^{*p}$ . The positive sign in equation 2.24 becomes negative when the normal force reaches its lowest value,  $-F_{cU}$ , at point  $e$  in Figure 3. Note that in a purely normal contact the continuity of equation 2.24 is assured since the left term becomes zero when  $F_n = -F_{cU}$ . The case when  $F_t \neq 0$  is discussed in the next section. The contact breaks at  $\alpha_{nP}$ , where  $F = -\frac{5}{9}F_{cU}$  (point  $f$  in Figure 3).

**2.1.1.2 Tangential impact of adhesive particles** Savkoor and Briggs studied tangential collisions of adhesive spheres. In their analysis, which incorporates the JKR model into tangential contact mechanics [79], the tangential force primarily affects the behavior of colliding particles through changes in the contact radius. This effect is most apparent at the beginning stages of a collision, which corresponds to a “peeling” mechanism. This can be seen from the previously discussed equation 2.17. As the tangential force increases, the contact radius is reduced up to a critical value of  $F_t$ , given by

$$F_{tpeeling} = 4\sqrt{\frac{(F_n F_c + F_c^2)G^*}{E^*}} \quad (2.25)$$

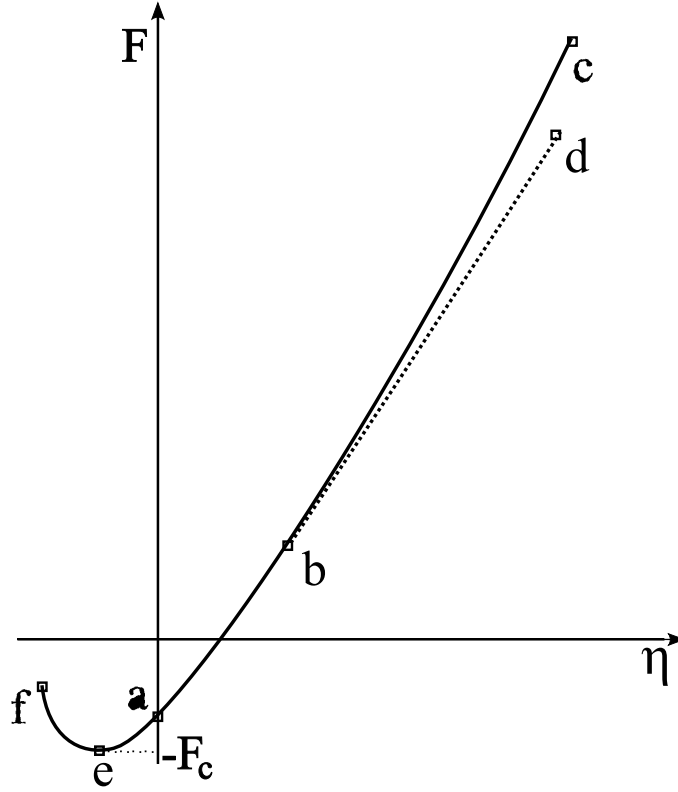


Figure 3: Adhesive normal force  $F_n$  versus normal approach  $\eta$ : (a) Initial contact point where  $\eta = 0$  and  $F_n = -\frac{8}{9}F_c$ ; (b) Yield point,  $\eta_y$  is determined by equation 2.18; (c) and (d) are maximum elastic and plastic normal force, respectively, (e) Maximum attractive force,  $F_n = -F_c$  ; and (f) Point of contact breakage,  $F_n = -\frac{5}{9}F_c$  and  $\eta = \eta_P$ .

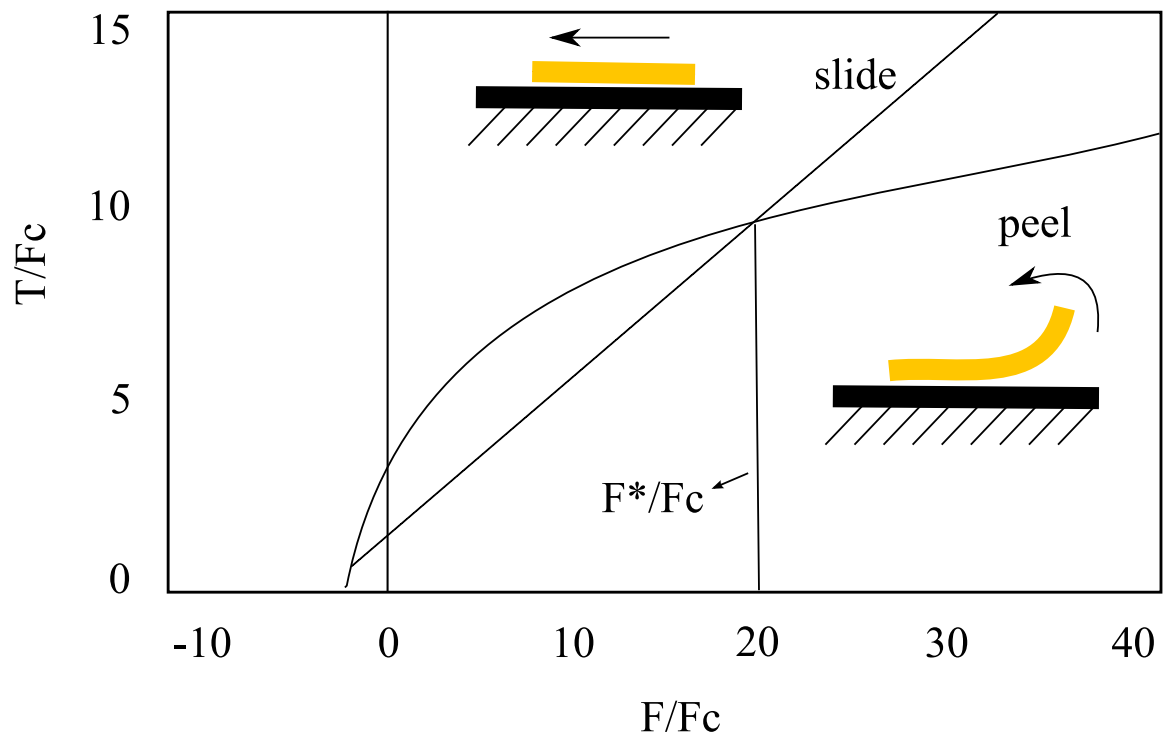


Figure 4: Peeling and sliding failure.

at which point the peeling process is considered complete and ‘peeling failure’ has occurred (Figure 4). After the contact has ‘peeled’, the radius of the contact area can be calculated from

$$a = \sqrt[3]{\frac{3R^*(F_n + 2F_c)}{4E^*}}. \quad (2.26)$$

In this work, the tangential contact stiffness is obtained following the procedure of Ref. [49] and is given by

$$k_t = 8G^*a\theta \pm \mu \frac{(1 - \theta)}{\Delta\delta} \quad (2.27)$$

with

$$\begin{aligned} \theta_L &= \left[1 - \frac{F_t + \mu\Delta F}{\mu F}\right]^{\frac{1}{3}} \\ \theta_U &= \left[1 - \frac{F_t^* - F_t + 2\mu\Delta F}{\mu F}\right]^{\frac{1}{3}} \\ \theta_R &= \left[1 - \frac{F_t - F_t^{**} + \mu\Delta F}{\mu F}\right]^{\frac{1}{3}}. \end{aligned} \quad (2.28)$$

The subscripts  $L$ ,  $U$  and  $R$  in equation 2.28 correspond to loading, unloading and reloading, respectively. The negative sign in 2.27 is only used for the unloading stage. The load reversal points  $F_t^*$  and  $F_t^{**}$  need to be continuously updated as  $F_t^* = F_t^* + \mu F_n$  and  $F_t^{**} = F_t^{**} + \mu F_n$  to account for the effect of varying normal force. In the case that the peeling criterion has not been satisfied, the contact stiffness is calculated setting  $\theta = 1$ . A detailed description can be found in Ref. [82]. Adhesion also changes the tangential failure criterion—sliding. Beyond the peeling limit, a further increase in tangential loading should (eventually) result in sliding. Savkoor and Briggs suggested that this transition would occur via immediate reduction of the contact radius to the Hertzian value,  $a = \sqrt[3]{3R^*F_n/4E^*}$ . In contrast, Thornton and Yin [49] suggested that the contact radius should vary smoothly at  $F_{tpeeling}$ ; therefore, the sliding criteria proposed in that work and used here, ensures a smooth transition in contact radius as the contact moves from peeling to sliding. The modified analysis proposed by Thornton yields multiple cases depending on the value of  $F_t$  necessary to reach the ‘peeling failure’.

In general, the onset of the ‘peeling failure’ is determined by equation 2.25, and the ‘sliding failure’ is reached when

$$F_t = \mu(F_n + 2F_c). \quad (2.29)$$

Both criteria, however, coincide when  $F_n = F^*$  (See Figure 4), where  $F^*$  is given by

$$F^* = 2F_c \left[ \left( \frac{4G^*}{\mu^2 E^*} - 1 \right) + \sqrt{\frac{4G^*}{\mu^2 E^*} \left( \frac{4G^*}{\mu^2 E^*} - 1 \right)} \right]. \quad (2.30)$$

This obviously leads to two separate possibilities. When the instantaneous value of  $F_n$  is such that  $F_n > F^*$ , the ‘peeling failure’ is reached earlier than the point where sliding would occur; thus, beyond that point a standard (non-adhesive) friction response is expected (i.e., development of a slip annulus, followed by a ‘sliding failure’—equation 2.29). If  $F_n < F^*$ , however, the tangential force at the point when the peeling failure criterion is met is greater than the magnitude of the force that would normally be required for sliding. Therefore, in this case, the tangential force beyond the peeling failure immediately jumps to the lower, sliding limit value. In order to achieve the objective of a continuous change in the contact radius, we must modify the sliding failure criteria slightly to

$$F_t = \begin{cases} \mu(F_n + 2F_c), & \text{if } F_n \geq -0.3F_c \\ \mu F_1 [1 - (F_1 - F_n)/3F_1]^{3/2}, & \text{if } F_n \leq -0.3F_c \end{cases} \quad (2.31)$$

This modification is required since, for small values of  $F_n$ , the contact spot obtained by strict observation of Eqn. 2.29 would result in a contact spot that included a tensile (as well as compressive) region despite the fact that peeling had already completed.

**2.1.1.3 Collision tests** Several particle collisions were simulated in order to validate the results of the adhesive contact mechanics in our code against the results found in the literature. The model for normal adhesive contact was validated using the work of Thornton and Ning [81] for elastic and plastic collisions. The force evolution for adhesive elastic tangential impacts was compared to the results obtained by Thornton and Yin [80]. In Figure 5, a normal elastic (thin line) and plastic (thick line) impact is compared for two particles ( $R = 100$  [ $\mu\text{m}$ ],  $\rho = 2650$  [ $\text{kg}/\text{m}^3$ ],  $E=70$ [GPa],  $\nu = 0.3$ ,  $\mu = 0.35$ ,  $\sigma_y = 0.3$ [MPa] and  $\Gamma=0.2$ [J/m<sup>2</sup>]). When particles are approaching, the adhesive forces do not come into play until the surfaces are in contact. In this loading stage, the particles can experience both a negative (attractive) and posteriorly positive (repulsive) normal force until the compression work reduces the kinetic energy to zero. During the unloading stage, particles can remain adhered because of a (negative) normal force at negative values of the approach (i.e., after contact of a rigid sphere would have ceased). This latter effect is observed due to the fact that the material at the contact will “stretch” slightly until the pull-off force is reached. In some cases, the kinetic energy of the particles at the moment of the impact may not be enough to overcome the work done by the adhesive force and the particles will not separate during unloading.

Next, the tangential interaction is tested using the same particle properties. Here, we simulate different collision angles for an impact velocity of  $\pm 0.5$  [m/s]. For the plastic case without (thin line) and with (thick line) adhesion, the force evolution is shown in Figure 6 ( $\Gamma = 0.2$  [J/m<sup>2</sup>] for the adhesive case). The discontinuity observed in the curve for higher impact angles ( $\geq 30^\circ$ ), corresponds to the occurrence of the peeling mechanism of failure. Beyond this point, the tangential force is large enough to cause the system to slide (straight line in the force curve). For a lower impact angle ( $15^\circ$ ), the tangential force is not large enough to promote angular motion of the particles because the contact never reaches the peeling limit so the adhesive interaction absorbs all of the torque.

As mentioned, in presence of adhesion, the attractive forces can prevent the particles of bouncing back. In the case of elastic contacts ( $F_{max} < F_y$ ), no energy is dissipated during a collision. If the impact velocity of the particles is smaller than the critical “sticking velocity” the contact force will oscillate continuously and equilibrium will never be reached.

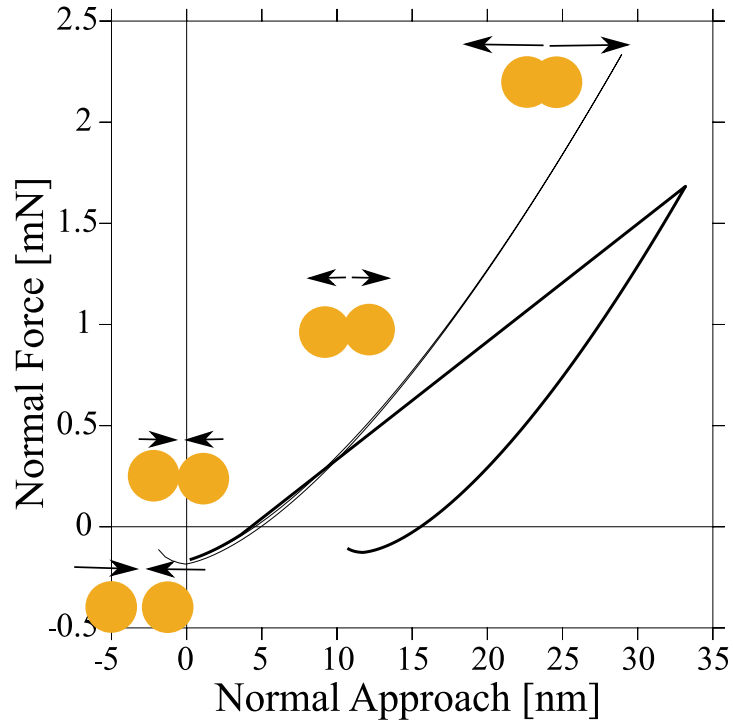


Figure 5: Force-displacement curve for normal impact of elastic (thin line) and plastic (thick line) contacts with adhesion. Particle snapshots depict the particle overlapping (normal approach) and arrows indicate the relative magnitude and direction of the normal force.

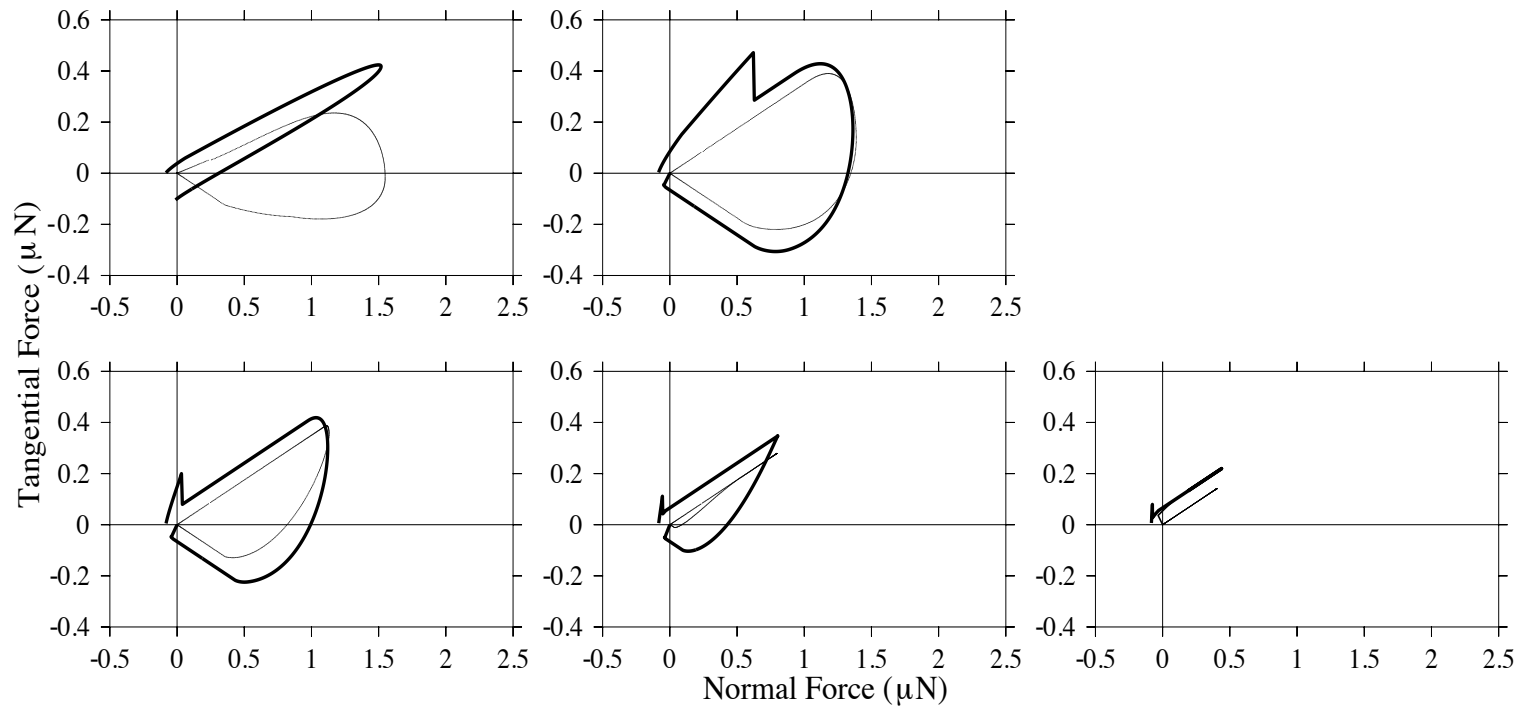


Figure 6: Force evolution for tangential plastic collisions with impact angles 15°, 30°, 45°, 60°, and 75° for non-adhesive (thin line) and adhesive (thick line) particles

In order to avoid this instability and physically mimic energy dissipation—for example, by sound—a contact damping term is added as:

$$\text{damping} = c_0 \frac{E^*}{1 - \nu^2} \quad (2.32)$$

where  $c$  is a constant and  $\nu$  is the Poisson ratio. Figure 7 shows the normal tangential and normal force evolution for a system with (continuous line) and without contact damping (dotted line). The impact velocity is 0.05 [m/s], the particle properties are the same as those in Figure 6, and the angle of impact for Figure 7b is 45°. The magnitude of the contact force progressively decreases with each oscillation until finally reaching equilibrium (contact forces are equal to zero) and the particles stay stuck to each other.

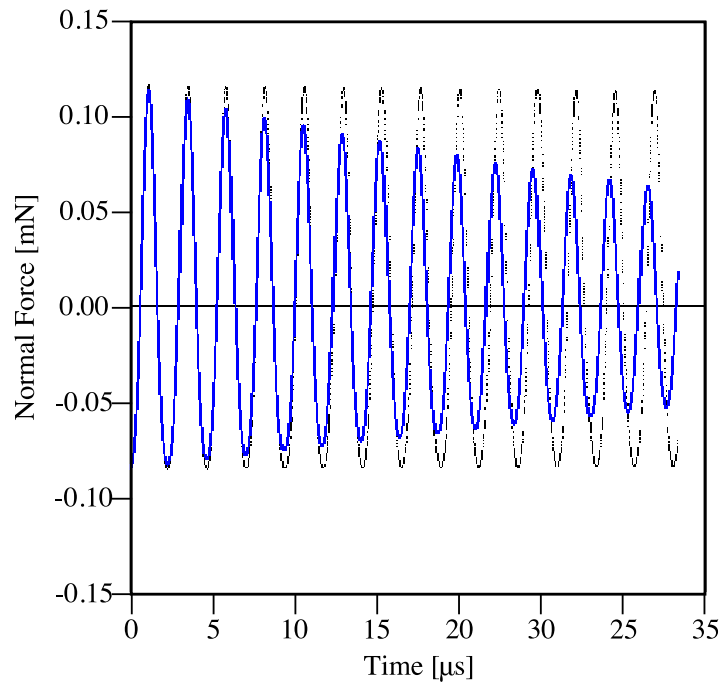
### 2.1.2 Thermal Particle Dynamics

The Thermal Particle Dynamics (TPD) simulation technique is based upon traditional PD but allows particles to exchange heat between each other and/or with walls. The key feature of TPD is that by incorporating contact conductance theories many simultaneous two-body interactions may be used to model heat transfer in a system composed of many particles. Consider particles  $i$  and  $j$  and their temperatures ‘far from the contact point’ to be  $T_i$  and  $T_j$ , respectively. The amount of heat transported per unit time is given by

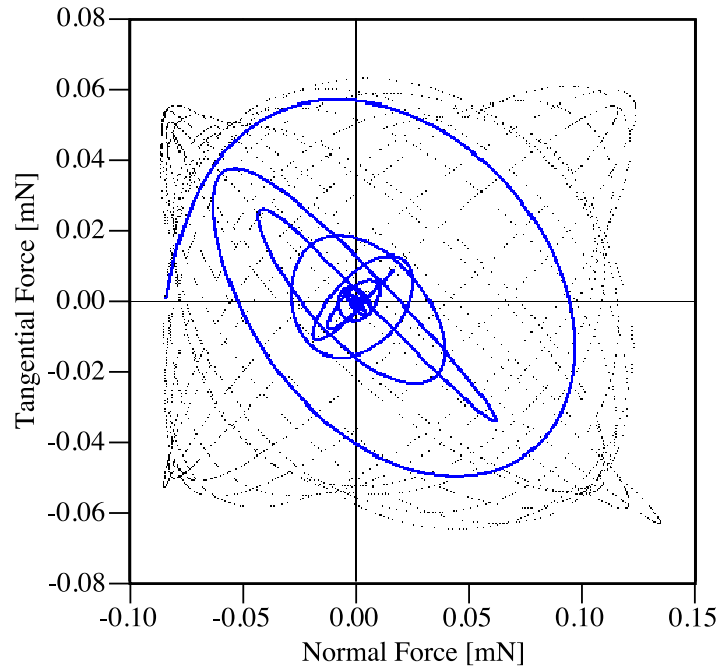
$$Q_{ij} = Hc(T_j - T_i) \quad (2.33)$$

where the contact conductance is calculated using  $Hc = 2k_S a$  (where  $k_S$  is the thermal conductivity of the pure solid material and  $a$  is the radius of the contact area between particles  $i$  and  $j$ ). When particle  $i$  is in contact with  $n$  particles, its rate of change of the temperature is given by

$$\frac{dT_i}{dt} = \frac{\sum_{j=1}^n Q_{ij}}{\rho_i c_i V_i}. \quad (2.34)$$



(a)



(b)

Figure 7: Contact damping for (a) a normal impact, (b) a tangential impact.

In analogy with PD, this description requires that the time-step be chosen such that any disturbance (in this case a change in a particle’s temperature) does not propagate further than that particle’s immediate neighbors within one time-step. Mathematically, this criterion can be shown to be met by choosing a time-step which satisfies

$$\frac{dT_i}{T_j - T_i} = \frac{Hc\Delta t}{\rho_i c_i V_i} = \frac{2k_{sa}\Delta t}{\rho_i c_i V_i} \ll 1. \quad (2.35)$$

While for this work we are considering particles that are largely in lasting contact, this criterion can also be satisfied in the majority of collision-dominated flows, although the amount of heat transferred between colliding particles under these conditions can be small [83]. More details of the simulation technique can be found in Ref. [84, 85]. Extensions of TPD to include the effect of stagnant interstitial fluids are straightforward and have also been explored [86]. Similar approaches have been developed for flowing gas-solid systems [87, 50, 88, 89, 90, 91].

### 2.1.3 Method of quaternions

Surfactants are commonly used to enhance the degree of solubility—or mixedness—of immiscible liquids. In Chapter 4, we propose to use amphiphilic particles as particulate analogues of surfactants in order to control the final mixed state of granular systems. As we will show, bi-face particles that exhibit different surface properties in each of their faces are able to allow systems to mix when the asymptotic state of the binary system leads to segregation and *vice versa*. The specific properties of each of the Janus particle’s faces can be chosen in order to favor one kind of interaction where they can act as a bridge between two-particles that would weakly interact otherwise.

To simulate non-symmetric particles it is necessary to know how each of these is rotating with time. Depending on the angular position, a Janus particle could be interacting with other beads with either of its faces. In Figure 8, the top and bottom particle collide with their ‘red’ and ‘yellow’ hemispheres, respectively. Since the collision is not normal (that is, the relative velocity has a component in the plane perpendicular to the normal vector), the tangential component of the contact force is non-zero and causes the particles to spin.

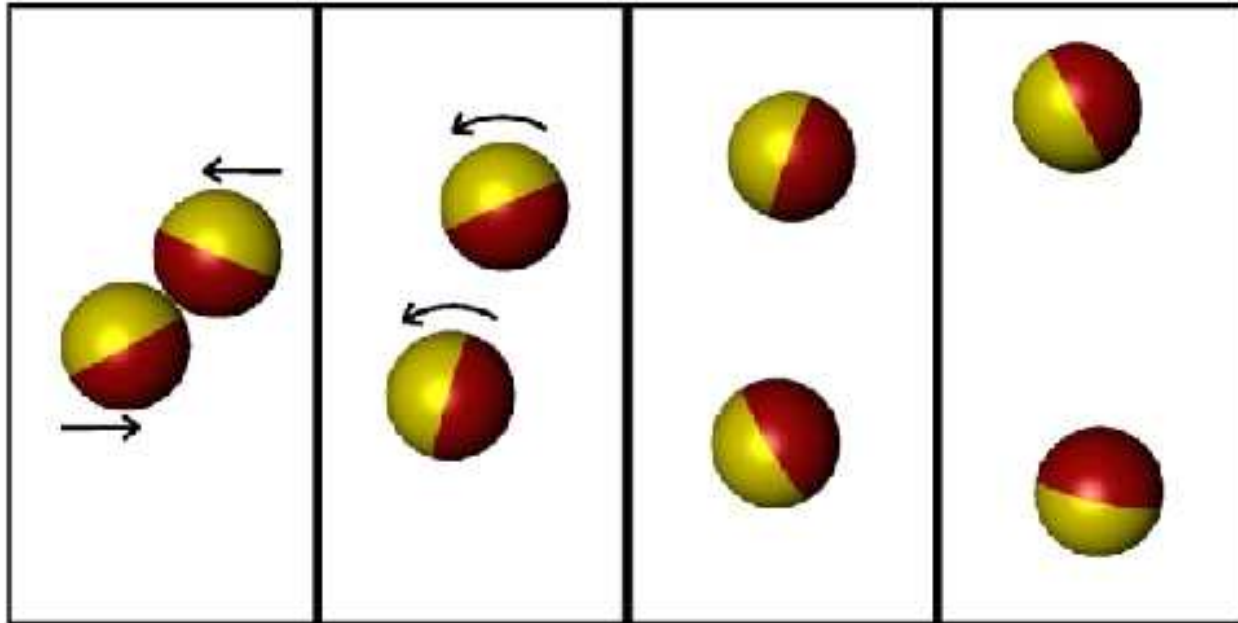


Figure 8: Non-symmetric particle rotation during a tangential collision.

Quaternions have been used to follow particle rotation: Dziugys [92] used quaternions to model the rotation of spherical and elliptical particles in DEM in processes such as rotary kilns and grueling grates; in the work of Langston [93], quaternions are used to model the discharge flow of frictionless particles from a hopper. Meister [94] used quaternions to simulate the rotation of non-symmetric objects in the space.

The rotation of a rigid object can be followed by determining the relation of a coordinate system fixed to the body with respect to a stationary coordinate system. Any vector  $e$  can be expressed with respect to the body-fixed coordinate system ( $e^b$ ) or the stationary coordinate system ( $e^s$ ). Both vectors are related by the rotation matrix  $A_r$  as follows,

$$e^b = A_r \cdot e^s \quad (2.36)$$

where  $A_r$  can be defined as

$$A_r = \begin{bmatrix} \cos(\phi_e)\cos(\psi_e) - \sin(\phi_e)\cos(\theta_e)\sin(\psi_e) & \sin(\phi_e)\cos(\psi_e) + \cos(\phi_e)\cos(\theta_e)\sin(\psi_e) & \sin(\theta_e)\sin(\psi_e) \\ -\cos(\phi_e)\cos(\psi_e) - \sin(\phi_e)\cos(\theta_e)\cos(\psi_e) & -\sin(\phi_e)\sin(\psi_e) + \cos(\phi_e)\cos(\theta_e)\cos(\psi_e) & \sin(\theta_e)\cos(\psi_e) \\ \sin(\phi_e)\sin(\theta_e) & -\cos(\phi_e)\sin(\theta_e) & \cos(\theta_e) \end{bmatrix} \quad (2.37)$$

where  $\phi_e$ ,  $\theta_e$  and  $\psi_e$  are the Euler angles. Evans [95] proposed a quaternion to describe the rotational motion, because a vector with three independent components can not provide equations with no singular points. The basic simulation algorithm is described in the work of Evans and Murad [96]. A quaternion  $Q$  is composed of four scalar quantities as

$$Q = (q_0, q_1, q_2, q_3). \quad (2.38)$$

Often the last three terms ( $q_1, q_2, q_3$ ), are considered vector components. The quaternions satisfy the constraint

$$q_0^2 + q_1^2 + q_2^2 + q_3^2 = 1, \quad (2.39)$$

and given the Euler angles  $(\theta_e, \psi_e, \phi_e)$  of a specific rotation, the quaternion components can be calculated from the following set of equations:

$$\begin{aligned}
q_0 &= \cos\left(\frac{1}{2}\theta_e\right) \cos\left[\frac{1}{2}(\phi_e + \psi_e)\right] \\
q_1 &= \sin\left(\frac{1}{2}\theta_e\right) \cos\left[\frac{1}{2}(\phi_e - \psi_e)\right] \\
q_2 &= \sin\left(\frac{1}{2}\theta_e\right) \sin\left[\frac{1}{2}(\phi_e - \psi_e)\right] \\
q_3 &= \cos\left(\frac{1}{2}\theta_e\right) \sin\left[\frac{1}{2}(\phi_e + \psi_e)\right].
\end{aligned} \tag{2.40}$$

Therefore the rotation matrix becomes

$$A_r = \begin{bmatrix} q_0^2 + q_1^2 - q_2^2 - q_3^2 & 2(q_1q_2 + q_0q_3) & 2(q_1q_3 - q_0q_2) \\ 2(q_1q_2 - q_0q_3) & q_0^2 - q_1^2 + q_2^2 - q_3^2 & 2(q_2q_3 + q_0q_1) \\ 2(q_1q_3 + q_0q_2) & 2(q_2q_3 - q_0q_1) & q_0^2 - q_1^2 - q_2^2 + q_3^2 \end{bmatrix}. \tag{2.41}$$

The quaternions further satisfy the equations of motion

$$\begin{bmatrix} \dot{q}_0 \\ \dot{q}_1 \\ \dot{q}_2 \\ \dot{q}_3 \end{bmatrix} = \frac{1}{2} \begin{bmatrix} q_0 & -q_1 & -q_2 & -q_3 \\ q_1 & q_0 & -q_3 & q_2 \\ q_2 & q_3 & q_0 & -q_1 \\ q_3 & -q_2 & q_1 & q_0 \end{bmatrix} \begin{bmatrix} 0 \\ \omega_{p_x}^b \\ \omega_{p_y}^b \\ \omega_{p_z}^b \end{bmatrix}. \tag{2.42}$$

yielding to a first order differential equation system that coupled to our PD model (that is capable of compute each particle's angular velocities  $\omega_p$ ) can be solved for each time-step to indicate the rotational position of each particle.

## 2.2 MIXING AND MIXING MEASURES

### 2.2.1 Mixing and segregation

Mixing is an operation where a relatively homogeneous substance is obtained from two or more ingredients, and the required quality of the mixture, or its homogeneity, depends on the powder mixture use. Industrially, poor mixing causes problems during handling, processing, transporting, or unit operations where granular materials are involved. Some examples are: fluctuation in food packages weight, discard of pharmaceutical powders because of variation of active/inactive ingredient composition, uneven composition of fertilizers, poor mechanical properties of compacts and abrasives, low conversion rates caused by poor reactant contact [2, 15]. However, in particle classification, segregation can facilitate the separation of grains. When a granular mixture of particles with the same physical properties—such as size, density, shape—is subjected to a mixing process, it asymptotically evolves to a perfect mixture as the process progress. However, particles composing powder mixtures commonly have different properties and, in this case, the material may exhibit segregation.

**2.2.1.1 Segregation mechanisms** Roughly, there are four segregating mechanisms that have been extensively studied: percolation/sieving, fluidization, convection, and trajectory segregation (Figure 9), although many more have been identified in the literature [97]. **Percolation** is commonly found in granular materials where there is a difference in particle size. When the particle mixture flows and particles can rearrange such as happens during stirring, vibration, pouring, tumbling, the smaller ones can fall down between the large particles and reach the bottom of the container. **Trajectory segregation** is based on the distance, or ‘stopping distance’, that a particle can horizontally travel before it lands when it is projected with a velocity  $v$  in a fluid of viscosity  $\mu_f$ , as happens at the end of a conveying belt. In the Stokes law region, this distance is given by  $S = \frac{v\rho d^2}{18\mu_f}$ , where  $\rho$  and  $d$  are the particle’s density and diameter, respectively. According to this equation, a particle twice as large can travel four times the distance. **Segregation by convection** [17] corresponds to the rise of large particles upon vibration. The convective upward movement of particles in the middle region

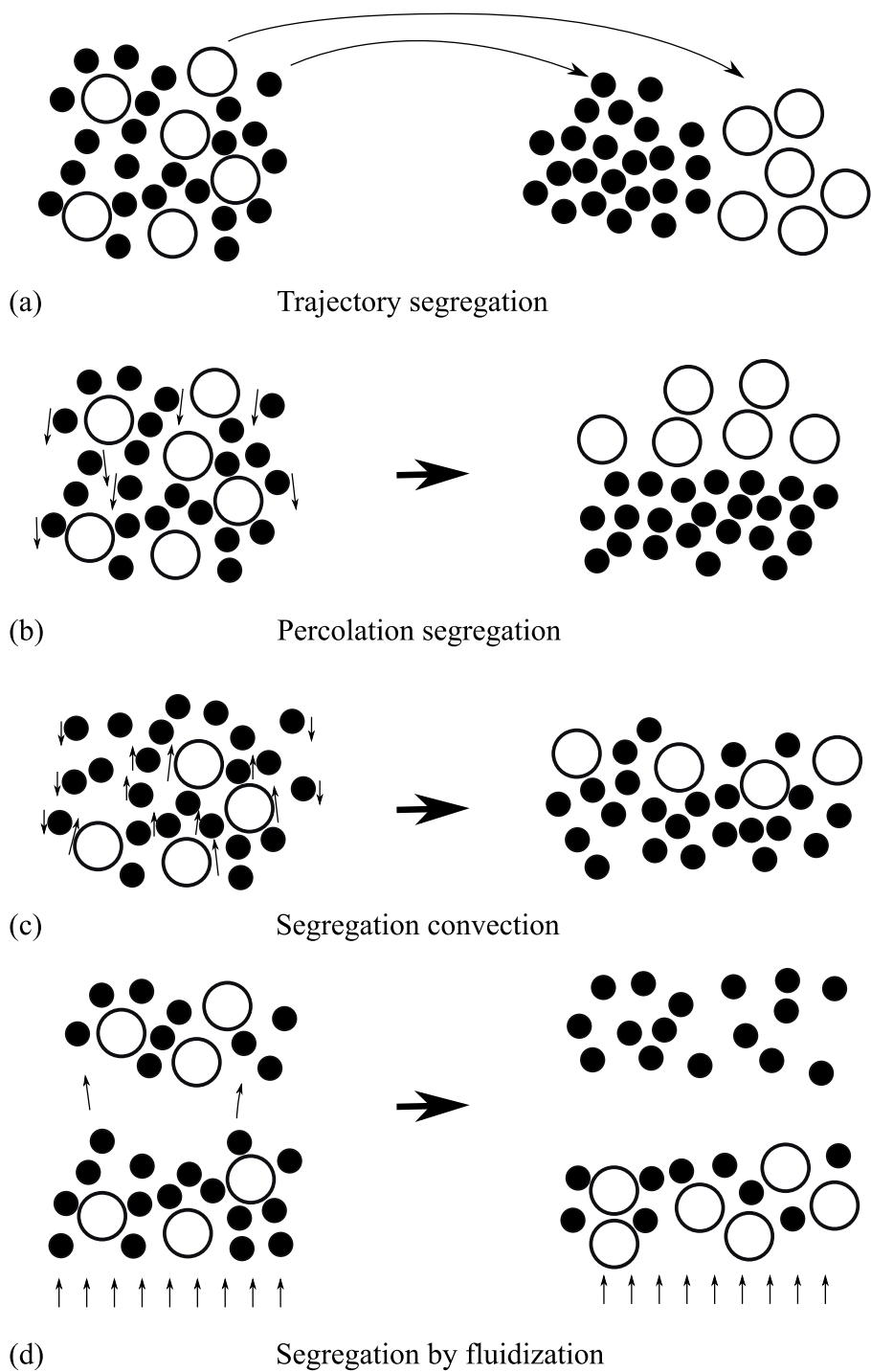


Figure 9: Segregation mechanisms.

of a vibrated bed causes all of the particles to rise, and segregation by size results when the large ones are prevented from returning to the bottom through the thin downward region close to the container walls. In a gas-fluidized bed, if the velocity is only moderately above the minimum fluidization velocity, the bed can **segregate by fluidization**: the ‘flotsam particles’ [98] (smaller and/or lighter particles) migrate to the upper part of the bed while the ‘jetsam’ particles (larger and/or heavier) tend to move towards the bottom of the bed.

**2.2.1.2 Practices to avoid segregation** Much of the research work in this area is aimed at proposing strategies to avoid or minimize segregation by either modifying the properties of the materials or controlling the operating conditions of the units that process and handle the material. Modifying the size distribution (by size reduction or agglomeration) may be the most effective way to minimize segregation [99, 100, 101], but it is often complicated and expensive [102]. For example, the mechanical properties of a compressed tablet can be affected by a change in the primary particle size. It is also possible to find a balance between size ratio and density difference to avoid segregation [103, 104]. However, reducing the particle size can also affect the flowability properties of the material [102]. Another method that can contribute to mitigate segregation is increasing the moisture content [105, 106].

Practically, the operation of industrial devices can be modified to avoid segregation by understanding the mechanism that cause it in each case. During a filling process (of a silo or of any storage container), granular material can segregate by trajectory, percolation and/or fluidization [102]. The first two are related to the formation of a heap, therefore some of the methods to avoid segregation in this kind of operation are oriented toward avoiding heap formation, or reducing its size and/or the size of the free-fall height by using different kind of distributors (that would form several smaller heaps) and inserts (chutes, egg-box inserts, etc) [102, 107, 108, 109, 110]. Segregation by fluidization appears due to the presence of fine particles or high free fall heights. The two natural methods to avoid this kind of segregation are increasing the particle size by granulation or reducing the free fall height [15, 111]. To discharge a silo, an efficient device is a mass flow discharge hopper [112]. In order to get a constant flow it is important to maintain a certain amount of material in the hopper. Inserts of different shapes can be added to avoid the formation of funnel flows [113].

A recent study by Shi *et al.* [114] showed that time modulation of the flow can be used to limit segregation. The key is to recognize that granular materials have a ‘preferred direction’ where particles tend to segregate and that segregation takes a finite amount of time ( $t_{SEG}$ ). The material cannot segregate as long as this ‘preferred direction’ is inverted/perturbed with a frequency higher than  $t_{SEG}^{-1}$ . Practically, this can be achieved by inverting the direction of the flow in a chute or selectively placing baffles in mixing devices.

**2.2.1.3 Segregation studies** Most of the practices previously mentioned are qualitative and/or have been developed empirically. However, in the last few years fundamental research on granular matter seems to have exploded [38] and studies from a fundamental point of view have arisen. Khakhar *et al.* [55] studied radial segregation (core formation) in a cascading flow. The results of their constitutive model (that requires one fitting parameter, the dimensionless segregation velocity) agree with their experimental observations in the segregation velocity and final degree of segregation. They also demonstrated competing cases of mixing and segregation and how, if mixing occurs fast enough, at a certain ‘optimal mixing time’ the intermediate state of the material can exhibit a higher mixing degree than the asymptotic state. The work of Makse and coworkers [8] show how a difference in the friction angle is enough to create a segregation pattern when the material is poured between two vertical plates. Particles stop rolling on the heap whenever the local slope is less than the maximum static angle of repose, then particles of different friction angles stop at different points in the heap. Another example of self organizing structures is the work by Hill *et al.* [7]. The patterns observed experimentally are explained by a continuum model that incorporates collisional diffusion and density-driven segregation. Khakhar [115] studied segregation driven by density as well as by size in a chute flow. Their theoretical predictions for equilibrium number density profiles agree with their computations for mixtures of equal sized particles with different density for all solids volume fractions, and for mixtures of different sized particles at low volume fractions.

The existence of forces other than ‘hard sphere’ repulsion and friction in a granular flow can dramatically affect the flow behavior. This was first introduced by Hersey [116] by using inter-particle forces to mitigate segregation by the concept of ‘ordered mixing’. This requires

particles that preferentially interact (by adsorption, surface tension, frictional, electrostatic, adhesion, etc.) with dissimilar ones to create a mixture that is more homogeneous than a random one. Practically, most inter-particle interactions are cohesive and can be classified in two main types: wet (induced by liquid bridges) and dry (caused by inter-particle forces). Kudrolli [117] *et al.* studied the effect of the moisture content in the degree of segregation of a bi-disperse mixture of powders that is poured from a hopper. For small volume fraction of fluid, they found that segregation was mitigated by viscous and capillary forces and, when the moisture content was increased, they reported a transition back to a segregated state. Geromichalos [118] identified three different regimes—viscoelastic, gaseous and intermediate—of the dynamic behavior of wet granular materials, depending on the effect (enhance mixing/segregation) of incrementing the moisture content in the degree of mixing of a jar containing glass particles of two different radius. Hsiao [119] also observed that the degree of mixing can be increased by adding moisture in a vibrating bed. A more general approach was adopted by Li *et al.* where the mixing degree of binary mixtures of particles of different sizes, densities and hydrophobicities is predicted from the physical properties of the powders. The model is based on dimensionless numbers, (Granular Bond Number  $Bo_{ij}$ ) and their predictions have been compared with experiments.

The case of mixing and segregation of dry adhesive forces remains unexplored. An exception is the work by Hutton and coworkers [120], they use a magnetic field to control the inter-particle forces in a mixture of iron and a non-magnetic particles. They describe phase diagrams as a function of the relative magnitude inter-particle force to the particle weight and the effective particle size of the clusters formed, to determine regions of ‘increased ability to mix’.

### 2.2.2 Mixing measures

The use of the powder mixture determines the quality of mixture standards. Danckwerts [121] used the term ‘scale of scrutiny’ as the maximum size of the segregating regions that can cause the mixture to be considered acceptable for its intended use. For a given powder, its quality of mixture decreases as the scale of scrutiny, with the extreme case where each

sample contains only one particle. In this section, some measures that attempt to quantify the degree of mixture are described, among them Intensity of Segregation ( $IS$ ), which is the mixing measure used in this work.

**2.2.2.1 Intensity of Segregation** The Intensity of Segregation ( $IS$ ) is essentially the standard deviation of the concentration calculated at multiple spots in the granular bed, and is calculated using:

$$IS = \sigma = \sqrt{\frac{\sum_{i=1}^N (C - \langle C \rangle)^2}{N - 1}} \quad (2.43)$$

where  $N$  is the number of concentration measurements,  $C$  is the concentration of the tracer particles in the designated measurement location, and  $\langle C \rangle$  is the average concentration of that type of particle in the entire bed. It should be noted that large values (approaching 0.5 for a equi-volume mixture) of  $IS$  correspond to a segregated state while smaller values denote more mixing.

**2.2.2.2 Lacey mixing index** The Lacey mixing index is defined as a function of the variance ( $\sigma^2$ ) of the composition of the actual mixture, the variance  $\sigma^2$  of the composition of the corresponding completely segregated mixture ( $\sigma_{SEG}^2$ , that is, its upper limit) and the variance of the perfectly mixed granular material ( $\sigma_{MIX}^2$ , lower limit) as:

$$\text{Lacey mixing index} = \frac{\sigma_{SEG}^2 - \sigma^2}{\sigma_{SEG}^2 - \sigma_{MIX}^2} \quad (2.44)$$

In other words, this index represents the ratio of the degree of mixing achieved to the maximum mixing possible. A Lacey mixing index equal to 1 corresponds to a perfectly mixed state, and value of 0 corresponds to complete segregation.

**2.2.2.3 Poole mixing index** The mixing index defined by Poole is defined as:

$$\text{Poole mixing index} = \frac{\sigma^2}{\sigma_{MIX}^2} \quad (2.45)$$

A value of 1 for the Poole mixing index represents a perfect mixture, and this index increases as the mixing quality decreases.

### 2.2.3 Poincare sections

The mixing measures described in the previous section aim to describe the mixing degree of a powder mixture but make no attempt to examine how that mixture is achieved. As we will examine the role of advective mixing in determining the rate of granular heat transfer in Chapter 6, it is useful to review methods of studying this mixing mode. In a tumbler mixer, the particles move relative to each other in the bed even in the simplest case—when the grains are identical—because of particle advection. Advection in tumblers can be studied in at least two different ways with the most common methods being [122]: (i) calculation of the Poincaré sections (stroboscopic maps of the particle trajectories), or (ii) studying blob deformation. The former method will be used in this work.

In order to isolate the advective effects of a granular we use the model developed by Khakhar [123] that applies to mixing of non-cohesive identical grains. The utility of this model to gain understanding about heat transfer mechanisms in granular systems is further described in Chapter 6; but, in short, by comparing the heat redistribution in simulated

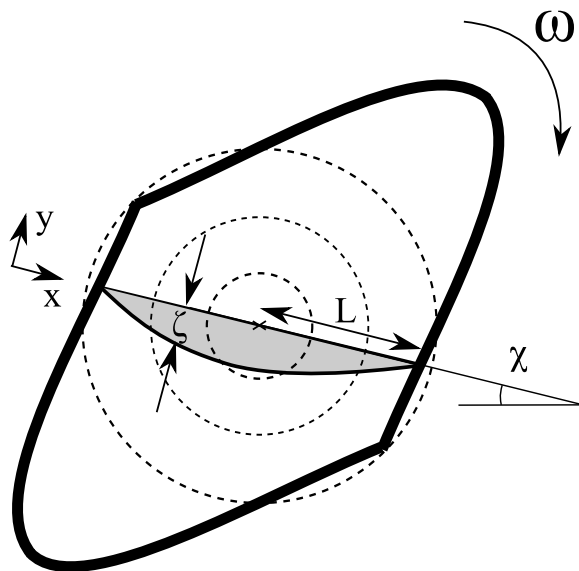


Figure 10: Schematic picture of half-filled rotating tumbler showing the shear layer (grey), its thickness ( $\zeta$ ) and length ( $L$ ). The free surface forms a  $\chi$  angle with the horizontal.

rotating tumblers with the advective flow that governs mixing in the two-dimensional non-heated model described in Ref.[123], we will determine the predominance of advection in the overall transfer of heat.

The model describes the single phase, incompressible, continuum flow of these grains in a two-dimensional tumbler of arbitrary shape when it rotates at constant angular velocity ( $\Omega$ ) in the continuous rolling regime. In this regime, particles below the free surface move in solid body rotation with radial velocity  $\Omega\sqrt{x^2 + y^2}$ , while near the free surface particles move relative to each other in a lens shaped shear region designated as the shear or flowing layer. The following description is restricted for cases of half filled, convex rotating tumblers which are symmetric with respect to 180° rotations about their centroid. In the shear layer, particle velocities are given by

$$\bar{v}_x = \frac{\bar{L}}{\kappa} \left( 1 + \frac{\bar{y}}{\bar{\zeta}} \right) \quad (2.46)$$

$$\bar{v}_y = -\bar{x} \left( \frac{\bar{y}}{\bar{\zeta}} \right)^2 \quad (2.47)$$

where the shear layer thickness is  $\bar{\zeta} = \bar{\zeta}_0[1 - (\bar{x}/\bar{L})^2]$ .

For circular tumblers the mean velocity field is time independent. However, if the angular velocity is a function of time and/or the tumbler is not rotationally invariant, the flow becomes time dependent and the parameters of the shear layer need to be function of time. In particular, the maximum length  $L$ , shear layer thickness  $\zeta$ , and mean velocity  $u$  of the flowing layer will vary as the tumbler rotates.

The variation of the dimensionless shear layer length with time for an elliptical shape is given by

$$\bar{L}(t) = \frac{\bar{B}}{\sqrt{B^2 \cos^2 \vartheta + \sin^2 \vartheta}} \quad (2.48)$$

with  $\vartheta = (\bar{t} + v) \bmod 2\pi$  (where  $v$  is the initial angle between the free surface and the major axis of the ellipse), and  $\bar{B} = B_E/A_E$ , where  $A_E$  and  $B_E$  are the major and minor semi-axes

of the ellipse, respectively. For a rectangular shape the free surface length can be calculated from

$$\bar{L}(t) = \begin{cases} \frac{1}{|\cos \vartheta|}, & \text{if } \vartheta < \vartheta_d \text{ or } |\pi - \vartheta| < \vartheta_d \text{ or } \vartheta > (2\pi - \vartheta_d) \\ \frac{\bar{B}}{|\sin \vartheta|}, & \text{otherwise} \end{cases} \quad (2.49)$$

with  $\vartheta_b = \tan^{-1} \bar{B}$ . Again, the rescaled parameters of the flow are the aspect ratio  $\bar{B} = B_E/A_E$ , where  $A_E$  and  $B_E$  are the major and minor semi-axes of the geometry, and the maximum mid-layer thickness  $\bar{\zeta}_{o,max} = \kappa$ . The value of the parameter  $\kappa$  can be obtained from experimental observations [123], and is typically 5–15 particle diameters. Also, this experimental work had shown that the maximum mid-layer thickness is linearly dependent on the shear layer length  $L$ , (i.e.  $\bar{\zeta}_o/\bar{L} = \kappa$ ). In this work we use  $\bar{L}_{max} = 1$ , and  $\bar{\zeta}_{o,max} = \kappa = 0.15$ . The Poincaré sections are then obtained by integration in time of the equations describing the velocity field, both in the shear layer and the solid body rotation region. The trajectories are computed from

$$\frac{d\bar{x}}{d\bar{t}} = \bar{v}_x(\bar{x}, \bar{y}, \bar{t}), \quad (2.50)$$

$$\frac{d\bar{y}}{d\bar{t}} = \bar{v}_y(\bar{x}, \bar{y}, \bar{t}) \quad (2.51)$$

where  $\bar{v}_x, \bar{v}_y$  is the velocity field described by Eqs. 2.46–2.47. Equations 2.46 and 2.47 represent the Lagrangian description of the convective diffusion equation, neglecting the diffusion component.

### 3.0 PREDICTING MIXING AND SEGREGATION OF ADHESIVE GRANULAR MATERIALS

When the size of particles is very small, the impact of van der Waals forces on their behavior becomes significant. A better understanding of the impact of this force on processing of fine particles would be useful to many industries (e.g., pharmaceutical, nuclear reactors, ceramics, coatings). Tools for the characterization, scaling, and prediction of the behavior of adhesive granular systems can critically change the analysis and design of industrial operations involving fine powders. Despite significant advances in the understanding of the impact of other forms of cohesion on the mixing and segregation of granular materials [124, 118, 117, 125] the role of adhesion due to van der Waals forces in the mixing/segregation process has not been extensively studied. In contrast, the impact of this kind of cohesion on the behavior of colliding particles/surfaces has long attracted attention from researchers [126, 75, 127, 79, 80]. It is these theories that will form the basis of the simulations presented here. The objective of this work is to examine the behavior of cohesive elastic-plastic particles and provide characterization tools capable of predicting the asymptotic state of these systems—i.e., whether than state is more mixed or more segregated than the comparable non-cohesive counterpart.

#### 3.1 THEORY

##### 3.1.1 Granular Bond number

We define the van der Waals Granular Bond number,  $Bo_{vdw}$ , as an extension of the Granular Bond Number ( $Bo_g$ ) [106, 124], to quantify the impact of adhesive binary interactions on

mixing. We assume that adhesiveness is caused by van der Waals interactions. The  $Bo_{vdw}$  is calculated as the ratio of the van der Waals force ( $F_{vdw}$ ) to other relevant forces in the system. The latter correspond the gravitational force, and our  $Bo_{vdw}$  is a function of the particle weight ( $W$ ) such that

$$Bo_{vdw_{ij}} = \frac{F_{vdw}}{W} = \frac{2\pi\Gamma_{ij}R^*}{\frac{4}{3}\pi g [R^3\rho]_m}, \quad (3.1)$$

where  $\Gamma$  is the surface energy of particles, and  $(R^3\rho)_m$  is the smaller of the two particle masses to represent the fact that the less massive particle's motion will be dominated by the more massive particle (i.e., it will behave as a guest). While the choice of the value for  $F_{vdw}$  in this expression could be made to follow either the JKR or DMT approach, we instead choose to use a pre-factor of 2 in analogy to the case of cohesive (wet) granular material studied in Ref. [124]. Note that, in the next section, our analysis will focus on ratios of  $Bo_{vdw}$  so that the exact value of this pre-factor is insignificant.

In order to build our simple mixing theory, the values of the  $Bo_{vdw}$  for each potential pair of particles,  $i$  and  $j$ , within the system need to be compared (i.e., for a binary system, we need to calculate  $Bo_{vdw_{11}}$ ,  $Bo_{vdw_{22}}$ , and  $Bo_{vdw_{12}}$ , where 2 is defined as the larger of the particles, see Fig. 11). Alternatively, in cases where the dominant non-adhesive force has a non-gravitational origin (e.g., in cases where the shearing forces are larger than gravitational forces) a similar approach can be used with a different choice of force scaling (see Ref. [128] for work focused on the shearing of wet granular mixtures).

### 3.1.2 Phase diagrams

The most convenient use of  $Bo_{vdw}$  as a predictive tool is to develop phase-space diagrams so that we may visually identify regions where systems tend to mix/segregate. We find the boundaries of each of these regions by comparing the magnitudes of the various  $Bo_{vdw_{ij}}$  of the system. This comparison can be written in dimensionless form as:

$$\mathfrak{R}_1 = \frac{Bo_{vdw_{11}}}{Bo_{vdw_{12}}} = \frac{\Gamma_{11}}{\Gamma_{12}} \frac{R_1 + R_2}{2R_2} \frac{(R_1^3\rho_1, R_2^3\rho_2)_{min}}{R_1^3\rho_1} \quad (3.2)$$

$$\mathfrak{R}_2 = \frac{Bo_{vdw_{22}}}{Bo_{vdw_{12}}} = \frac{\Gamma_{22}}{\Gamma_{12}} \frac{R_1 + R_2}{2R_1} \frac{(R_1^3\rho_1, R_2^3\rho_2)_{min}}{R_2^3\rho_2}, \quad (3.3)$$

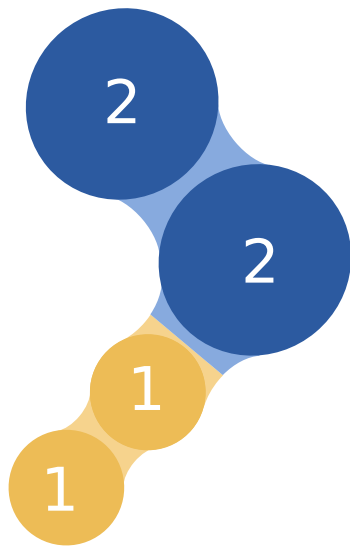


Figure 11: Three possible interactions in a binary system characterized by  $Bo_{vdw_{11}}$ ,  $Bo_{vdw_{22}}$ , and  $Bo_{vdw_{12}}$ .

where  $\alpha = \rho_1/\rho_2$ ,  $\beta = R_1/R_2$ , and  $\phi = \sqrt{\Gamma_{11}/\Gamma_{22}}$  can be used together with the combining rule,  $\Gamma_{12}^2 = \Gamma_{11}\Gamma_{22}$  [78], to these expressions to

$$\mathfrak{R}_1 = \frac{Bo_{vdw11}}{Bo_{vdw12}} = \phi \frac{\beta + 1}{2} \frac{(\alpha\beta^3, 1)_{min}}{\alpha\beta^3} \quad (3.4)$$

$$\mathfrak{R}_2 = \frac{Bo_{vdw22}}{Bo_{vdw12}} = \frac{1}{\phi} \frac{\beta + 1}{2\beta} (\alpha\beta^3, 1)_{min}. \quad (3.5)$$

In order to determine the mixing behavior, we can then locate the boundaries of our mixing/segregation phases in the diagram by analytically identifying where in the parameter space of size ratio ( $\beta$ ), density ratio ( $\alpha$ ) and surface energy ratio ( $\phi$ ) differing hierarchies of  $Bo_{vdw_{ij}}$  are observed. Regions in the phase diagrams where the predominant interaction is the interaction between dissimilar particles (i.e., particles 1-2) lead to a mixed asymptotic state. When this is not the case, we expect an asymptotic state to exhibit segregation. In other words, systems where both  $\mathfrak{R}_1$  and  $\mathfrak{R}_2$  are less than one will achieve a mixed asymptotic state and systems where either  $\mathfrak{R}_1$  or  $\mathfrak{R}_2$  are greater than one will result in a segregated state (Figure 12).

After some manipulation, the following cases may be observed:

If  $\alpha\beta^3 > 1$

$$1 < \mathfrak{R}_1, 1 < \mathfrak{R}_2 \quad \frac{2\alpha\beta^3}{1+\beta} < \phi < \frac{1+\beta}{2\beta} \quad (3.6)$$

$$\mathfrak{R}_1 < 1 < \mathfrak{R}_2 \quad \phi < \frac{2\alpha\beta^3}{1+\beta} \quad (3.7)$$

$$\mathfrak{R}_2 < 1 < \mathfrak{R}_1 \quad \phi > \frac{1+\beta}{2\beta} \quad (3.8)$$

If  $\alpha\beta^3 < 1$

$$\mathfrak{R}_1 < 1, \mathfrak{R}_2 < 1 \quad \frac{(\beta^3+\beta^2)\alpha}{2} < \phi < \frac{2}{1+\beta} \quad (3.9)$$

$$\mathfrak{R}_1 < 1 < \mathfrak{R}_2 \quad \phi < \frac{(\beta^3+\beta^2)\alpha}{2} \quad (3.10)$$

$$\mathfrak{R}_2 < 1 < \mathfrak{R}_1 \quad \phi > \frac{2}{1+\beta} \quad (3.11)$$

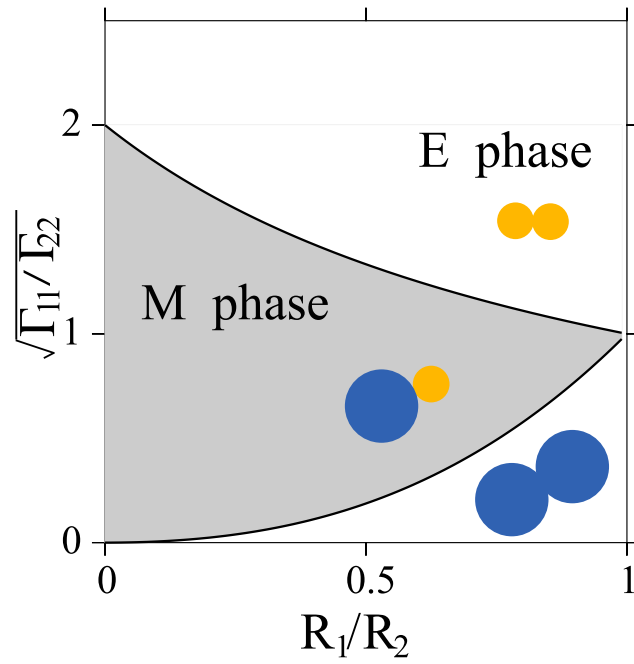


Figure 12: Schematic phase diagram showing regions where interactions 1-1, 2-2 and 1-2 predominate.

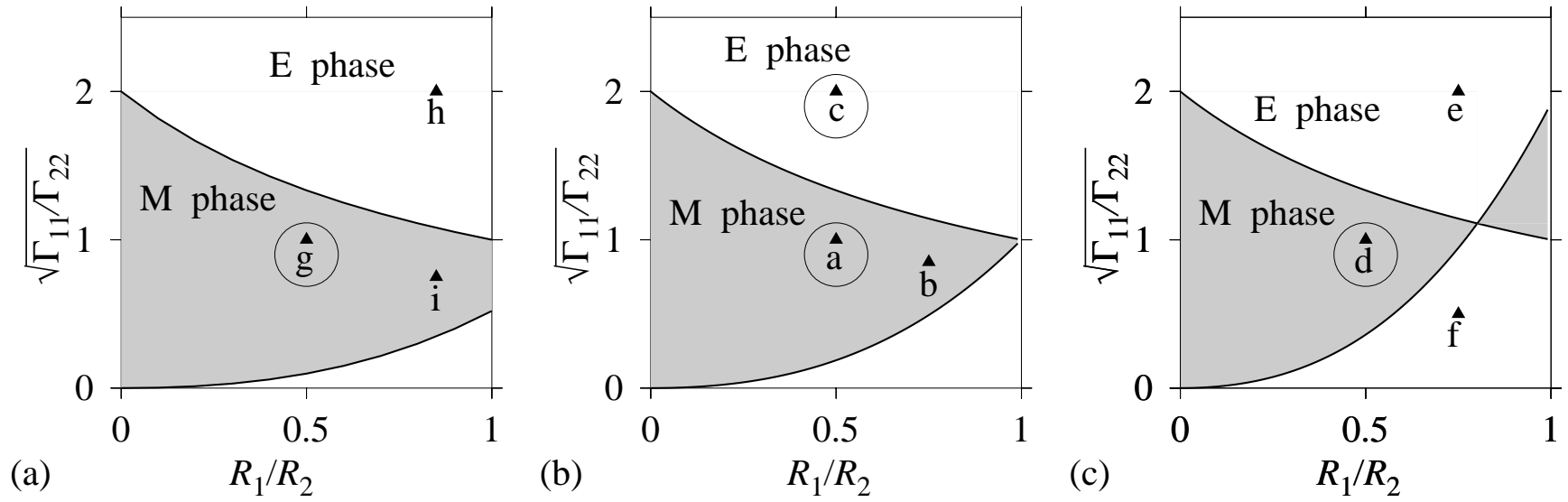


Figure 13: Phase diagrams exhibiting E (Enhanced segregation) and M (Mitigated Segregation) phases for density ratio (a)  $\alpha = 0.52$ , (b)  $\alpha = 1.00$ , and (c)  $\alpha = 1.92$

Regions of the phase space where adhesive interactions enhance (E phase) or mitigate (M phase) segregation are denoted in Figure 13 as light and dark regions, respectively. Note that the accuracy of the phase diagram predictions is subjected to the validity of the assumptions of our theory. These can be summarized as follows. First, only two-particle interactions exist in our systems; that is, interactions of clustered particles with other single/clustered particles are taken into account. This assumption may not be valid if the size difference between particles is significant. Second, systems are “thermalized” and the frequency of occurrence of each kind of interaction (1-1, 1-2, 2-2) is similar. This means that the flow in the system is such that each particle can explore all possible interactions to choose its more favorable asymptotic partners and, that each of these partners can be visited with comparable frequency. This is most likely to be true for case where the all particles in the system have similar sizes ( $\beta$  close to 1). Last, the planes where ratios  $\mathfrak{R}_1 = 1$  and  $\mathfrak{R}_2 = 1$  are assumed to determine the boundary between the mixing and segregating spaces. In other words, our simple theory predicts a discontinuity at these boundaries while . As will be seen in Section 3.2, both of these assumptions can have negative impact on our results. Nevertheless, this approach is surprisingly effective in many instances.

### 3.2 TUMBLER SIMULATIONS

In this section, PD simulations of binary mixtures of particles in rotating tumblers are used as a testbed for the results shown in Figure 13. Because the proposed theoretical arguments suggest *changes* in the asymptotic mixing behavior exhibited by cohesive versus free-flowing systems, we first examine the results of free-flowing mixing exercises. These results are then compared to those obtained for van der Waals adhesive materials. Before beginning a detailed comparison of theory and simulation, we should note several key assumptions of our approach that are not necessarily consistent with the behavior of real systems. First, we consider only interactions between two primary particles. Clearly if the cohesive interactions are strong enough, or size discrepancies are sufficiently large, multi-particle interactions will become significant. Second, we assume that the system is “thermalized” enough that each

particle will have the opportunity to choose its most favorable asymptotic partner. In the case of each of these assumptions, the absolute magnitude of the cohesive interaction will play a role in determining how (in)valid the approximation/prediction is; therefore, in the following sections we vary this absolute magnitude in order to elucidate its role.

The initial conditions correspond to static tumblers with particles segregated by color in each (left and right) half of the tumbler. These particle arrangements are obtained via a preliminary simulation whereby particles are aligned on a perturbed hexagonal lattice and allowed to settle under the influence of gravity. The tumbler is 28 particles in diameter and 4 particles long (and periodic) in the axial direction. The rotation rate corresponds to 5 [rpm], and the simulation is run up to 5–12 revolutions, depending on the time required to reach its asymptotic state. As we are interested only in kinematics the particle stiffness used is reduced in order to decrease necessary simulation time (a practice shown to have essentially no impact on flow kinematics [129]) and the particle diameter is scaled up to 4 [mm] (with corresponding increases in the surface energy to obtain the proper  $Bo_{vdw}$  range). The simulation parameters of the base case are as shown in Table 4. The particles of the tumbler walls are assumed to have the same material properties of the larger particles in the system. In order to quantify the degree of mixing, we examine the evolution of the  $IS$  for each system and the prediction given by the phase diagram is compared with the PD simulation result.

We should note that each point of the phase space to be examined corresponds to a system that has a fixed value of size ratio ( $\beta$ ), density ratio ( $\alpha$ ) and surface energy ratio ( $\phi$ ). Therefore, there is some flexibility available for us in choosing the absolute sizes, densities, and surface energies while still examining the relevant points in phase space. As mentioned previously, it is important that we carefully choose the degree of adhesion such that cohesive interactions are not overwhelmed by collisional forces, yet cohesion is small enough that large particle clusters are not persistent. As such, we will examine two distinct ranges of  $Bo_{vdw}$  in the following sections.

Table 1: Van der Waals Granular Bond numbers for cases  $b$ ,  $e$ ,  $f$ ,  $h$  and  $i$

Simulation	freeflow	adhesive case			$IS$	$\mathfrak{R}_1$	$\mathfrak{R}_2$
	$IS$	$Bo_{11}$	$Bo_{22}$	$Bo_{12}$			
b	<b>0.34</b>	11.3	8.77	15.2	<b>0.25</b>	0.74	0.58
e	<b>0.37</b>	26.6	7.18	15.2	<b>0.39</b>	1.75	0.47
f	<b>0.37</b>	6.65	28.7	15.2	<b>0.40</b>	0.44	1.89
h	<b>0.19</b>	28.04	2.65	15.1	<b>0.39</b>	1.85	0.17
i	<b>0.19</b>	10.6	7.13	15.3	<b>0.19</b>	0.69	0.47

### 3.2.1 PD simulations vs. phase diagram prediction: systems $\beta > 0.5$

We start our mixing/segregation studies by simulating cases where the size differences are not particularly large, i.e.,  $\beta > 0.5$ . In these simulations, our results are found to be somewhat insensitive to cohesion degree so, in this section, we (somewhat arbitrarily) choose our cohesive scale such that  $Bo_{vdw_{12}} \sim 15$  and consider this as the base case for adhesion in latter studies. Table 1 summarizes the Granular Bond Number for the systems treated in this section and includes the asymptotic value of  $IS$  reached in each case (i.e., it is an average of the final three points in Figures 14, 15 and 16). Case  $b$  corresponds to particles with size differences ( $\beta = 0.75$ ), but no density difference. Because of this, the corresponding free-flowing case segregates as indicated by an Intensity of Segregation value ( $IS_{ff_b}$ ) of 0.34 after 14 revolutions. The phase diagram predicts that adhesive forces will mitigate segregation as the small-large interaction is the strongest. The evolution of the  $IS$  both for the free-flowing and the adhesive case is presented in Figure 16 and depicts how the non-adhesive system achieves a segregated asymptotic state, while mixing is enhanced by the presence of adhesion (resulting in an  $IS_b$  value of 0.25, which is seemingly still decreasing). Next, we examine cases  $e$  and  $f$  which correspond to systems where both size and density differ. Specifically, the smaller particle is also more dense so that dramatic segregation is expected in the free-

flowing case. For case  $e$ , cohesive interactions between the like smaller particles is dominant, while in system  $f$  the strength of the large-large interaction is biggest. In other words, strong segregation is expected in all cases, whether cohesive or free-flowing. As can be seen in Figure 14, after 5 revolutions, all systems are clearly segregated as expected and indicated by the  $IS$  values ( $IS_e = 0.39$ ,  $IS_f = 0.40$ ). Finally, in systems  $h$  and  $i$ , the smaller particles are less dense so that segregation by size and density have competing effects. The size effect promotes the migration of the small (light) particles toward the inner core, whereas the density effect pushes the light (small) particles toward the periphery. These opposing effects cancel in the free-flowing case, and the system with no adhesion is mixed after 7 revolutions (see Figure 15b). For the adhesive cases  $h$  and  $i$ , our model predicts that their asymptotic states will depend on the surface energy ratio of the particles. For the case  $h$ , where  $\phi = 2.0$  the system will segregate, while in case  $i$  (where  $\Gamma_{11} = \Gamma_{22}$ ) the system is expected to mix. These results may be rationalized as follows. When the smaller particles have a significantly higher surface energy compared to the other particles present in the system (as in system  $h$ ), they tend to form clusters exclusively composed of small particles. As a consequence, these clusters of particles are large enough to overcome the tendency of individual small particles to migrate toward the center and the density-based segregation dominates (Figure 15). However, in the case where the surface energies are equal, cluster formation of dissimilar particles is favored, therefore the mixing tendency of the free-flowing case is not affected by adhesion. The mixing progress as well as the  $IS$  values (after 6 revolutions,  $IS_{ffhi} = 0.19$ ,  $IS_h = 0.39$  and  $IS_i = 0.19$ ) confirm the predictions given by our phase diagrams.

### 3.2.2 Effects of adhesion in tumbler simulations: systems $\beta = 0.5$

As a further test of our predictions, we next examine systems with larger size differences ( $\beta = 0.5$ , highlighted with circles in Figure 13). As expected, however, this tends to emphasize the fact that we have neglected interactions beyond binary and, as we will see, the absolute degree of cohesion becomes more significant in these systems. The cases examined here involve: size segregation only ( $a$  and  $c$ ), which segregates strongly when free-flowing; size and density segregation that augment each other ( $d$ ), which yields dramatic segregation in

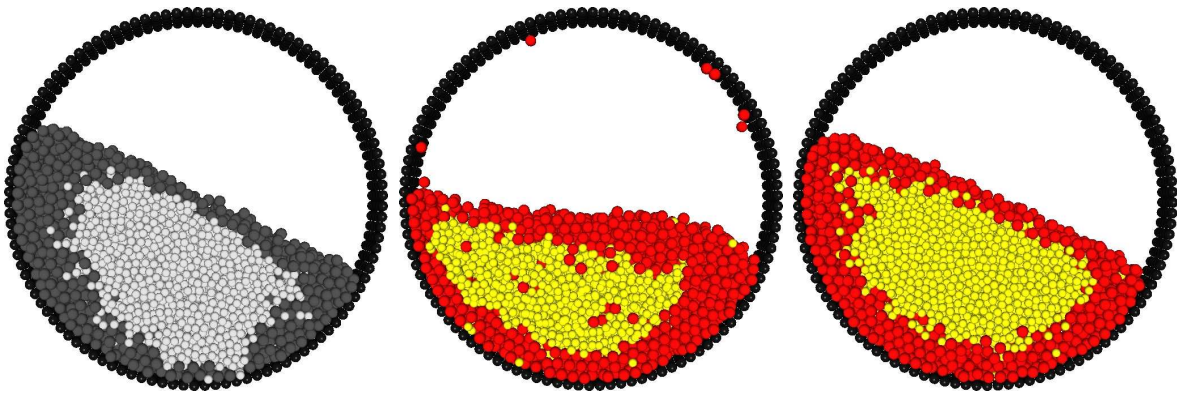
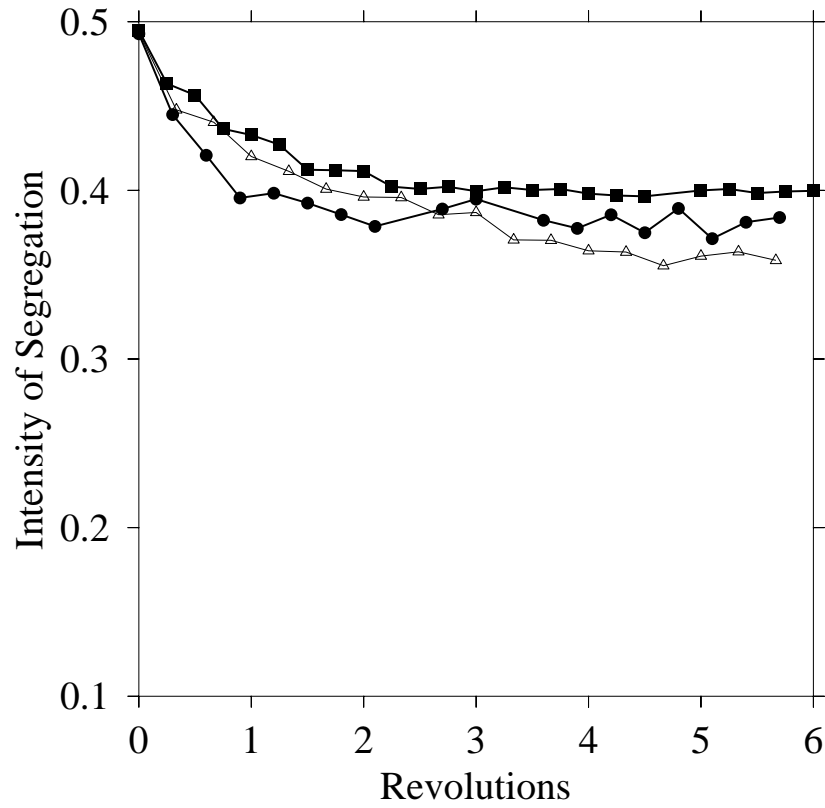


Figure 14: Mixing progress for tumbler cases  $e$  and  $f$  (● and ■, respectively) and the corresponding free-flowing case (△). The tumbler snapshots at the bottom corresponds to the mixing state after 5 revolutions.

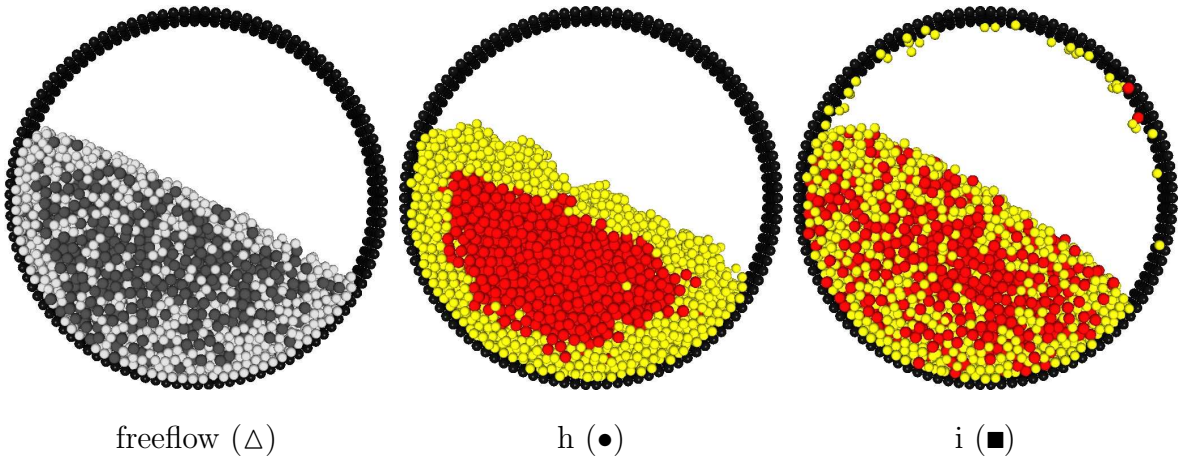
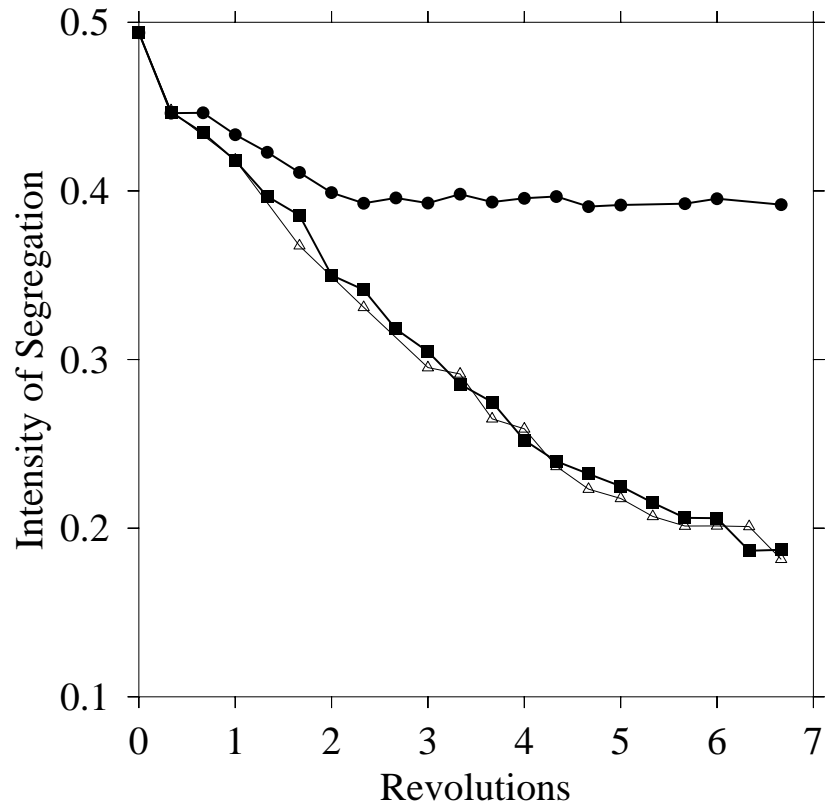


Figure 15: Intensity of Segregation for cases  $h$  and  $i$  ( $\bullet$  and  $\blacksquare$ , respectively) and the corresponding free-flowing case ( $\Delta$ ).

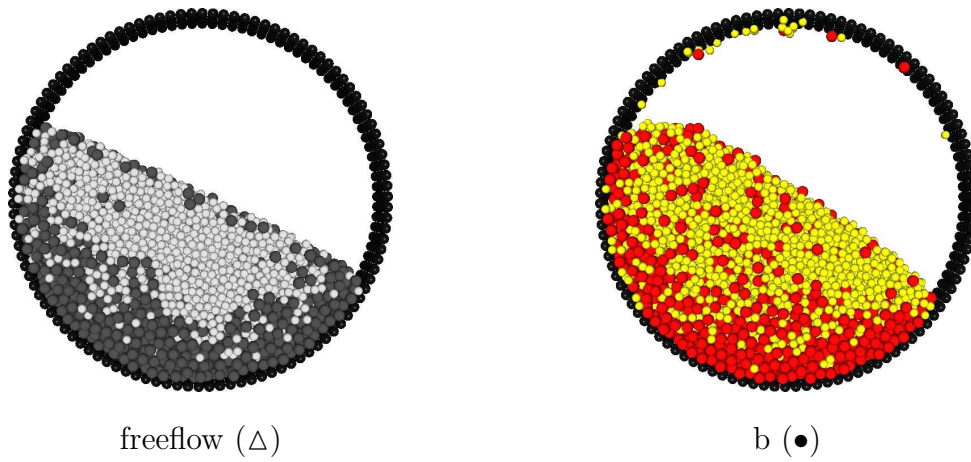
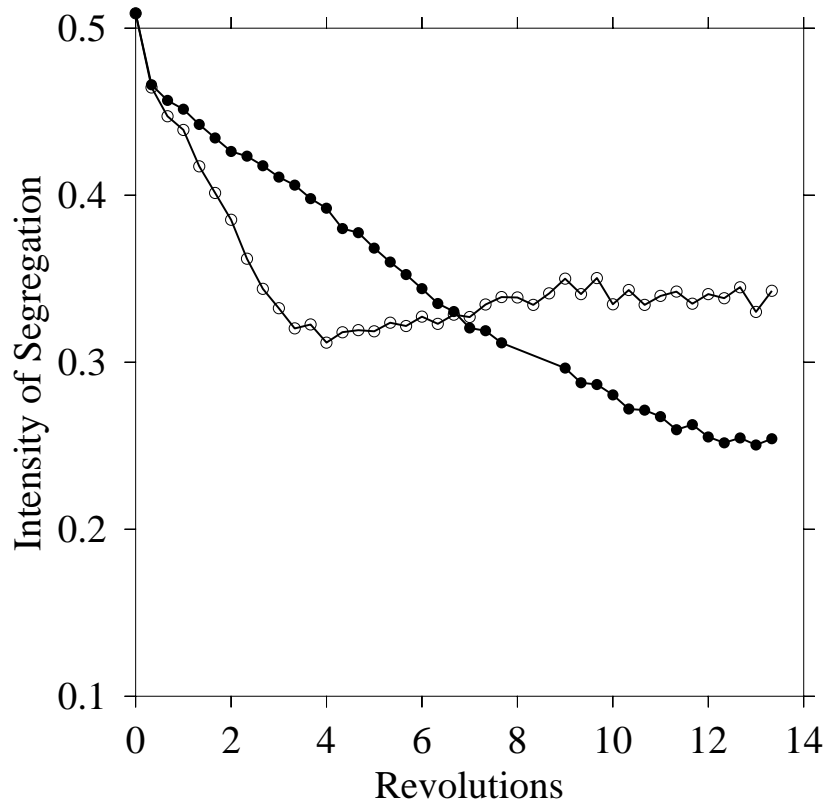


Figure 16: Intensity of Segregation for case *b* ( $\bullet$ ) and its corresponding free-flowing counterpart ( $\circ$ ).

the free-flowing case; and size and density segregation that compete ( $g$ ), so that the free-flowing case is somewhat mixed. First, we examine these systems using the base adhesion degree described in section 3.2.1. Then, we revisit these systems by running PD simulations corresponding to the same points in the phase diagrams, now with higher surface energies (more adhesion). The new systems have been scaled to yield  $Bo_{vdw_{ij}} \sim 30$  (more adhesive case). A listing of all of the Granular Bond Numbers are in Table 2.

In the case of system  $a$ , the strongest cohesive interaction is for dissimilar particles (i.e., the “mixing” interaction), so we expect that adhesion will increase the extent of mixing. In Figure 17a, it can be observed that the degree of mixing of system  $a$  is higher than the respective free-flowing case ( $IS_{ffac} = 0.38$ ,  $IS_a = 0.33$ , for 6 rev.), yet the difference is somewhat modest in the base case. In contrast, using the more adhesive case ( $IS_{ma}$ ), it is clear that a considerably larger mixing extent is reached ( $IS_{maa} = 0.18$ ). One possible explanation for the necessity of larger adhesive forces in this case may be the following. Since our simulations contain equal parts by volume of both species, the larger size difference leads to a dramatically larger number of small particles. This skews the probability of interactions between particles such that small-small interactions happen far more frequently. Hence, our assumption of binary interactions that essentially randomly visit all possible combinations becomes less realistic. Increasing the absolute degree of cohesion, however, changes the “penalty” for choosing the more probable interaction over the more favorable so that we eventually reach the predicted state. Case  $c$  maintains the same mechanical properties as case  $a$  (i.e.,  $\beta = 0.5$  and the densities are the same), but now the smaller particles have a larger surface energy ( $\phi = 2.0$ ). In this case, the small-small interaction is predominant and the phase diagram predicts enhanced segregation (Figure 18). Interestingly, the opposite trend is seen for the base case of adhesion and the cohesive system is significantly more mixed than the free-flowing case. A possible explanation for this observation is that the interactions between small particles are so strong that they are rarely present individually, but instead form persistent clusters. These clusters are comparable in size or perhaps slightly larger than the large primary particles. Coupling this with the fact that clusters are inherently less dense (due to voids in the packing) means that these small particle clusters will tend to migrate outward. In the more adhesive case, we exacerbate this tendency so that the clusters

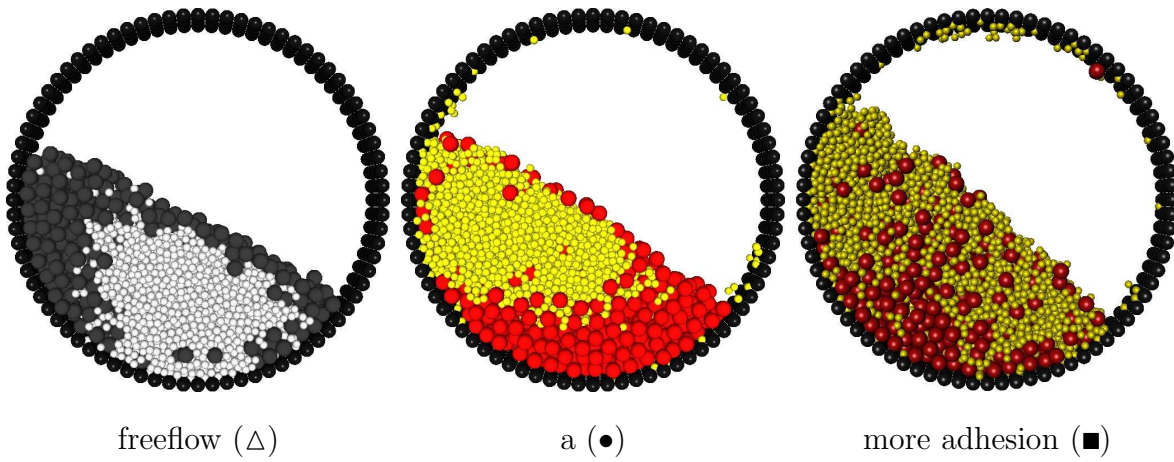
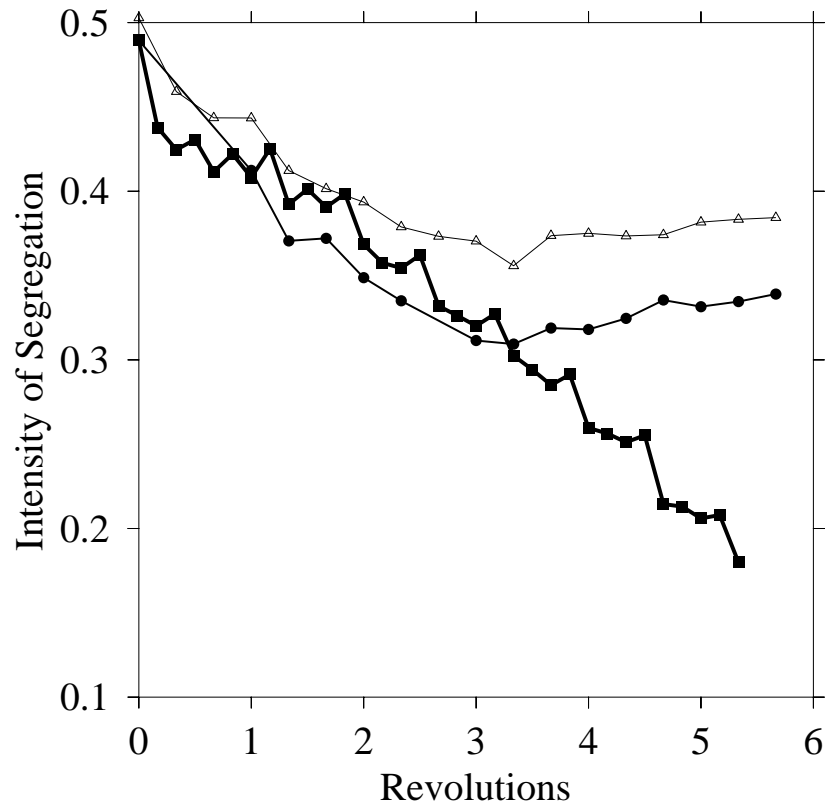


Figure 17: Mixing progress for systems corresponding to case *a* with low (●) and high (■) degree of adhesion and the corresponding free-flowing case (Δ).

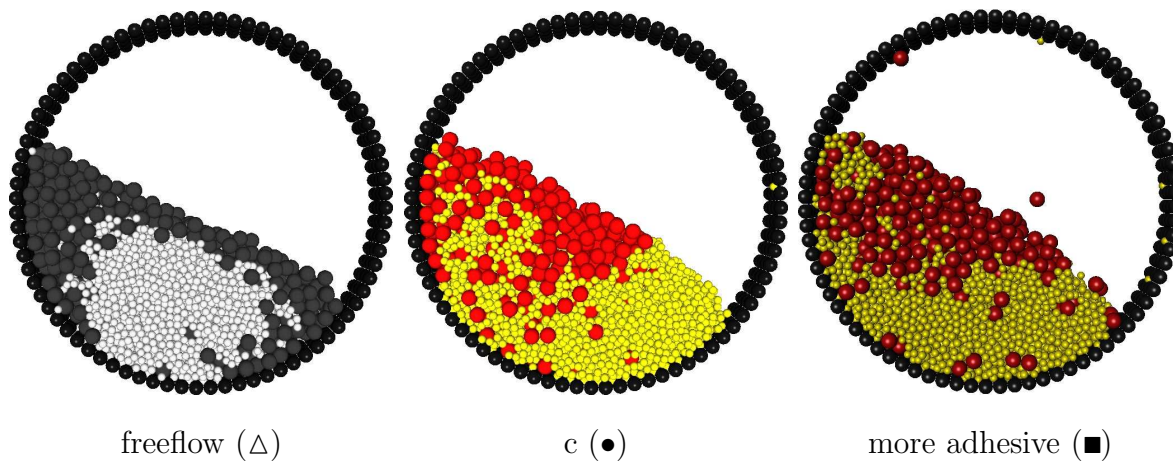
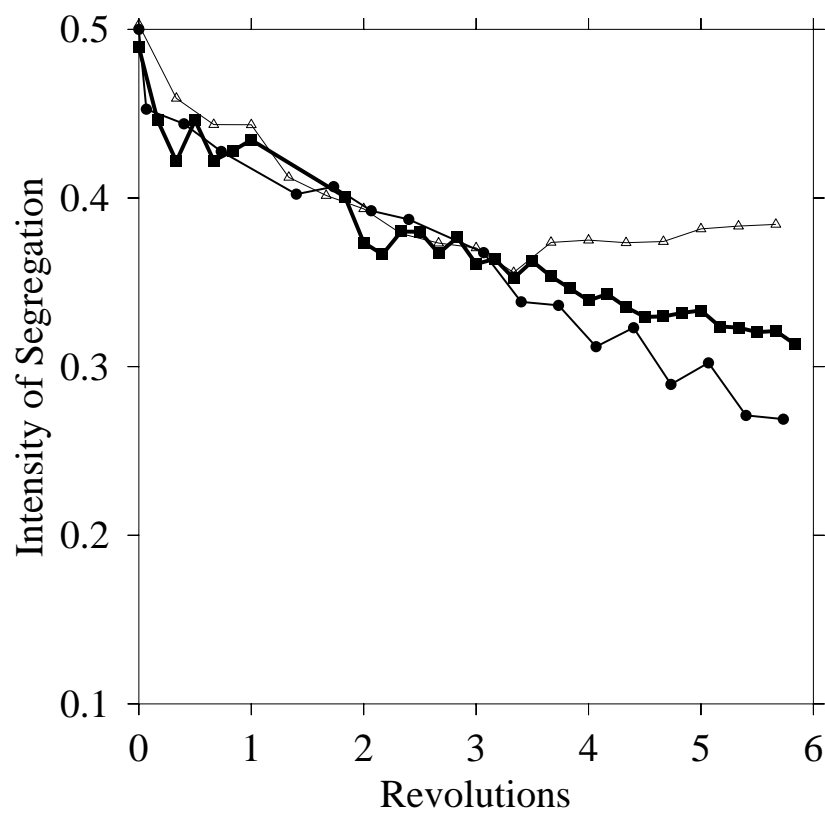


Figure 18: Intensity of Segregation for case  $c$  and all related cases.

of small particles are even larger (and still less dense) than the primary large particles so that we begin to overshoot the somewhat mixed result and move toward a segregated result.

Case *d* consists of small dense particles that segregate strongly in the free-flowing case. As with case *a*, cohesion is expected to increase the degree of mixing, yet the results for the base case are only marginally different from their free-flowing counterpart ( $IS_{ff_d} = 0.35$  and  $IS_d = 0.33$ ). In contrast, increasing the degree of cohesion again leads to a more substantial difference (Figure 20), leading to  $IS$  values below 0.3 ( $IS_{ma_d} = 0.28$ ). Finally, in case *g* (See Figure 13a and 19), segregation by density and by size lead to competing effects so that the free-flowing system reaches a low extent of mixing ( $IS_{ff_g} = 0.19$ ). Once again, for the base case, we obtain the surprising result that we observe a trend opposite of that predicted. That is, a basal level of cohesion leads to a slightly more segregated system ( $IS_g = 0.24$ ). As with the case *c*, this can likely be explained by the fact that clusters of small particles are present which skew the natural competition between the density and size segregation such that density begins to “win”. Increasing the degree of cohesion causes the “penalty” for these non-favored interactions to be larger (relative to the particle’s weight) such that the expected increase in mixing is now evident ( $IS_{ma_g} = 0.14$ ). Our results suggest the following general trend. For modest size differences, cluster formation (beyond binary interactions) may be ignored and our simple theory captures the behavior of cohesive versus free-flowing systems, regardless of absolute cohesive magnitude. As size differences increase (i.e.,  $\beta < 0.5$ ) not only does cluster formation begin to become significant, our assumption that the system is “thermalized” enough that all potential interactions have roughly the same probability of occurring randomly begins to cause difficulty. Nevertheless, even in this region of phase space, simply increasing the magnitude of the cohesive interactions has been effective in the cases studied here.

### 3.3 CONCLUSIONS

In this work we examine the effects of adhesion in particle mixing by developing a computational model capable of simulating this kind of interaction. Moreover, we introduce

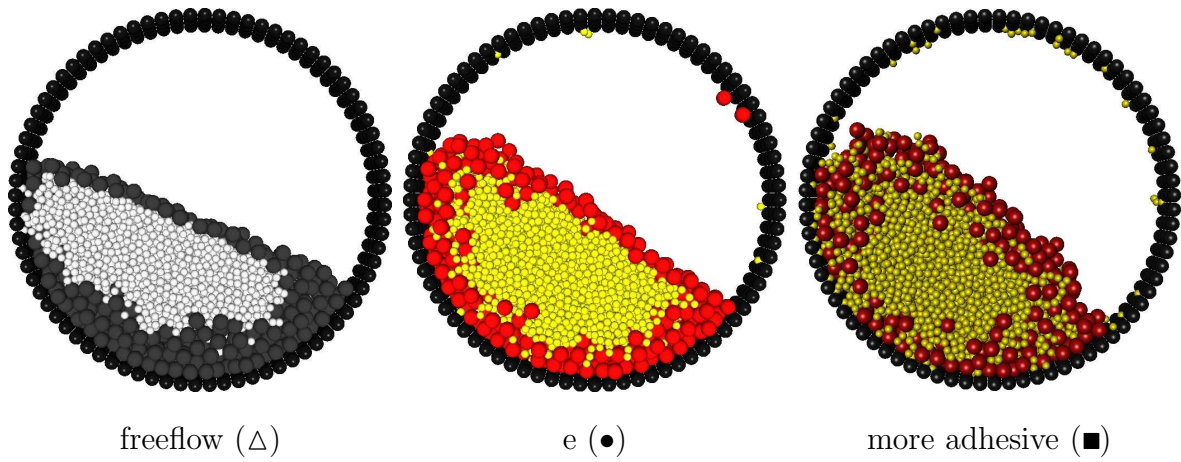
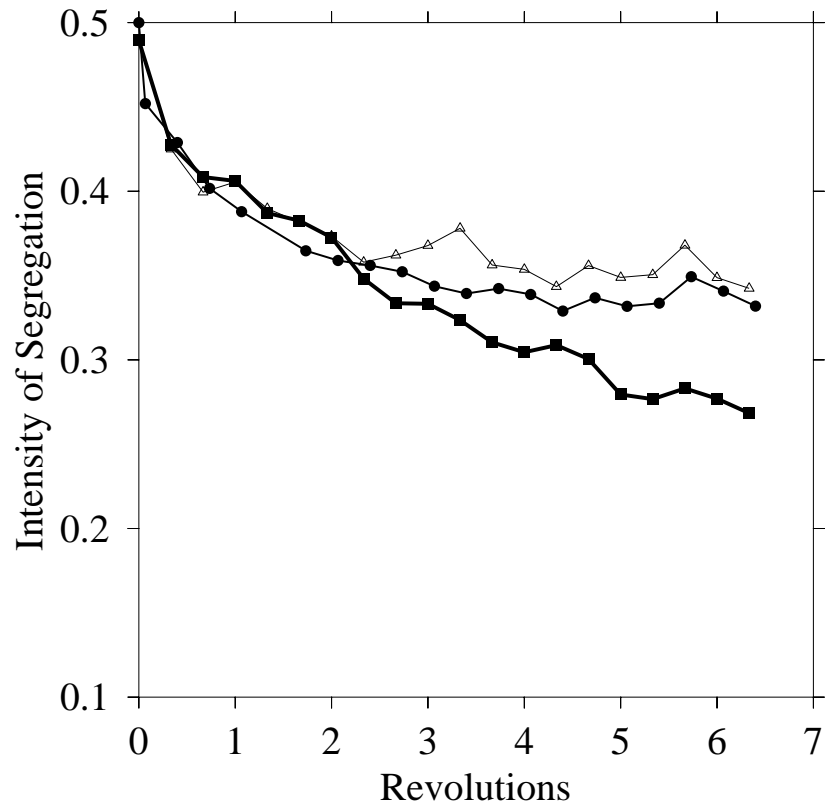


Figure 19: Mixing progress for tumbler case  $d$  with different degrees of adhesion (freeflow ( $\Delta$ ), base case ( $\bullet$ ) and more adhesion ( $\blacksquare$ )).

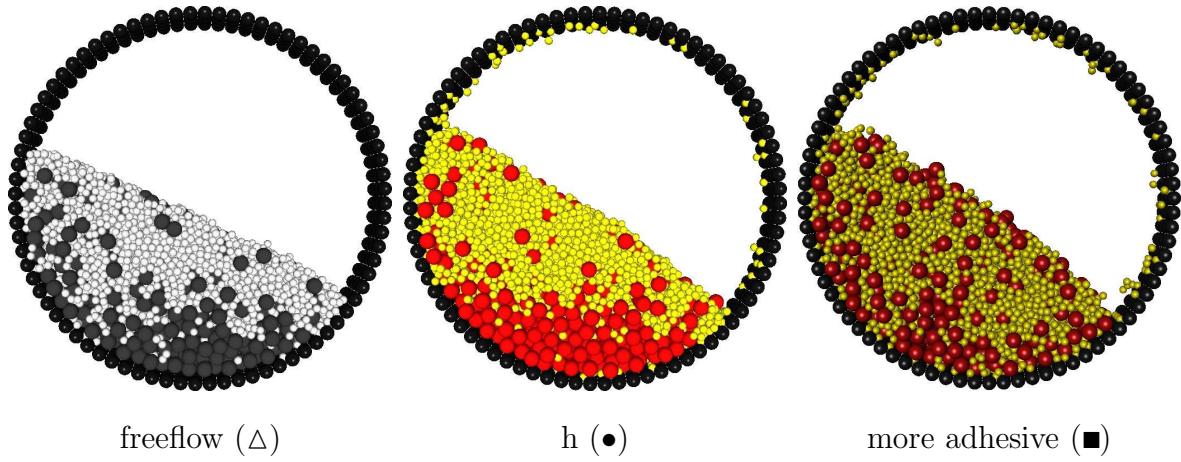
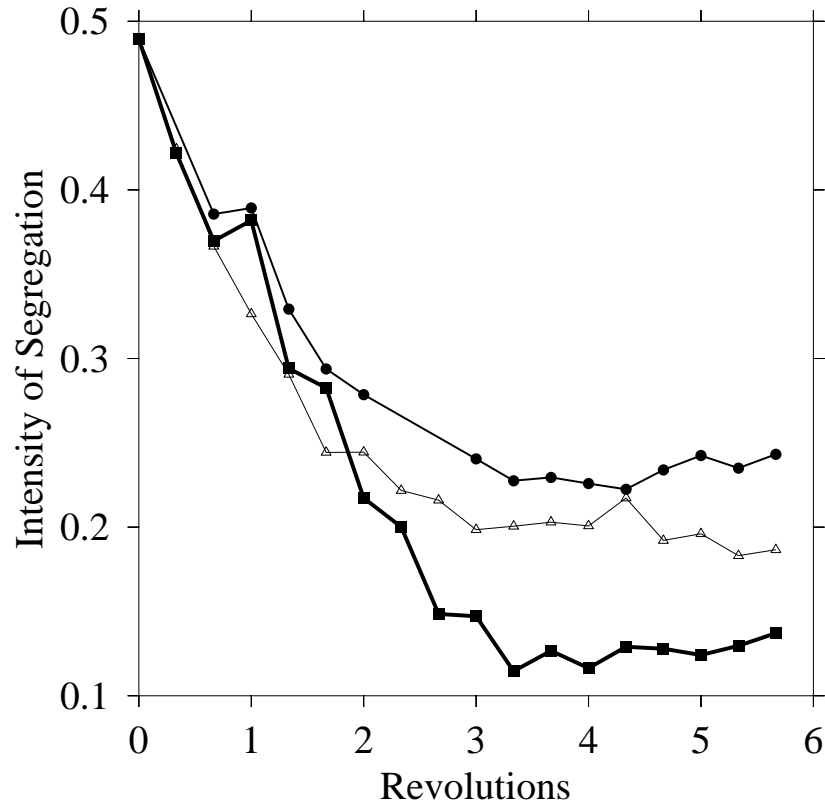


Figure 20: Mixing progress for tumbler case  $g$  with different degrees of adhesion: freeflow ( $\Delta$ ), base case ( $\bullet$ ) and more adhesion ( $\blacksquare$ ).

Table 2: Van der Waals Granular Bond numbers for cases *a*, *c*, *d*, and *g*

	freeflow			base case			more adhesive				
	<i>IS</i>	$Bo_{11}$	$Bo_{22}$	$Bo_{12}$	<i>IS</i>	$Bo_{11}$	$Bo_{22}$	$Bo_{12}$	<i>IS</i>	$\mathfrak{R}_1$	$\mathfrak{R}_2$
<b>a</b>	<b>0.38</b>	11.34	2.83	15.1	<b>0.33</b>	22.4	5.6	29.8	<b>0.18</b>	0.75	0.19
<b>c</b>	<b>0.38</b>	22.75	1.42	15.2	<b>0.28</b>	44.8	2.8	29.8	<b>0.32</b>	1.5	0.09
<b>d</b>	<b>0.35</b>	11.3	5.4	15.1	<b>0.33</b>	22.5	10.8	30.0	<b>0.28</b>	0.75	0.36
<b>g</b>	<b>0.19</b>	11.3	1.47	15.1	<b>0.24</b>	22.9	3.0	30.6	<b>0.14</b>	0.75	0.1

a characterization tool,  $Bo_{vdw_{ij}}$ , that allows us to construct phase diagrams depicting the particle/system parameters necessary to obtain mixed and segregated asymptotic results. These diagrams are based solely on scaling arguments whereby we compare the variety of potential interactions in the system. Using this model, we have shown that we can accurately predict mixing/segregation behavior for systems with relatively modest size differences (i.e., size ratios larger than 0.5) in simulated tumbler mixers. However, as the size differences become larger the absolute magnitude of the adhesive forces becomes a significant parameter as the favored interactions now need to compete with multi-particle cluster formation, as well as the relative decrease in the probability of dissimilar particle interactions. While the work presented here focuses on tumbler mixer it is entirely possible that other industrial equipment—such as a fluidized bed—may avoid some of this theoretical pitfalls altogether as the system is considerably more “thermalized” and binary collisions are much more common (a similar approach has already been shown to work for wet systems [130]). Nevertheless, our predicted trends were recovered in all cases studied here simply by increasing the degree of cohesion, suggesting that this approach may be somewhat robust to device geometry. An obvious next step in this work is to focus on overcoming the stated assumptions inherent in our analysis: namely, we need to consider multi-particle interactions, as well as incorporated particle collision statistics.

## 4.0 CONTROLLING MIXING AND SEGREGATION OF ADHESIVE GRANULAR MATERIALS

Mixing two dissimilar materials is not a trivial operation: segregation can exist when particles differ in any physical property. Segregation is a major problem in industries that rely on the creation of granular mixtures. In the pharmaceutical industry, for example, a batch that cost hundred of thousand of dollars can be rejected if the composition of as little as five tablets do not meet the FDA requirements [15]. Additionally, investing more and more energy in the process may have a counterintuitive result: more energy could lead to more segregation [16, 17]. As the particle size decreases, intermolecular interactions start playing a central role in the bulk behavior of granular materials [131] and can dramatically impact the mixing/segregation behavior [132]. These kinds of powders are commonly found in the production of pharmaceuticals, ceramics, detergents, construction, material synthesis (amongst others) and techniques for rationally controlling their mixing/segregation behavior could contribute to significant cost savings in these industries. Current strategies used to control mixing and segregation depend on the kind of material, but the most common practices consist of reducing or increasing the particle size, changing the particle properties and/or modifying the handling/operating equipment [15, 101, 102, 100]. Recently, however, manipulating cohesion has been suggested as a means of attaining this control. For instance, adding a small amount of liquid can help to reduce the relative movement of particles by introducing capillary cohesive forces between particles. Kudrolli [117] *et al.* studied the effect of the moisture content on the degree of segregation of a bidisperse mixture of powders that is poured from a hopper. For small volume fractions of fluid, they found that segregation was mitigated by viscous and capillary forces and, when the moisture content was increased, they report a transition back to a segregated state. Geromichalos [118] identified

three different regimes—viscoelastic, gaseous and intermediate—of the dynamic behavior of vibrated wet granular materials, which determine the effect of incrementing the moisture content on the degree of mixing of a jar containing glass particles of two different radius. A more general approach was adopted by Li *et al.* [106, 124] where the mixing degree of binary mixtures of particles of different sizes, densities and hydrophobicities is predicted from the physical properties of the powders. They predict the asymptotic state of a wet particle system based on a dimensionless number, the Granular Bond Number ( $Bo_{ij}$ ), and compare their theoretical predictions with experimental results. An analogous approach for dry adhesive granular materials is shown in ref. [132], where bond number predictions are compared with DEM simulated systems dominated by these kind of adhesive interactions. The results show that as the dry adhesive forces become dominant, the predicted asymptotic states become clearer. In this Chapter, we propose a strategy to control mixing of granular materials by adding “surfactant/extractant aids”. Surfactant particles will be used to mitigate segregation, whereas extractants have the opposite purpose. Practical applications of this mixing/segregation strategy can be found, for example, in the pharmaceutical industry. The use of micron sized particles can favor the dissolution rate of a given active component in a tablet at the same time that the quality of mixing is critical to the efficacy of the product. In order to control mixing and segregation, we will first analyze all possible particle-particle interactions in a given system to *a priori* determine (from its physical properties) its mixing/segregation tendency and design the appropriate particles that can transform this asymptotic state. Our predictions will be compared with Particle Dynamics (PD) simulations of mixing tumbler containing these materials.

## 4.1 THEORY

### 4.1.1 Granular Bond Number for binary systems with Janus beads

In order to analyze systems containing these “helper particles” we need now to extend the Granular Bond Number concept to interactions that are bridged by Janus particles—i.e.

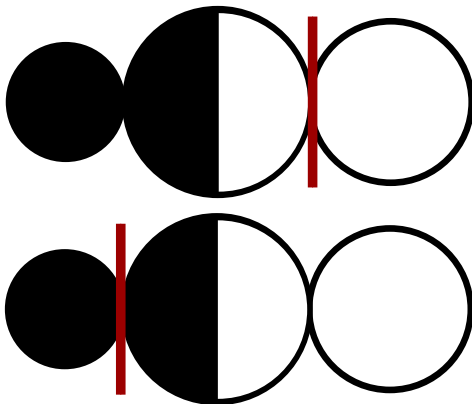


Figure 21: The strength ( $Bo_{iJj}$ ) of a Janus particle interaction is calculated as the weakest interaction where the bridge can break.

ternary interactions. These interactions are of the form ‘particle  $i$ —Janus—particle  $j$ ’ ( $iJj$ ), where  $i$  or  $j$  are particles of type 1 or 2. If we call  $A$  and  $B$  the Janus’s hemisphere in contact with  $i$  and  $j$  respectively, the Granular Bond number can be expressed as:

$$Bo_{vdw1J2} = \text{Min} \left\{ \frac{F_{vdw1A}}{\text{Min}(W_1, W_2 + W_J)}, \frac{F_{vdw2B}}{\text{Min}(W_1 + W_J, W_2)} \right\}. \quad (4.1)$$

That is, the idea behind the  $\text{min}()$  operator is that the strength of the Janus-bridged interaction between  $i$  and  $j$  is determined by the weakest bond that links the interaction (See Figure 21). Expressions for all possible interactions in the system are summarized in Table 3. In general, we expect the concentration of Janus particles to be small enough that the probability of one Janus particle interacting with another is negligible.

#### 4.1.2 Phase Diagrams

The predicted asymptotic behavior of the binary+Janus systems is calculated in the same manner as in the purely binary case, that is, by comparing and scaling all existing bonding forces. Based on the possible interactions in these systems, the strengths of those that promote mixing ( $Bo_{12}$ ,  $Bo_{1J2}$  and  $Bo_{2J1}$ ) are compared with the ones that enhance segregation

Table 3: Summary of Granular Bond Numbers for systems containing Janus Particles

Bond Number	Interactions	Expression
$B_{Ovdw_{11}}$		$\frac{F_{vdw_{11}}}{W_1}$
$B_{Ovdw_{22}}$		$\frac{F_{vdw_{22}}}{W_2}$
$B_{Ovdw_{12}}$		$\frac{F_{vdw_{12}}}{\min(W_1, W_2)}$
$B_{Ovdw_{1J1}}$		$\min\left\{\frac{F_{vdw_{1B}}}{W_1}, \frac{F_{vdw_{1A}}}{W_1}\right\}$
$B_{Ovdw_{2J2}}$		$\min\left\{\frac{F_{vdw_{2B}}}{W_2}, \frac{F_{vdw_{2A}}}{W_2}\right\}$
$B_{Ovdw_{1J2}}$		$\min\left\{\frac{F_{vdw_{2B}}}{\min(W_2, W_1 + W_J)}, \frac{F_{vdw_{1A}}}{\min(W_1, W_2 + W_J)}\right\}$
$B_{Ovdw_{2J1}}$		$\min\left\{\frac{F_{vdw_{1B}}}{\min(W_2, W_1 + W_J)}, \frac{F_{vdw_{1A}}}{\min(W_1, W_2 + W_J)}\right\}$

( $Bo_{11}$ ,  $Bo_{22}$ ,  $Bo_{1J1}$  and  $Bo_{2J2}$ ). Janus particles are added either to enhance mixing in an adhesive system that would otherwise tend to segregate or *vice-versa*. In the first case, we say that the Janus particles act as a *surfactant* because they promote mixing of two (granular) phases that would be ‘immiscible’ otherwise. The latter corresponds to *extractant* particles that are used to recover a component from a mixture. More formally, we can express the functionality of these helper particles as:

$$\text{Janus Particle} = \begin{cases} \text{Surfactant,} & \text{if } \max(Bo_{ij}) \in \{Bo_{11}, Bo_{22}\} \text{ and} \\ & \text{if } \max(Bo_{ij}, Bo_{iJj}) \in \{Bo_{1J2}, Bo_{2J1}\} \\ \text{Extractant,} & \text{if } \max(Bo_{ij}) = Bo_{12} \text{ and} \\ & \text{if } \max(Bo_{ij}, Bo_{iJj}) \in \{Bo_{1J1}, Bo_{2J2}\} \end{cases} \quad (4.2)$$

Next, we aim to determine for which systems (if any) represented in the phase-space diagrams constructed for the binary systems, it is possible to find surfactants/extractants. Let the dimensionless properties of a Janus particle be defined analogously to those for the binary case:  $\alpha_J = \rho_J/\rho_2$ ,  $\beta_J = R_J/R_2$ ,  $\phi_A = \sqrt{\Gamma_{AA}/\Gamma_{22}}$  and  $\phi_B = \sqrt{\Gamma_{BB}/\Gamma_{22}}$ , corresponding to the dimensionless size, ratio and surface energy of each of the hemispheres of the Janus particle, respectively. It is clear that, although our simulation technique can be used to simulate systems with a wide range physical parameters, the actual values of a particles’s physical properties that can be found in real applications is limited. For this reason, we have arbitrarily defined a domain for  $\alpha_J$ ,  $\beta_J$ ,  $\phi_A$  and  $\phi_B$  as:

$$0.2 < \alpha_J < 4.0 \quad (4.3)$$

$$0.2 < \beta_J < 4.0$$

$$0.0 < \phi_i < 10.0$$

that limits the availability of functional Janus particles we will use. In Figure 22, the E region (binary systems that segregate) have been covered with open symbols if it is possible to use Janus particles to enhance mixing, i.e. there is at least one set of Janus particle’s properties that satisfies equation 4.3 and the surfactant conditions in equation 4.2. We refer to this region as the **Janus surfactant region**. In the M region (containing those cohesive systems that are expected to mix), closed symbols have been placed only if it is possible

to use Janus beads to promote segregation. Again, this means that it is possible to find particles that are in the set defined by equation 4.3 and satisfies the extractant condition in equation 4.2. In the same manner, we call this the **Janus extractant region**. According to this, for every adhesive system predicted to mix in Figure 22, it is possible to find Janus beads that would serve as extractant particles. In contrast, only for a reduced space in the region where segregation of adhesive particles is predicted (E Region in 22) can Janus beads act as surfactants.

In the section 4.2, we choose binary systems in the surfactant/extractant regions and attempt to modify their asymptotic state by adding Janus particles.

### 4.1.3 Selection of Janus Beads properties

Although the dimensionless properties of particles 1 and 2 have been set for each point in Figure 22, the Janus particle's properties have not and they must be chosen to favor the desired final state. For each of the selected systems, Figure 23 shows the domain of densities and sizes of functional Janus particles (if surface energy are chosen appropriately). Two more degrees of freedom remain to be covered, namely the surface energy ratios of the two faces of the Janus particles. Once the size and density of the Janus particle have been selected, again the values for  $\phi_A$  and  $\phi_B$  are set to satisfy the functional restrictions in equation 4.2. Figure 24 displays the  $\phi_A$ - $\phi_B$  feasible plane for the cases selected in Figure 23 and points out the particle properties we simulate in the next section. Note that the helper particles with surfactant properties must, in fact, be Janus (i.e., have two different hemispheres), since no feasible point falls on or near  $\phi_A=\phi_B$ . On the contrary, for the extractant case it is possible to use regular (symmetric) helper particles because  $\phi_A=\phi_B$  is included in the feasibility region.

The selection is based on three criteria:

(i) if the ratio of mixing interactions to the segregation interactions ( $\mathfrak{R}_J$ ) is defined as:

$$\mathfrak{R}_J = \frac{\max(B_{O_{12}}, B_{O_{1J_2}}, B_{O_{2J_1}})}{\max(B_{O_{11}}, B_{O_{22}}, B_{O_{1J_1}}, B_{O_{2J_2}})} \tag{4.4}$$

Janus-surfactants are chosen to maximize  $\mathfrak{R}_J$  and Janus-extractants to maximize  $\mathfrak{R}_J^{-1}$

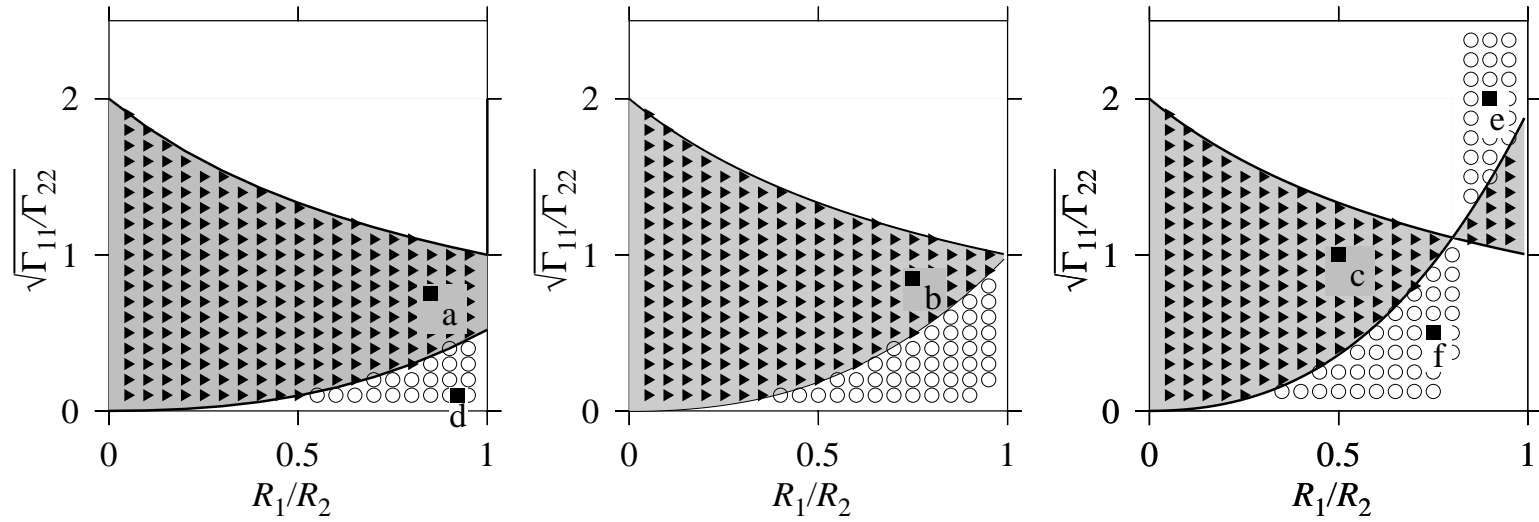


Figure 22: Phase-space diagrams for van der Waals adhesive systems with Janus beads. The binary phase-space diagram shows in grey the region corresponding to the materials that tend to mix and closed symbols have been placed if Janus can be used as extractant ( $\blacktriangleright$ ). The white region indicate systems that tend to segregate and open symbols cover the Janus surfactant ( $\circ$ ) region.

- (ii) we try to avoid dramatic size differences because they promote cluster formation and multi-particle interactions, two phenomena which are beyond the scope of our theory
- (iii) we choose (when possible) low  $B_{OJJ}$  values to avoid the formation of clusters of Janus particles (i.e., particle “micelles”) that would reduce their activity in the bed

Figure 23 suggests that extractant particles tend to be more massive (higher  $\alpha_J\beta_J$ ) while surfactant particles are lighter. An explanation can be as follows. Lets consider a system where Janus beads are used as surfactants and the interaction  $aJb$  is the dominant interaction. We can choose  $a, b, A, B$  such as

$$B_{O_aJb} = \min \left\{ \frac{F_{vdwaA}}{\min(W_a, W_a + W_J)}, \frac{F_{vdwbB}}{\min(W_b + W_J, W_b)} \right\} = \frac{F_{vdwaA}}{\min(W_a, W_b + W_J)}, \quad (4.5)$$

in that system there is also a segregating interaction  $aJa$  for which,

$$B_{O_aJa} = \min \left\{ \frac{F_{vdwaA}}{W_a}, \frac{F_{vdwaB}}{W_a} \right\} \geq \frac{F_{vdwaA}}{\min(W_a)}. \quad (4.6)$$

In order to avoid segregation, the mixing interaction must predominate ( $B_{O_aJb} > B_{O_aJa}$ ), for which we need at least that  $W_b + W_J < W_a$ . That lead us to two cases,

$$\begin{aligned} \text{if } a = 1 \wedge b = 2 & \quad \alpha\beta^3 + \alpha_J\beta_J^3 > 1 \\ & \quad \alpha_J > \frac{1 - \alpha\beta^3}{\beta_J^3} \\ \text{if } a = 2 \wedge b = 1 & \quad \alpha\beta^3 + \alpha_J\beta_J^3 > 1 \\ & \quad \alpha_J > \frac{\alpha\beta^3 - 1}{\beta_J^3} \end{aligned} \quad (4.7)$$

that correspond to the curve that seem to define a extractant/surfactant boundary. The extractant case can be explained in an analogous manner.

Janus particles used to enhance mixing/segregation act under the same principle as surfactants and extractants do to increase the solubility of two immiscible liquid phases or recover a component from a mixture, that is, using molecule groups (or in this case particle hemispheres) with different affinity to favor interactions between different components (extractants) or to generate interactions that prevail over those that promote the mixture (surfactant). As in the surfactant/extractant case, they can not be removed from the mixture. However, in industrial powders it is common to find components that perform a

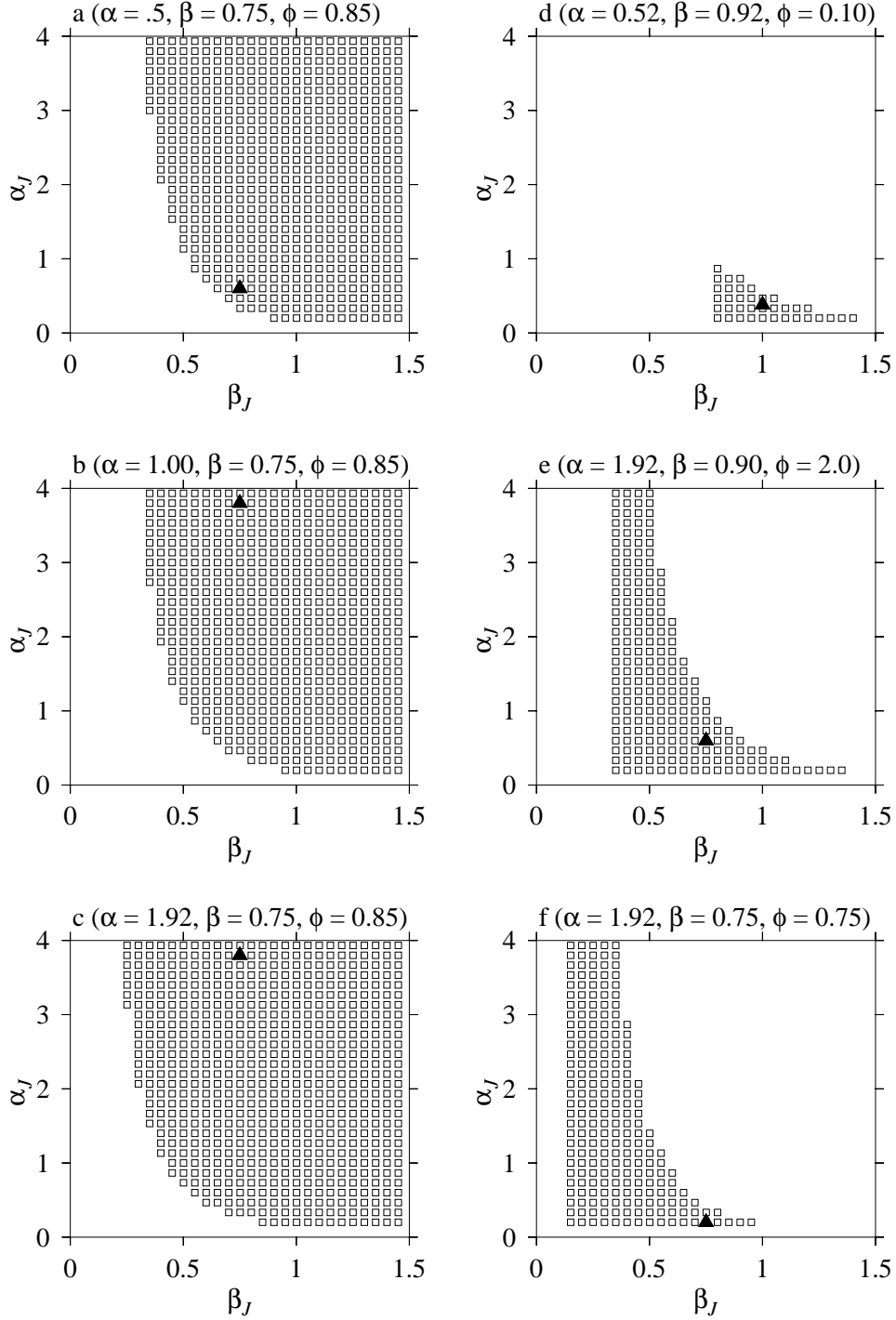


Figure 23: Density-size feasible values for extractant (left) and surfactants (right) Janus particles for binary systems chosen in Figure 22, respectively. Open circles indicate the existence of functional (extractant/surfactant) Janus particles with those density and size properties, if surface energies are chosen appropriately. In each case, a closed symbol indicate the properties chosen for PD simulations.

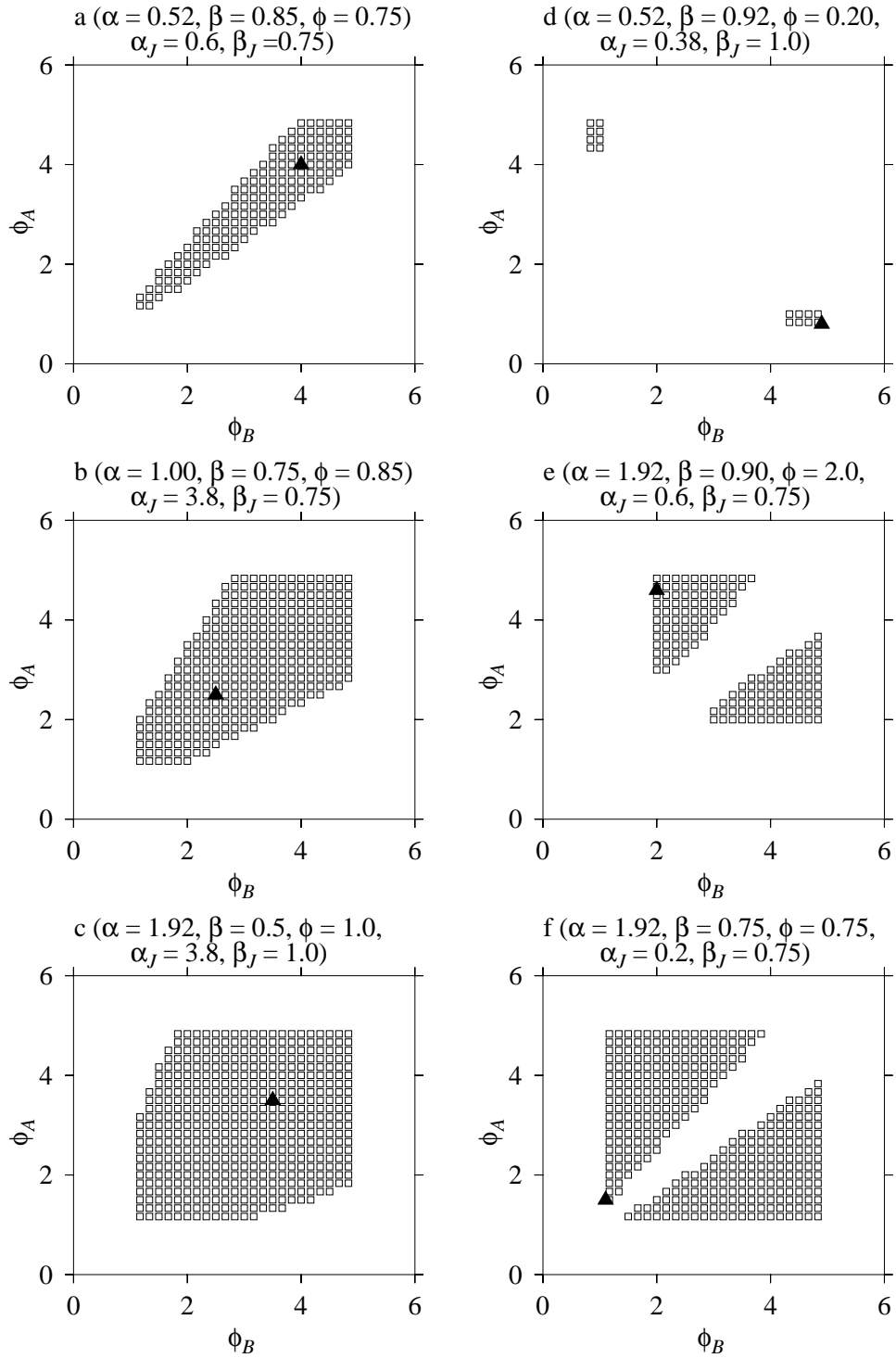


Figure 24: Allowed values of surface energies for extractant (left) and surfactant (right) Janus particles for systems shown in Figure 22. These  $\phi_A$ - $\phi_B$  values correspond the surface energy ratios that will lead to functional particles with the densities and sizes selected in Figure 23.

Table 4: PD simulation parameters for tumbler simulations

particle diameter	4[mm]
density	1000[ $Kg/m^3$ ]
Young’s modulus	30[MPa]
Surface energy	0.2–1.6[ $J/m^2$ ]
Poisson ratio	0.3
friction coefficient	0.35

secondary function and contribute to their handling and processing—such as glidants to improve flowability, lubricants to facilitate tableting, binders to granulate, desintengrants to promote their tablet breakage (e.g. in the gastric system), flavors, etc.

## 4.2 TUMBLER SIMULATIONS

Our focus now is to control mixing of dry adhesive granular material in a rotating tumbler. In the following results, the initial condition (mixed/segregated) for our simulations is varied in order to show the effect of the presence of the Janus particles and is chosen based on the predicted asymptotic state of each system. In cases where the material is initially segregated, the light (small) and dark (large) particles are located in each—left/right—half of the tumbler. Initially mixed material is achieved by randomly placing the particles inside the tumbler and allowing them to settle under gravity. The tumbler diameter is equal to 40 times the particle diameter and the rotation rate is 5[rpm]. We consider base particle properties (or our base case) those in Table 4. These particle properties are varied according to the dimensionless values indicated in the phase-space diagrams  $(\alpha, \beta, \gamma)$  to lead to particle systems with the required differences in size, density and surface energy.

Table 5: Summary of Granular Bond Numbers for systems containing Janus Particles

	Extractants			Surfactants		
	a	b	c	d	e	f
Binary system						
$\alpha$	0.52	1.00	1.92	0.52	1.92	1.92
$\beta$	0.85	0.75	0.50	0.92	0.92	0.75
$\phi$	0.75	0.85	1.00	0.1	2.0	0.75
$Bo_{11}$	3.72	1.60	0.78	0.08	1.69	1.29
$Bo_{22}$	2.48	1.24	0.75	3.29	0.66	2.48
$Bo_{12}$	5.36	2.15	1.46	0.78	1.25	1.97
Systems with Janus Beads						
$\alpha_J$	0.6	3.80	3.80	0.38	0.6	0.2
$\beta_J$	0.75	0.75	1.00	1.0	0.9	0.75
$\phi_A$	4.0	2.5	3.5	4.9	2.0	1.5
$\phi_B$	4.0	2.5	3.5	0.8	4.6	.1
$Bo_{1J1}$	18.6	4.69	5.13	0.62	1.54	1.9
$Bo_{2J2}$	2.48	2.66	2.61	2.63	1.13	2.34
$Bo_{1J2}$	14.9	2.66	2.61	3.36	1.72	2.59
$Bo_{2J1}$	14.9	2.66	2.61	0.62	1.13	1.89
Interactions between Janus Beads						
$Bo_{J_A J_A}$	11.7	2.29	3.07	10.5	0.29	1.65
$Bo_{J_A J_B}$	11.7	2.29	3.07	1.6	0.67	1.21
$Bo_{J_B J_B}$	11.7	2.29	3.07	0.27	1.55	0.89

For each of the cases to be studied, at least two cases are considered: an adhesive case and a system with Janus particles. All particle properties in the adhesive case are identical to those of particles 1-2 in the Janus beads system. In some cases, more than one Janus system is presented to explore the effect of the initial conditions or the number of Janus particles. The  $IS$  values mentioned in the next sections correspond to the average of the last half revolution presented in the plots. The subscripts  $wo/J$  and  $w/J$  correspond to the adhesive case without Janus beads and the system with Janus beads, respectively. *MIX* and *SEG* stand for a initial state of the system.

#### 4.2.1 Extractant particles

In this section, we focus on binary adhesive systems that tend to mix and explore how Janus particles can be used in these cases to prevent these systems from mixing or to separate systems that have been already mixed. According to Figure 22, this is the case of systems *a*, *b* and *c*.

In case *a* (Figure 25), smaller particles are less dense ( $\alpha = 0.52$ ,  $\beta = 0.85$ ), so that a free-flowing system would mix (not shown). Similarly, Figure 22 predicts that an adhesive system would also mix under these conditions, as our results confirm ( $IS_{wo/J_a} = 0.2$ ). We attempt to then separate these materials by using Janus particles of a size and density ratio of  $\alpha_J = 0.6$ ,  $\beta_J = 0.75$ . The lower density of the Janus particles tends to drive them to the periphery of the drum. This should facilitate the predominant interaction  $1J1$ . Here (Figure 25) we show results for both initially segregated as well as initially mixed cases. For the system that is initially segregated the Janus particles seem to increase the degree of segregation very slightly; however, if we instead examine the initially mixed case, the Janus beads appear to be unable to achieve separation. In this case, we must conclude that Janus beads have little or no effect. This can be understood by virtue of the fact that the dominant segregation Bond number,  $Bo_{1J1} = 18.6$ , is in fact comparable in magnitude to the largest mixing Bond number  $Bo_{1J2} = Bo_{2J1} = 14.9$ , thus the bias expected due to these interactions is negligible.

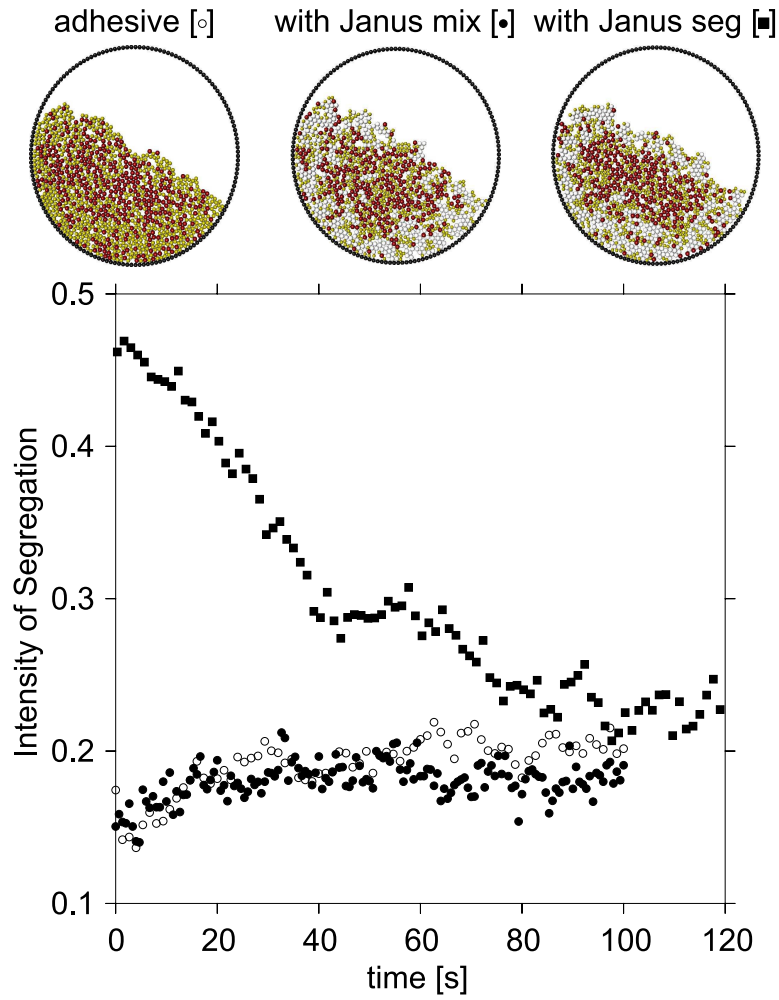


Figure 25: Intensity of Segregation and tumbler snapshots for system *a*. Snapshots for adhesive without Janus particles [o] and systems with Janus particles when the initial state is mixed [•] and segregated [■].

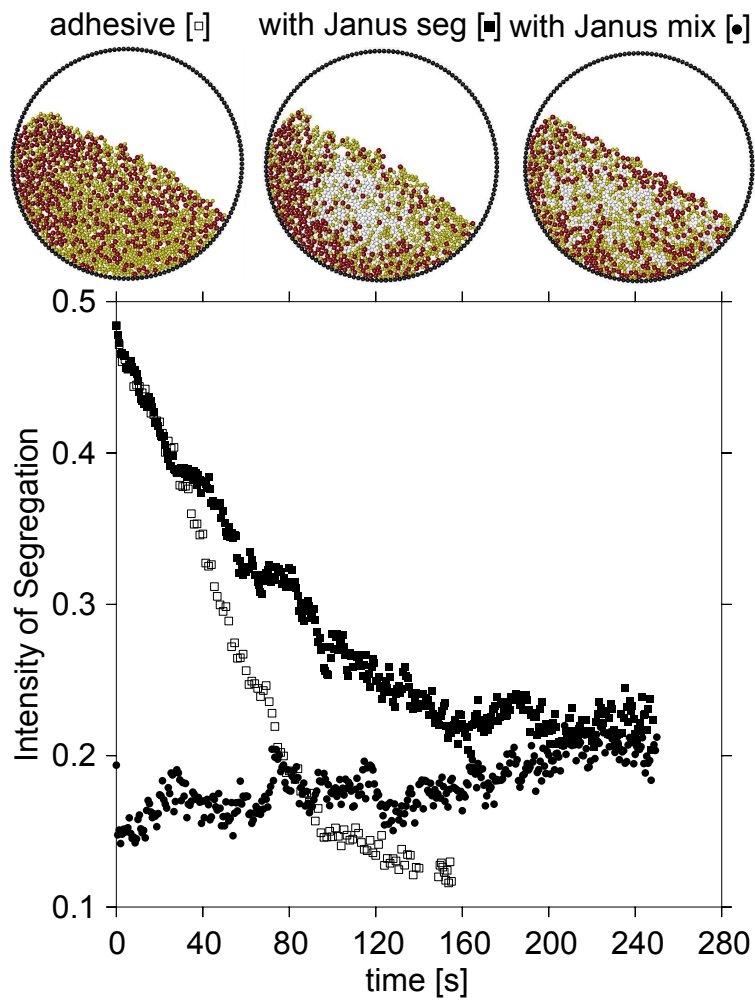


Figure 26: Intensity of Segregation and tumbler snapshots for system *b*. Snapshots adhesive without Janus particles [□] and systems with Janus particles when the initial state is mixed [●] and segregated [■] .

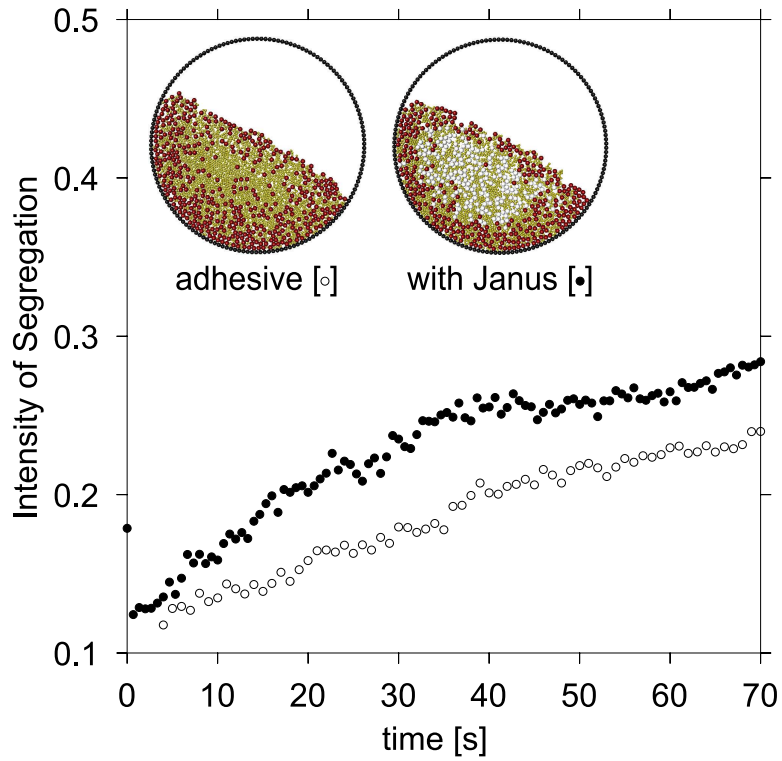


Figure 27: System *c*: Intensity of Segregation and respective snapshots for adhesive case without Janus particles [o] and with Janus particles [•].

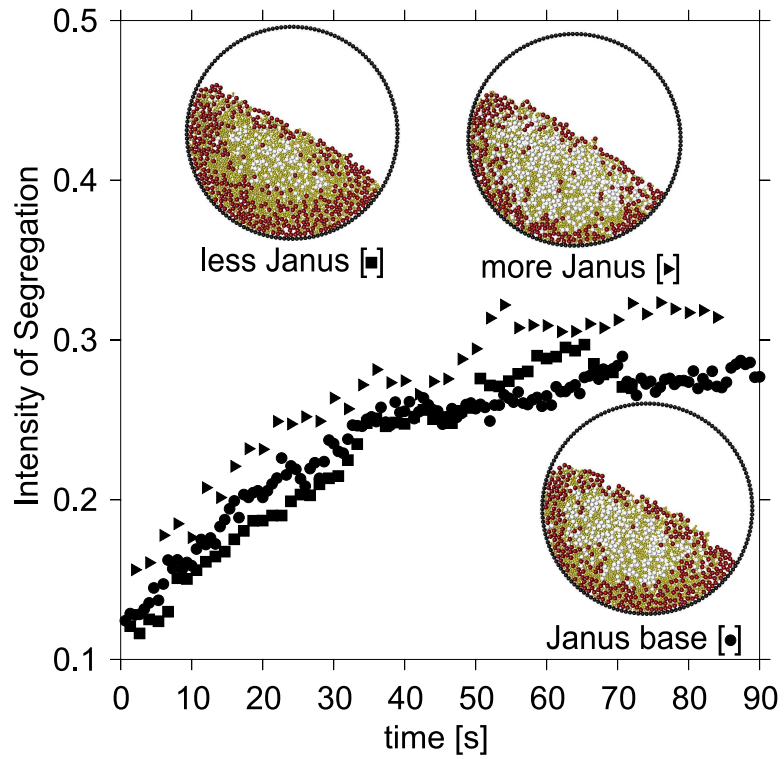


Figure 28: System *c*: Intensity of Segregation and respective snapshots for system *c* with less [■], base [●] and more [►] Janus particles.

System *b*, in contrast, achieves almost a two-fold difference between mixing and segregation Bond numbers. This system consists of particles with the same densities and a size ratio of  $\beta = 0.75$ . The free-flowing case again would achieve a mixed state (not shown), as does the binary adhesive case, as predicted Figure 26. Again comparing both an initially segregated and initially mixed Janus system yields slightly differing results. Here, the system contains Janus particles of properties  $\alpha_J = 3.8$ ,  $\beta_J = 0.75$ ,  $\phi_A = \phi_B = 2.5$ . The dominant interaction in the Janus system is the interaction  $1J1$  and therefore Janus particles are expected to agglomerate and collect the smaller particles in the inner core (where Janus also would tend to migrate because of their significantly higher density). In the initially segregated case, the mixing evolution shown in Figure 26 clearly demonstrates how the rapid drop in the  $IS$  value for the binary adhesive system does not occur when Janus particles are present (i.e., the mixing *rate* is dramatically decreased). Moreover, the asymptotic state reached by the system with Janus beads is more segregated than that of the binary case. This is confirmed by the  $IS$  values ( $IS_{w_o/J_b} = 0.13$ ,  $IS_{w/J_{b_{SEG}}} = 0.23$ ). Interestingly, in the case of the initially premixed system, the Janus beads are able to achieve a similar degree of separation over the time-scale simulated here ( $IS_{w/J_{b_{MIX}}} = 0.20$ ,  $IS_{w/J_{b_{SEG}}} = 0.23$ )

Next, we simulate a system with a size and density ratio of  $\beta = 0.5$  and  $\alpha = 1.92$  (system *c*, Figure 27), respectively. All systems in this case are initially mixed. Here the free-flowing case would result in a strongly segregated system because both segregation by size and density drive the small particles to the core. In the adhesive case, however, the interactions between smaller and large particles are enhanced, and segregation (as predicted) is mitigated ( $IS_{w_o/J_c} = 0.26$ ). The properties of the Janus beads used are  $\alpha_J = 3.8$ ,  $\beta_J = 1.25$ ,  $\phi_A = \phi_B = 0.95$ . The dominant Bond Number is  $Bo_{1J1}$ , and the Janus particles are larger but conveniently much more dense than the other particles in the system. This higher density promotes their migration to the inner core so that this system exhibits small-Janus-small particle bridges, where these clusters segregate to the inner core (without Janus,  $IS_{w_o/J_c} = 0.26$ ; with Janus,  $IS_{w/J_c} = 0.29$ , Figure 27). Note that in this case the dominant interaction  $Bo_{1J1} = 5.1$  is again approximately twice as high as the largest mixing interaction  $Bo_{1J2} = Bo_{2J1} = 2.6$ .

Finally, in an effort to gain insight into the proper number of Janus beads to be used in an extractant effort, we consider two additional systems containing identical types of particles but a different proportion of Janus. In the case shown in Figure 27, 19.2% of the total occupied area corresponds to Janus particles. In Figure 28, we study the effect of a higher (33.5%) and lower (9.1%) proportion of Janus particles. By increasing the proportion of Janus particles from 9.1% to 19.2%, no significant difference arises in the asymptotic state (Figure 27, ( $IS_{w/J_c} \approx IS_{w/J_{c--}} = 0.29$ )); however, if the Janus particle concentration is further increased, a better degree of separation can be reached ( $IS_{w/J_{c++}} = 0.31$ ) giving a more efficient separation alternative. Nevertheless, this increased concentration of Janus beads not only would prove more costly in materials, but also would decrease the volume available for mixed product. Hence, we expect that a balance can be struck when choosing an appropriate number of Janus beads to use.

#### 4.2.2 Surfactant particles

Surfactant particles are used to enhance mixing in systems  $d$ ,  $e$  and  $f$  as shown in Figure 22. The domain where the surfactant particles can be used is reduced and it is located close to the boundaries between the M and E regions of the adhesive phase-space diagrams. This means that the systems for which we can enhance mixing are in a limited domain and in most cases correspond to systems that typically only mildly segregate. Moreover, we have a smaller window of choices for the feasible Janus bead properties.

Case  $d$  corresponds to a case where the less dense particles have a slightly smaller size ( $\alpha = 0.52$ ,  $\beta = 0.92$ ). The free-flowing as well as the system with no Janus particles tend to radially segregate. The feasibility domain depicted in Figure 23 and Figure 24 severely restricts the properties of the Janus beads that can be chosen and make the selection of Janus particles that would lead to a high  $Bo_{J_i J_i}$  unavoidable (i.e., the systems will essentially always form strong particle micelles). We have simulated a system within this domain with a predominant mixing interaction of  $Bo_{1J_2} = 3.36$ , but, unfortunately with a correspondingly high  $Bo_{J_A J_A} = 10.5$ . The Janus particles in this case tend to cluster together and are not effective as mixing agents (not shown).

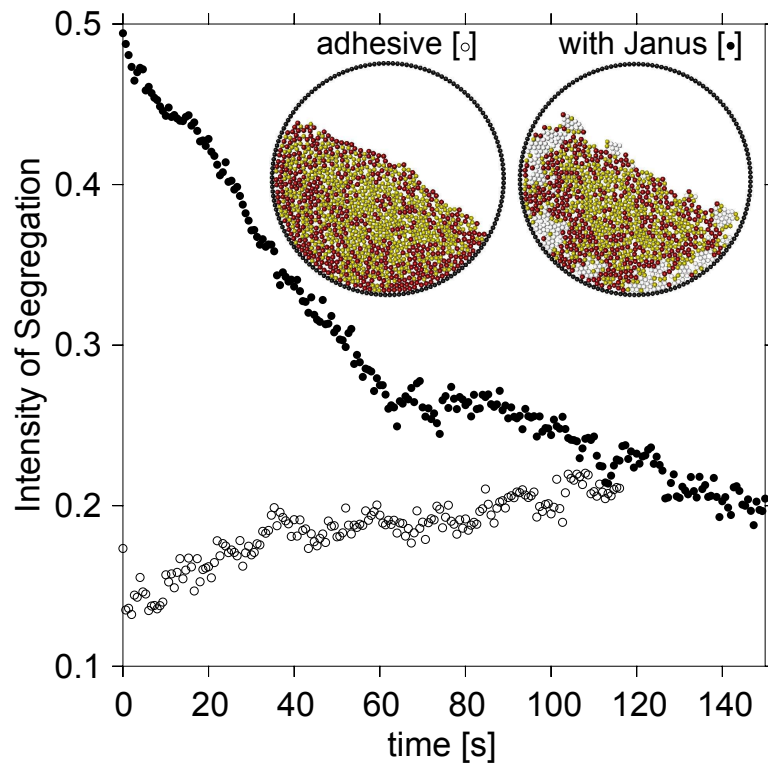


Figure 29: Intensity of Segregation for system  $e$  and respective snapshots for adhesive case without Janus particles [o] and with Janus particles [•].

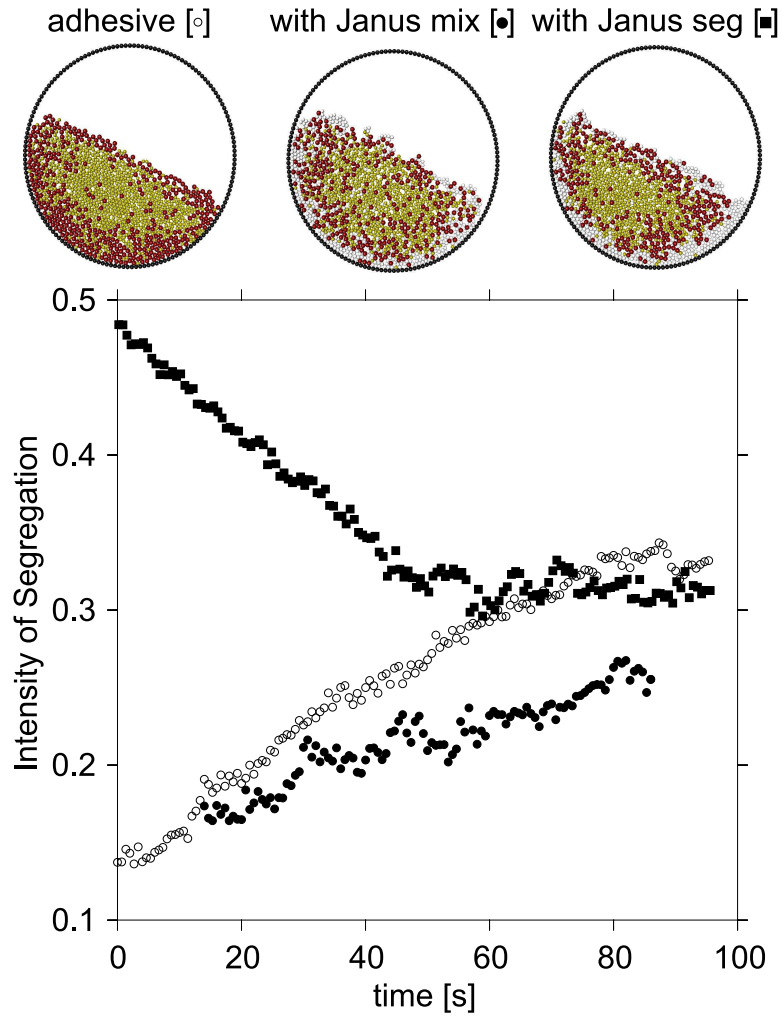


Figure 30: Intensity of Segregation and tumbler snapshots for system  $f$ . Snapshots for adhesive without Janus particles [o] and systems with Janus particles when the initial state is mixed [•] and segregated [■].

System  $e$  correspond to a case where the smaller particle is more dense ( $\alpha = 1.92$ ,  $\beta = 0.92$ ). Because of the density difference, and the fact that the smaller particle is the one that has a higher surface energy, the adhesive case mildly segregates. In this case, we show how an initially segregated system mixed in the presence of the Janus particles ( $\alpha_J = 0.6$ ,  $\beta_J = 0.9$ ,  $\phi_A = 2.0$ ,  $\phi_B = 4.0$ ). The predominant Bond number is  $Bo_{1J2}$ , however, due to the fact that the ratio between this and the largest segregation interaction is less than a factor of two, not surprising, the increase in mixedness is small (without Janus,  $IS_{wo/J_e} = 0.22$ ; with Janus,  $IS_{w/J_e} = 0.20$ ) over the time-scale simulated here.

Finally, in case  $f$  ( $\alpha = 1.92$ ,  $\beta = 0.75$  and  $\phi = 0.75$ ), the smaller particles are more dense, and both segregation by size and density drive the smaller (lighter) particles to the inner core and the larger and more dense to the periphery. This leads to segregation in both the free-flowing and binary adhesive cases (Fig.30,  $IS_{wo/J_f} = 0.34$ ), as predicted by the phase-space diagram. The Janus particles selected for this case are  $\alpha_J = 0.2$ ,  $\beta_J = 0.75$ ,  $\phi_A = 1.5$ ,  $\phi_B = 1.1$ . Note that the feasible density values are low ( $\leq 0.4$ ), if a dramatic size ratio must be avoided as can be seen in Figure 23. Two simulations were run (Figure 30): one where the system was initially premixed and another that was initially segregated. Both cases achieve a degree of mixing ( $IS_{w/J_{f_{MIX}}} = 0.24$  and  $IS_{w/J_{f_{SEG}}} = 0.30$ ) higher than their adhesive binary counterpart ( $IS_{wo/J_f} = 0.34$ ) over the time-scales simulated here.

### 4.3 CONCLUSIONS

In this work we propose a novel strategy to control the degree of mixing of adhesive particle systems. The systems studied are dry where adhesive forces caused by van der Waals forces predominate. By using “helper particles” of biphasic geometry, we can modify the asymptotic state of the system from mixing to segregation and *vice-versa*. We distinguish between these two functionalities denoting them as Janus-surfactants and Janus-extractants, respectively. In the case of surfactants, although the space where the aids can be used is limited, Janus particles show some promise of improving the degree of mixing in an initially segregated system and show a tendency to decrease the kinetics of segregation for systems that are

premixed and then subjected to flow. This concept could be applicable industrially when the granular material is acceptably mixed at the exit of a blending unit, and segregation occurs as the material flows in a pipe or a conveyor belt. In the case of extractants particles, the results are even more positive. When it is possible to choose aid particles that yield a two-fold difference between the highest mixing and segregation Bond numbers, we have shown a clear ability to both prevent a segregated system from mixing, as well as to induce segregation in initially mixed beds.

## 5.0 FLOW AIDS

The ubiquitous appearance of granular materials in the chemical industry implies the need of making use of their flow properties at one stage or another. Moreover, in some cases continuous processes depend on the ability of the powder to flow through different devices and inconsistent flow can lead to expensive plant shut-downs [133].

Powder flowability—or its ability to flow—depends on particle size, density, shape, chemical composition, moisture content, etc. Because of its industrial relevance and the complexity of the matter, numerous methods for measuring powder flowability have been developed. In practice, many of these methods are inconsistent and/or difficult to interpret [134]. A widely used cohesiveness measure in the pharmaceutical industry is the Hausner [135] ratio of the bed. That is the ratio of the ‘aerated bulk density’ (random loose packing) to the ‘tapped bulk density’ (random close packing). This test is done by letting the dispersed powder settle under the influence of gravity (aerated density) and then tapping the container, allowing the bed to consolidate (tapped density). Dutta *et. al* [136] relate decreases in the Hausner ratio to less cohesive materials. Another widely used methodology to assess the degree of cohesion of a granular material is the measurement of its angle of repose (AOR). The angle of repose is measured from the horizontal to the bed’s free surface and it is related to the critical stress the material can support. The most common methods of measuring the angle of repose are static/poured piles, discharges hoppers and rotated tumblers [2]. These last two examples are used in this work, to quantify the flowability of materials.

Flow aids—also known as flow conditioners, free-flowing agents, anti-caking agents, glidants, lubricants—are additives commonly used in the pharmaceutical [137, 138, 105, 139] and food [140] industry to prevent material from ‘caking’ and improve its flowability. Particulate silica, silicate, talc and salts of stearic acid have all been used for this purpose [141].

Several mechanisms have been proposed for the operation of these aids, which include [142]: reduction of inter-particle friction by coating the host particles and diminishing their surface irregularities, reduction of adhesive inter-particle forces by imposing a physical barrier, reduction of the static electrical charge on the host powder. The first mechanism usually requires a dramatic size ratio between host and conditioner powders while the second and third, both of which may be considered “adhesive screening” techniques, can work with modest size differences. In this chapter we will use our model, together with our previously developed characterization tools, to study how the physical properties of the aid particles play a significant role in their ability to increase the flowability of the powders in a manner that is most similar to the “adhesive screening methods”.

## 5.1 THEORY

Using the same strategy presented in both chapters 3 and 4, we first develop phase-space diagrams to represent our theoretical predictions and then we compare them with our PD experiments.

### 5.1.1 Granular Bond number

The Granular Bond Number defined in section 3.1.1 for binary systems is used in this chapter to design aid particles that can control the degree of flowability of an adhesive material. The host granular material is a homogeneous powder (particles 1) characterized by its granular bond number,  $Bo_{11}$ . In the presence of aid particles (particles  $a$ ), other relevant interactions arise, including: interactions that promote mixing between the conditioner and the host,  $Bo_{1a}$ , the interactions between aids,  $Bo_{aa}$ , and the interaction that represent clustering between aids and particles,  $Bo_{1a1}$ . The starting point for these expressions is in Table 3 and simplifications are made considering the aids particles are symmetric (not Janus). The relevant Bond numbers for this case are summarized in Table 6.

Table 6: Granular Bond numbers for systems containing flow aids (1 is host powder,  $a$  is conditioner powder).

Bond Number	Interactions	Expression
$Bo_{11}$	$\bigcirc\bigcirc$	$\frac{F_{vdw_{11}}}{W_1}$
$Bo_{aa}$	$\bullet\bullet$	$\frac{F_{vdw_{aa}}}{W_a}$
$Bo_{1a}$	$\bigcirc\bullet$	$\frac{F_{vdw_{1a}}}{\min(W_1, W_a)}$
$Bo_{1a1}$	$\bigcirc\bullet\bigcirc$	$\frac{F_{vdw_{1a}}}{W_1}$

### 5.1.2 Phase Diagrams

In order to identify the properties necessary to impart ‘aid’ characteristics to our helper particles, we again turn to granular bond number calculations. As with previous cases, we define  $Bo$  values for all relevant interactions in the system (assuming that the aid particles,  $a$ , can bridge interactions), thus we obtain:  $Bo_{11}, Bo_{1a1}, Bo_{aa}, Bo_{1a}$ .

The primary criteria to identify proper aid particles is that the interactions bridged by aid particles is weaker than the direct interaction between host particles, that is:

$$\mathfrak{R}_3 = \frac{Bo_{1a1}}{Bo_{11}} < 1 \quad (5.1)$$

After some manipulation, this constraint can be simplified to

$$\mathfrak{R}_3 = \frac{2\phi\beta}{1+\beta} < k_2 \quad (5.2)$$

where  $\beta = R_a/R_1$  and  $\phi = \sqrt{\Gamma_{aa}/\Gamma_{11}}$  (analogously to chapters 3 and 4, also  $\alpha = \rho_a/\rho_1$ ) and a lower the value of  $k_2$  indicates better flowability of the powder. The phase-space diagram in Figure 31 shows contour lines for different values of  $\mathfrak{R}_3$ . Our phase-space diagram indicates that, in general, smaller particles are better flow aids. Also, as the size ratio decreases, the functional values of the surface energy ratio of the aid particle becomes less restricted.

In addition to this criterion, it is also desirable that the aid particles “naturally” mix with the host particles at their asymptotic state, such that

$$\mathfrak{R}_1 = \frac{Bo_{11}}{Bo_{1a}} < 1 \quad \text{and} \quad \mathfrak{R}_2 = \frac{Bo_{aa}}{Bo_{1a}} < 1 \quad (5.3)$$

Our second criteria is *preferable*, but is not actually a *necessary* condition; i.e., it is possible that the aids may be pre-mixed into the host particles and that the operation of interest will not proceed until the system actually reach its asymptotic state (since segregation needs a finite time to take place). Therefore, we examine conditions that lead to  $\mathfrak{R}_1$  and  $\mathfrak{R}_2$  values that are a variety of values,  $k_1$ . In other words, we expect that the lower the value of  $k_1$ , the more predominant the mixing interaction  $Bo_{1a}$  is with respect to the other binary interactions in the system and a better quality of mixture is expected. This idea is depicted in the phase diagrams as regions of different shades in Figure 31 (light grey,  $k_1 = 1$ ; medium grey,  $k_1 = 0.5$ ; dark grey,  $k_1 = 0.25$ ). As the density ratio decreases (from right to left in the diagrams) size and density segregation start to compete, the ‘driving force’ for segregation diminishes and, therefore, the size of the mixing region for any given mixing quality value (value of  $k_1$ ) is larger.

## 5.2 PD SIMULATIONS

### 5.2.1 Hopper simulations

Hoppers are commonly used devices for storage, feeding of equipment, even blending of a wide variety of bulk powders—from non-cohesive, free-flowing to highly cohesive, poorly flowing. In most applications, it is relevant how the granular material will empty the hopper under the action of gravity. Roughly, two modes can be distinguished: the mass flow (where the material exits the device in a ‘first in first out’ manner) and the funnel flow (where the material that is in the center of the container will exit first).

A very simple method to measure the degree of cohesion or flowability of a material is to observe the static angle of repose of the heap in a rectangular bottomed hopper after the

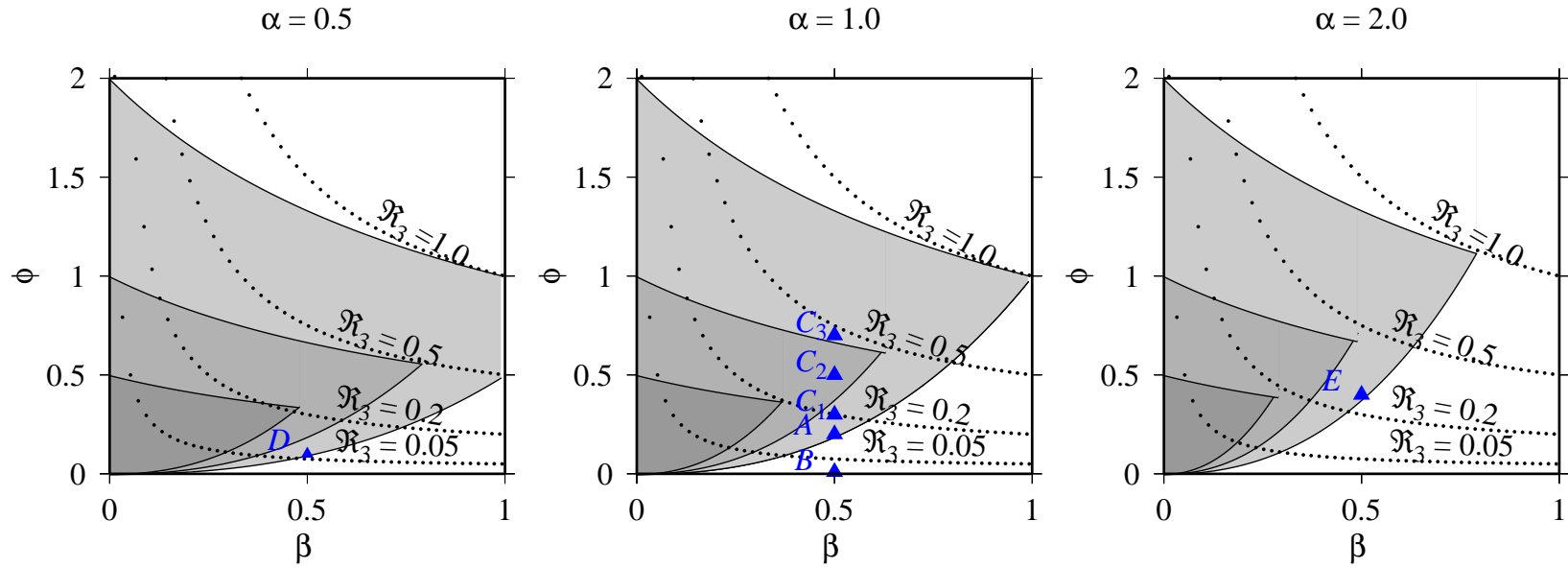


Figure 31: Flow aid phase diagram for density ratio  $\alpha$  equal to 0.5, 1.0 and 2.0, respectively. Darker shades of grey indicate regions where better mixing is expected. Contour lines showing the flowability values (lower  $\mathfrak{R}_3$ , higher ability to flow) are shown as dotted lines.

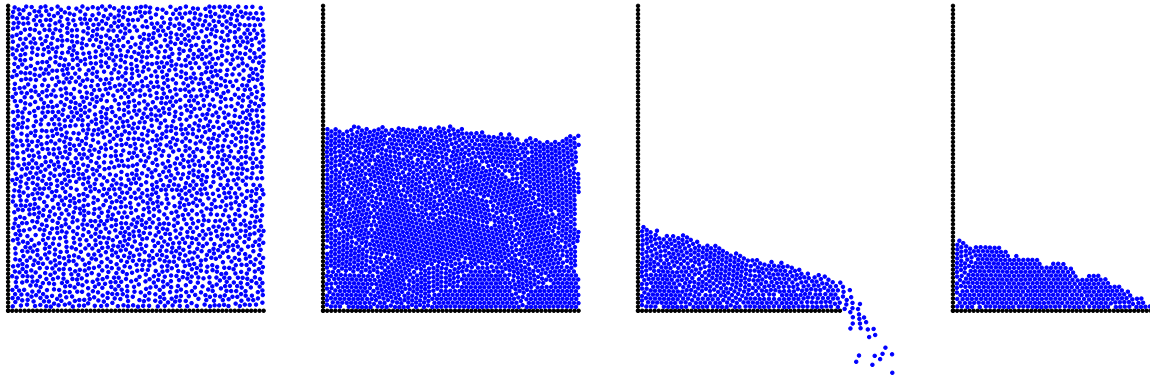


Figure 32: Hopper discharge simulation: Particles are randomly placed inside the device and let to be settled. The orifice is open and material starts to flow. The angle of repose of the remaining heap is used to assess the cohesiveness of the material.

material has been discharged. In this section, we simulate the discharge from such hoppers as shown in Figure 32 and compare the static angle of the remaining heap after the discharge. The hopper width is 50 times the particle diameter and particles are initially randomly placed in the devices, and allowed to settle. After that the hopper orifice—located in extreme right of the device and with a width equal to 10 particle diameters—is opened and the material starts to flow. The result of these experiments correspond to the angle that the remaining material forms after the flow has stopped.

The aim of this section is to show how the cohesiveness of the material can be modified by the addition of aids. In Figure 33, the angle of repose for the free-flowing, pure adhesive host powder and two cases where the the host powder has been conditioned by two different aids. The composition of aids is such that they occupy 25% of the total particle area. The properties correspond to systems B and D in Table 7. The properties of the base case material are those in Table 4. The values of  $\mathfrak{R}_3$  (0.067 and 0.007) indicate that the flowability of the combined powder is better than the pure host. Next, we take case D and increase the composition of the flow aids in terms of occupied area from 25% to 33% (Figure 34). Although we expected the angle to further decrease, the result shows that the surface becomes more irregular as we increase the aid content. This can be understood in terms of the bond number: the  $Bo_{1a1}$  (0.62) is lower than the bond number  $Bo_{11}$  (3.9), however the bond number  $Bo_{aa}$  is equal to 0.74, so that increasing the probability of an  $aa$  interaction negatively impact the surface angle relative to the 25% mix case (but it still implies an improvement over the pure host material).

### 5.2.2 Tumbler simulations

In the rolling regime, the free surface angle with the horizontal can be used as a cohesion metric. In our second simulation setup, the dynamic angle of the free surface in a rotating tumbler is used to measure the degree of cohesiveness of the host material. The systems simulated are identified in Figure 31 and their respective properties are tabulated in Tables 4 and 7. The results are presented in Figure 35 where all cases correspond to the same host powder properties. All simulations have been run for at least 2 revolutions at a rotation

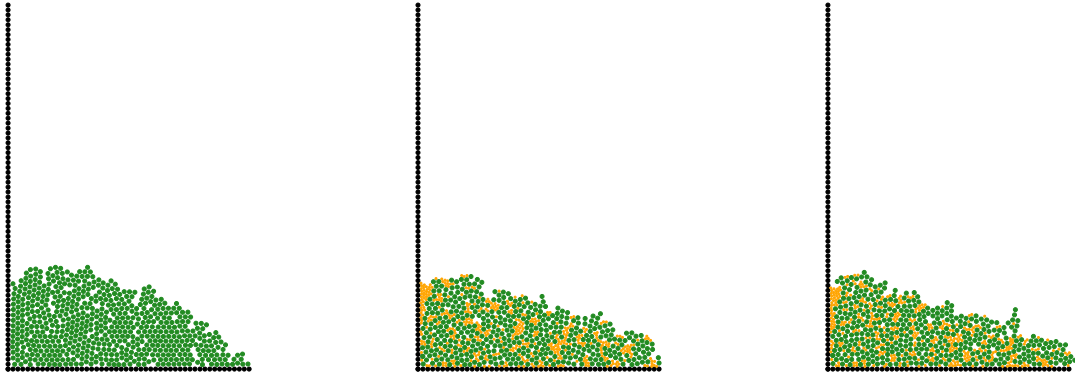


Figure 33: Heaping result for pure host powder (left, AOR =  $24^\circ$ ), with aids D (center, AOR =  $19^\circ$ ) and B (right, AOR =  $21^\circ$ ).

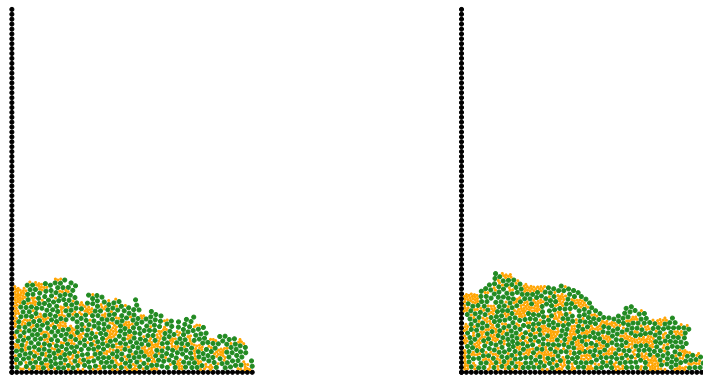


Figure 34: Heaping result for host with 25% (left) and 33% (right) aids D.

Table 7: Summary of Granular Bond number values for uniform systems (1) with flow aids (a).

	host powder	$A$	$B$	$C_1$	$C_2$	$C_3$	$D$	$E$
$\alpha$		1	1	1	1	1	0.5	2
$\beta$		0.5	0.5	0.5	0.5	0.5	0.5	0.5
$\phi$		0.2	0.01	0.3	0.5	0.7	0.1	0.4
$Bo_{11}$	9.3	9.3	9.3	9.3	9.3	9.3	9.3	9.3
$Bo_{aa}$		1.49	0.09	3.3	9.3	18.2	0.74	2.98
$Bo_{1a}$		9.9	2.49	14.9	24.8	34.8	9.9	9.9
$Bo_{1a1}$		1.24	0.31	1.86	3.11	4.34	0.62	2.48
$\mathfrak{R}_1$		0.94	3.73	0.62	0.37	0.27	0.94	0.94
$\mathfrak{R}_2$		0.15	0.03	0.22	0.37	0.52	0.07	0.30
$\mathfrak{R}_3$		0.13	0.03	0.20	0.33	0.47	0.067	0.26

rate of 5 [rpm], and in the case of flow aid conditioned material, the host powder has been ‘premixed’. That is, host and conditioner particles are randomly placed inside the tumbling device and allowed to be settled by the action of gravity. This eliminates, at least over short times, the requirement that the  $Bo_{1a}$  must be dominant relative  $Bo_{11}$  and  $Bo_{aa}$ .

The case without glidant corresponds to the tumbler on the far left. Three different aids corresponding to cases labeled as  $E$ ,  $A$  and  $D$  are shown in the top, middle and bottom rows, respectively. From left to right the area composition of aids increase from 0% (leftmost column), to 25%, to 39%, to 50%. The rightmost column shown tumbler snapshots containing only aids. The  $\mathfrak{R}_3$  values decrease from top to bottom indicating better flow properties. This is confirmed by the dynamic repose angles we measured. The system with no aids has an angle of repose of 49 degrees, which decreases to 34–35 degrees with 25% aids. As expected in every case, as the aid composition is increased the repose angle decreases and approaches that of the pure aids. In the lower row, aids  $D$  are shown to be the most efficient with a  $\mathfrak{R}_3$  of 0.067.

For all three aid types ( $E$ ,  $A$ ,  $D$ ) in Figure 35 the bond number corresponding to the interaction  $aa$  is again higher than that corresponding to the interaction  $1a1$ . This is unavoidable for systems that satisfy the mixing conditions. In the case of the hopper we observed that increasing the aid content did not further improve the powder’s flowability properties. However, this effect is not observed in rotating tumblers. This can be understood by virtue of the fact that, in the hopper case,  $aa$  was larger than  $1a1$ , so increasing the content of aid particles made the interactions  $aa$  more frequent. In contrast, the tumbler case is a “thermalized” system where particles can choose their most favorable asymptotic partner. Since  $Bo_{aa} \downarrow Bo_{1a}$  (satisfying mixing constraints), particles  $a$  will prefer to bond with host particles 1 rather than other aids, and further facilitate interactions  $1a1$ . Therefore, we can conclude that increasing the number of aid particles can be detrimental if and only if the system is not properly thermalized.

Next, we tested the material using aid particles that are expected to improve the flowability properties in different degrees according to their respective values of  $\mathfrak{R}_3$ . In Figure 36, the snapshot on the far left corresponds to aids  $A$  ( $\mathfrak{R}_3 = 1.3$ ) and three different systems have been studied ( $C_1$ ,  $C_2$  and  $C_3$  in Table 7) to explore the effect of changing the aid

properties giving different  $\mathfrak{R}_3$  values. All four snapshots were taken after the tumblers have completed exactly 2 revolutions and auxiliary lines have been drawn in each case to estimate their respective AORs. As expected, the flow properties of the material deteriorate as we use aids with higher values of  $\mathfrak{R}_3$ . However, it can be seen in our phase diagrams (Figure 31), that in this particular set the lower the value of  $\mathfrak{R}_3$ , the closer to the E (Enhanced segregation) phase our system are. This explains why system A on the far left (Figure 36) already starts exhibiting segregation after two revolutions deteriorating the performance of the flow aids in the system (irregular free surface). Our last experiment explore the importance of satisfying the mixing constraints described in equation 5.3 in the aids performance. Figure 37 shows how the AOR of a system containing aids B increases—and its flow properties deteriorate—as it becomes more and more segregated.

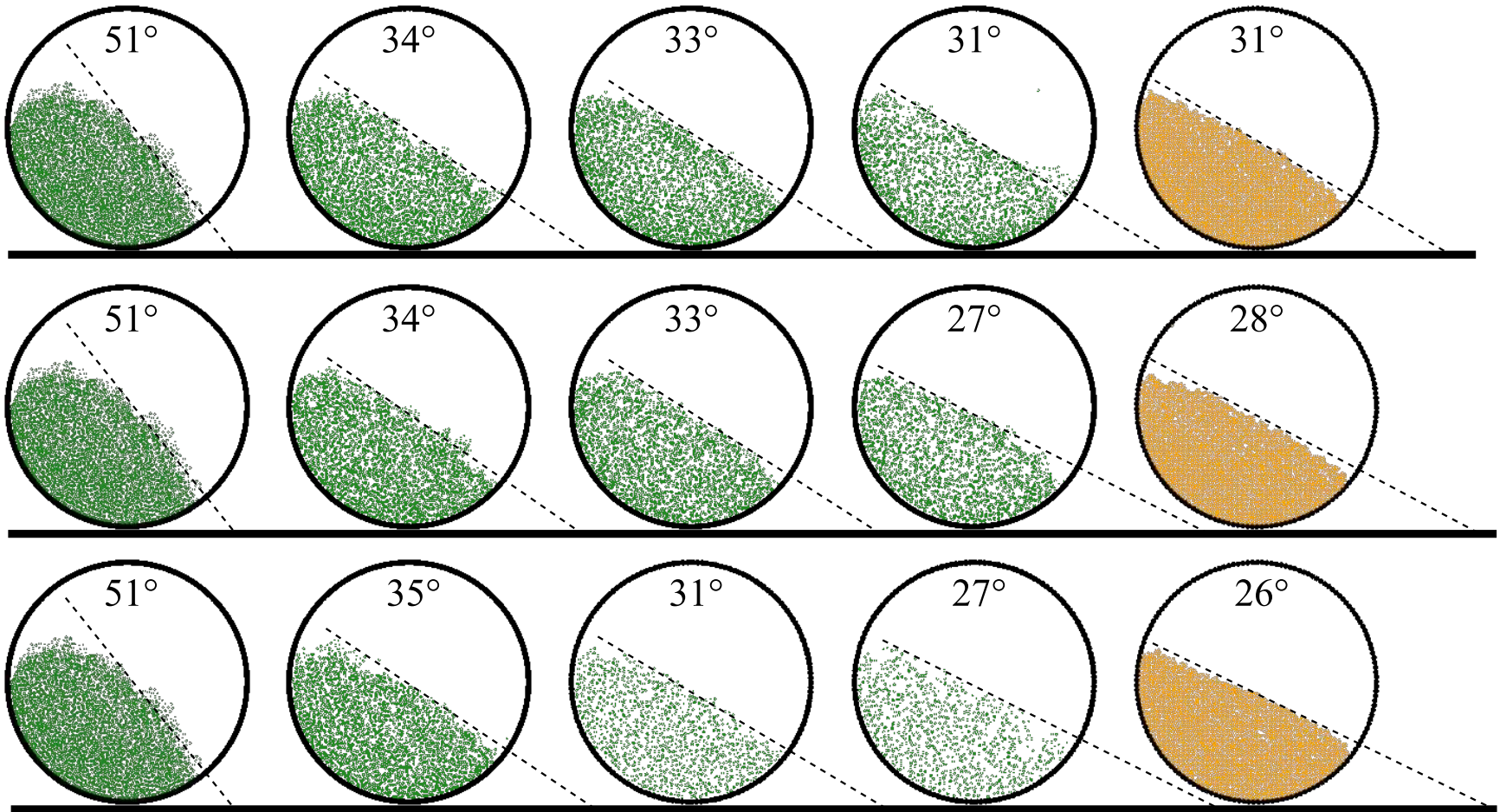


Figure 35: Dynamic angle of repose for host powder with aids  $E$  (center),  $A$  (top),  $D$  (bottom). From left to right the content of aids increases from no-aids to pure aids.

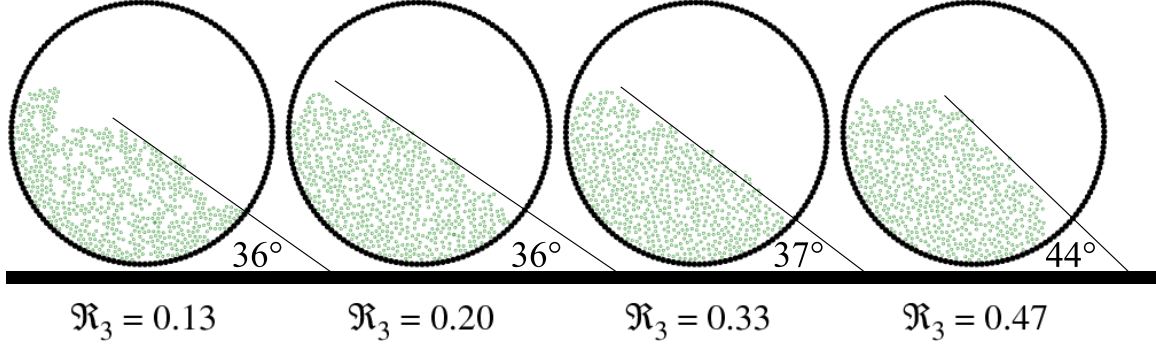


Figure 36: Dynamic angle of repose for systems containing aids  $A$ ,  $C_1$ ,  $C_2$ ,  $C_3$ . As value of  $\mathfrak{R}_3$  increases, the flow properties of the mixture deteriorate.

Note that, in our theory, we have assumed that the particular mechanism by which our aids work corresponds to the one that involves imposing a physical barrier between the host particles and thus disabling adhesive interactions between them. We have somewhat arbitrarily chosen a size ratio between aids to host particles equal to 0.5, while in industrial practice it is common to find differences of one or two order of magnitudes between the aid and host particle dimensions [141]. In our case, this is due to the computational limitations of simulating those systems. Not only does a large size difference dramatically increase the necessary number of particles, but also it severely hampers contact detection routines. However, it is important to clarify that this theory would still apply to those cases where the size ratio decreases to lower values. The limit is determined by the underlying physical mechanism we attempt to model: when the absolute value of the aid particle size is comparable to the range of action of the adhesive force involved. Forces of van der Waals are short range so that two micron-sized particles separated by any distance larger than 1/10 of the particle diameter would feel van der Waals forces that are negligible when compared to gravity forces. In this way, an aid particle that forces a distance between host particles equal to 1/10 (or greater) of the particle diameter would have the potential to efficiently screen the  $Bo_{11}$  interaction.

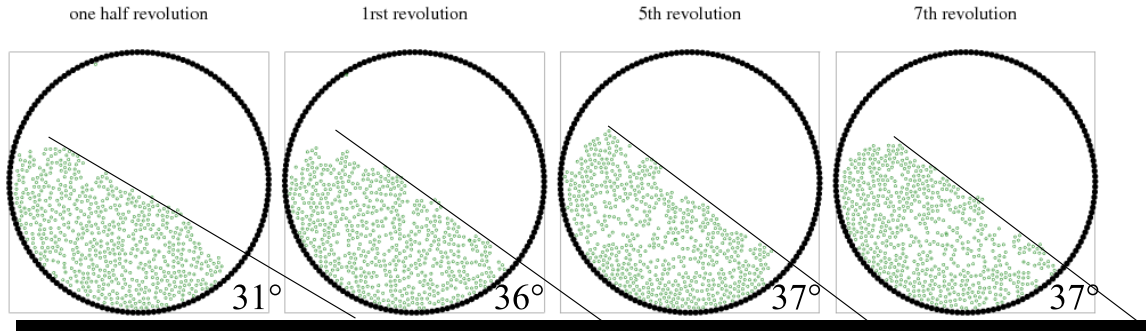


Figure 37: System with aids B: as the drum tumbles, the host and the aids particles (originally pre-mixed) start segregating, and the aid particles become inefficient.

### 5.3 CONCLUSIONS

In this Chapter, we have proposed a criteria to design glidants to increase the flowability of an adhesive granular material. Their performance can be assessed as the ratio ( $\mathfrak{R}_3$ ) of the strength of the host-aid-host ( $Bo_{1a1}$ ) particle interactions to the strength of the host-host ( $Bo_{11}$ ) interaction. In the case of a flowing material (e.g. rotating tumbler), the conditions previously developed in Chapter 3 that guarantee mixing of the material also apply. The designed aids have been shown to improve the flowability properties of the material commensurate with the predicted values of  $\mathfrak{R}_3$ . As expected, when the content of glidants is increased, the angle of repose approaches the value of the system containing purely aids.

## 6.0 MIXING AND HEATING IN GRANULAR MATERIALS

Granular materials subjected to agitation are encountered in many practical applications of material processing. Furthermore, many of these applications also involve heat transfer whereby solids come into contact with cooling or heating surfaces and heat is exchanged not only between individual particles, but also between the particles and external surfaces during the duration of the particle-particle or particle-surface contact. The magnitude of the heat exchanged during any of these events depends on the thermo-physical properties of the particles and the surfaces/walls, the interstitial fluid, the shape of the particles and the contact time [35], among other variables. The flow behavior in these heating/cooling devices not only impacts the rates of heat transfer within the bulk material, but also has a significant impact on the overall mixing rate within these devices. In this work we will distinguish between “particle-level” mixing, which is due primarily to the randomization induced by inter-particle collisions, and advective or large-scale mixing which is due to the gross motion of large groups of particles. When the shearing force is small, only minor shifting of the particles occurs so mixing rates (both particle-level and advective) are small, yet the particles experience multiple lasting contacts which lead to force networks or “stress chains” [143, 144] that contribute to good particle-particle conduction [145]. As the shearing increases, significant dilation of the structure takes place such that deformation of the bulk material occurs along localized slipping planes [146] and the structure of the stress chains has a random transient character [147]. These changes lead to good particle-level mixing, but decreased particle-particle conduction rates (as the contact strength and duration decreases). Moreover, gross motion within the particle bed is now possible so that advective (large-scale) mixing can occur in addition to the mixing occurring solely at the particle scale. Naturally, there is a balance that must be struck whereby inter-particle (and particle-surface) contacts

are sufficient to promote good conduction while at the same time agitation is high enough that thermal gradients can be enhanced via mixing. The general problem of heat transfer encountered in a rotating tumbler is a very common one in chemical engineering [148] and this prototypical case serves as our testbed in the current work. Depending on the process and material variables, heat transfer between heated surfaces and particles in motion may be dominated by contact conductance. This process constitutes one of the basic mechanisms of heat transfer in particulate systems [86, 36] and this specific issue has been addressed by many authors [149, 35, 83, 36]. Recently, researchers have turned toward the thermally-modified discrete modeling technique Thermal Particle Dynamics (TPD) [84] as a means of studying such issues as the role of particle-wall versus particle-particle heat transfer [150], the impact of baffles and/or cohesion [89], and the influence of interstitial gases [91], to name a few. In this study, we specifically examine the interplay between mixing and heat transfer in granular media composed of uniform-sized spheres undergoing slow flow in a tumbler mixer using Thermal Particle Dynamics (TPD) [84]. We vary the mixing/heating rate by using different cross-sectional shapes (circular, square and elliptical) as well as two values of rotation rate for the simulated tumblers. The changing shapes are particularly of interest as commonly used industrial mixing devices have non-circular shapes; for example, a V-blender has an elliptical cross-section with respect to its rotation axis, or in the case of double-cone blender, the cross-section is a polygon. At the same time, in these non-circular drum geometries, the periodic change of the length of the shear layer promotes chaotic advection and can dramatically improve the advective mixing rate [123] with little impact on the particle-scale mixing or contact duration.

## 6.1 MIXING RATE ANALYSIS

In the context of heat transfer, the mixing process serves to equalize the temperature within the drum and maintain as high of a thermal gradient as possible near the heated surfaces. It has been well documented [151, 152, 153, 146, 154, 155] that axial mixing in a tumbler can be well described by a simple diffusive relation. On the other hand, radial mixing, while much

faster than axial mixing, is considerably more complex—depending strongly on both drum filling and rotation rate. Moreover, segregation, when present, is much more pronounced in the radial direction than in the axial direction. In the systems treated here, heat from the hot walls to the (initially) cold granular material. It is expected, therefore, that radial mixing will have a much stronger influence on the heat transfer process than axial mixing does. Despite its complexity, radial mixing has been extensively studied [156, 123, 157, 158] and can be generalized in the following way: mixing occurs when circulation times vary as a function of radial position; diffusive mixing—which causes particles to move across streamlines—is due to collisions within the shearing, surface layer.

### 6.1.1 Measuring radial mixing

As mentioned above, the mixing rate is of critical importance in the present work. By tagging a portion of the mechanically identical particles as tracers we can use the Intensity of Segregation ( $IS$ ) [121], which is a measure of the variability of the concentration of tracers in a number of spatially disparate samples, as a means of quantifying the mixing. In all of our cases—composed of identical particles—the value of  $IS$  will asymptotically decrease to the perfectly mixed value, but by observing its evolution we can determine the mixing rate of the system. As the heat is added to the system radially, from the outside in, our particles are color-tagged according to their initial radial position: particles in the inner core—far from the heated wall—are assigned to one color, while particles in the perispherical region are tagged with another one. This allows us to study the mixing evolution specifically in the direction of highest initial thermal gradient. In all cases there is an exponential decay in the  $IS$  value that can be fitted to an equation of the form

$$IS = C_0 e^{(-2\pi k_{mix} t)}. \quad (6.1)$$

The fitted curves are shown as solid lines in Figure 39. A mixing rate constant,  $k_{mix}$ , can then be determined by fitting these curves to equation 6.1. The values are tabulated in Table 8. In general, the mixing rate increases with rotation rate and with decreasing the fill level of the drum. These observations agree well with those from the literature [159, 160, 161, 152, 153].

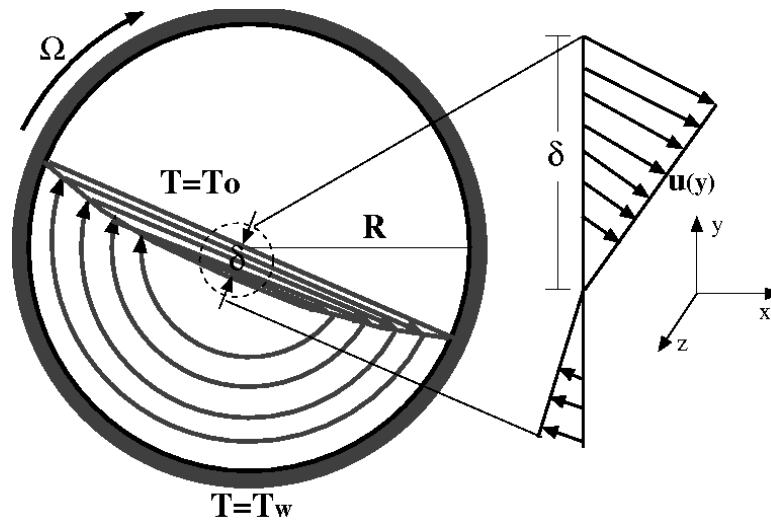


Figure 38: Schematic of a rotating cylinder with heat exchange at the wall, showing the definition of the shear layer thickness  $\delta$ . The shear layer defines the region within the bed where the main motion of the particles is taking place (heat advection region), and defines the boundary from the region of solid-body rotation (heat conduction region). Representative streamlines, the coordinate system and the relevant system parameters are also shown.

Table 8: Computational rates of mixing,  $k_{mix}[s^{-1}]$

Rotation speed	Tumbler filling level		
	$\Omega$ [rpm]	$f = 0.50$	$f = 0.37$
5	$1.1 \times 10^{-3}$	0.029	0.073
10	$1.3 \times 10^{-3}$	0.050	0.15
15	$1.4 \times 10^{-3}$	0.060	0.18

High rates of heat transfer and high heat transfer coefficients are expected under conditions in which there is a rapid exchange between particles in the bulk and those close to the wall, (*i.e.*, higher rates of mixing). As expected, Figure 40a shows, for a half filled tumbler, that increasing the rotation rate (thus, increasing the mixing rate; see Table 8) increases the rate of heat transfer. However, for a filling level of 0.25—where the mixing rates are about 100 times higher than for a half-filled tumbler—the opposite trend is observed with respect to rotation rate (See Figure 40c). In these cases, the higher mixing rates resulting from the increased rotation rate seem to lead to a slower heating of the particles inside the tumbler. Therefore, although rapid mixing rates typically favor faster heating rates, it is clear that this is not the only factor determining the rate with which granular material will heat. This observation was the primary impetus for the current work.

### 6.1.2 Analyzing heating mechanisms

As is true in fluids, heat can be transferred in granular materials by different mechanisms—conduction, convection and radiation. Since the temperatures concerned in this study are assumed to be relatively low, radiant heat transfer is neglected. Moreover, as the purpose of this study is to examine the impact of mixing on the relative importance of conduction and convection, the interstitial fluid is neglected (simulations are performed under vacuum conditions). Heat conduction occurs whenever two or more particles are in contact and the amount of energy transferred by this mechanism depends not only on the temperature

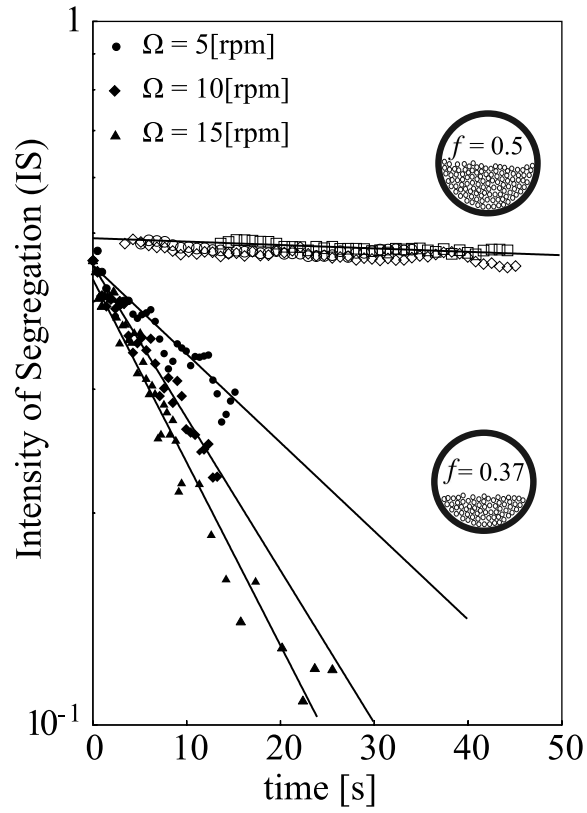


Figure 39: Variation of the Intensity of Segregation with different rotation rates at constant filling degree  $f = 0.37$  and  $f = 0.5$ . For a half filled tumbler  $f = 0.5$ , the circulation time of the material in the bed is independent of radial position thus mixing takes place at a very low rate. In contrast, for less than half filled drums ( $f \rightarrow 0$ ), the circulation time varies with radial position and therefore mixing is more rapid [160].

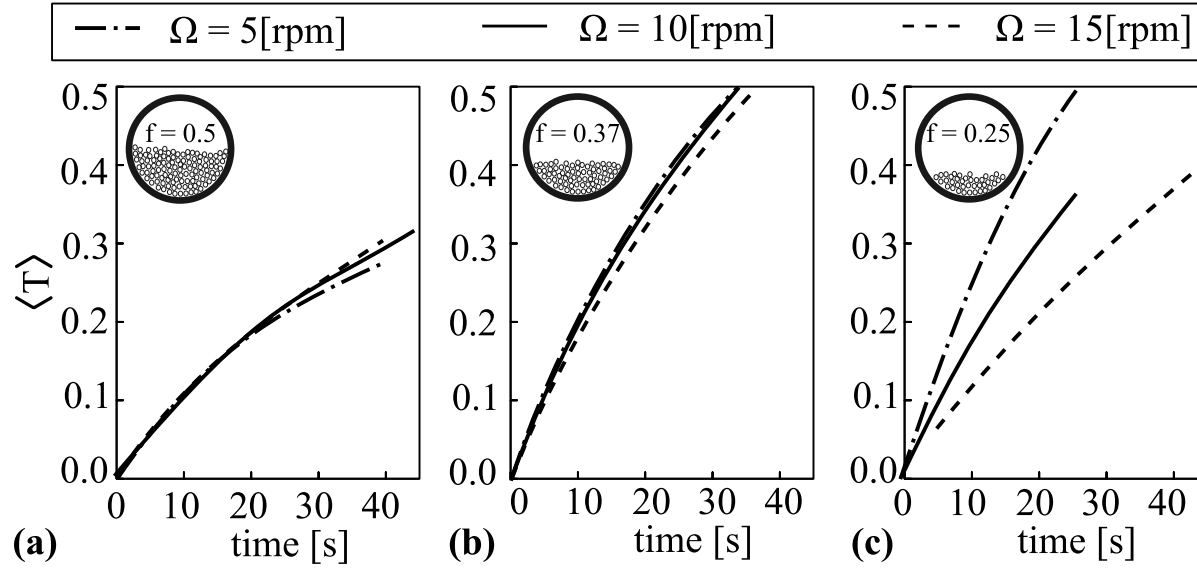


Figure 40: Variation of the bulk temperature in a rotating tumbler at three different extents of filling. The bulk temperature within the drum varies in a logarithmic fashion, although the local temperature evolution of individual particles is highly nonlinear. The rate of change is dependent on both the filling level ( $f$ ) and the rotation rate ( $\Omega$ ).

difference but also on the size of the contact area and the duration of the contact. In consequence, the mechanical properties of the particle (such as the shear modulus or the Young’s modulus) will impact the rate of conductive/diffusive transfer of heat through the particles. On the other hand, convection of heat corresponds to the transfer of energy associated with the movement of particles relative to one another, where particles from hotter regions are physically moved to colder zones, and *vice versa*. In this work, we use the Péclet number to determine the heat transfer mechanism that is expected to be dominant in the overall bed heating. The Péclet number for granular systems is calculated as follows:

$$Pe = \frac{\{\text{mixing rate}\}}{\{\text{rate of thermal diffusion}\}} = \frac{\frac{1}{t_{mix}}}{\frac{\alpha_T}{\lambda^2}} \quad (6.2)$$

where  $t_{mix}$  will be obtained from the slope of a log-lin  $IS$  plot,  $\alpha_T$  is the effective thermal diffusivity of the particle bed, and  $\lambda$  is the characteristic length of the system. For our rotating tumblers of different cross-sectional shapes, we have used the equivalent diameter of the drum  $\lambda$ . Using this definition, a system characterized by a low Péclet number is one where heat is predominantly transferred within the bed by inter-particle conduction, and a high Péclet number indicates that convection, or the motion of hot particles, is the predominant mechanism. It should be noted that, unlike the case of a fluid system, in a granular system the rate of heat diffusion through the “material” itself is not independent of the mixing rate as it is defined in equation 6.2 because of the change in the effective thermal conductivity with the changing bed microstructure.

### 6.1.3 Apparent heat transfer coefficient

In order to quantify the impact of mixing on the overall rate of heat transfer within tumbler-type devices, we use an apparent heat transfer coefficient,  $h_T$ . This value is related to the difference between the wall temperature and the average temperature in the granular phase, thus it incorporates not only the transfer of the heat from the wall to the particle bed, but also the transfer between the particles within the bed itself. Using this simple definition of  $h_T$  and performing an overall balance of heat in the granular bed, we can derive an equation for  $h_T$  as:

$$\rho V_B c \frac{d\langle T \rangle}{dt} = h_T A_T (T_W - \langle T \rangle) \quad (6.3)$$

where  $V_B$  is the volume of the granular bed,  $A_T$  is the area in contact with the tumbler walls,  $\langle T \rangle$  is the mean temperature in the granular bed, and  $T_W$  is the wall temperature. We then obtain the apparent heat transfer coefficient ( $h_T$ ) from the slope of the heating curve (i.e., plots of  $\ln\left(\frac{T_W - T_0}{T_W - \langle T \rangle}\right)$  versus time; see Figure 41). It should be noted that, in previous work [150, 162], the apparent heat transfer coefficient defined in Eqn. 6.3 was shown to vary with time (making it less useful of a discriminatory tool for our purposes). In order to examine this tendency in the current mixing study we simulated several two-dimensional systems composed of soft particles ( $E^* = 30[MPa]$ ,  $\rho = 1000[Kg/m^3]$ ,  $c = 385[J/KgK]$ ,  $\nu = 0.33$ ,  $d_p = 4[mm]$ ) and observed how rapidly  $h_T$  reached a constant value as the heating process evolves. Low ( $k = 1.0[W/mK]$ ) and high ( $k = 1000.0[W/mK]$ ) thermal conductivity systems are examined with tumblers whose diameter is 40 times the particle diameter. To cover the range of parameter space to be studied in this work, we vary the relative value of the conductance in equation 2.33 for wall—particle contacts with respect to those values for the particle-particle contacts. In our base case, as well as in all other cases present in the following sections, the tumbler walls are composed of particles of the same material as the particles inside the drum, so the resistance is comparable for both kind of contacts ( $H_{c_{WP}}/H_{c_{PP}} = 1$ ). By making the resistance at the wall significantly higher ( $H_{c_{WP}}/H_{c_{PP}} = 0.01$ ), the flow of energy to the granular bed from the walls is expected to become the bottleneck. The opposite case is also presented, where the resistance between the particles in the bed is dominant ( $H_{c_{WP}}/H_{c_{PP}} = 100$ ). All three situations are studied at both high and low Péclet number values by changing the base value of  $H_{c_{PP}}$  to correspond to the high and low conductivity materials, respectively (recalling that  $H_{c_{ij}} = 2k_s a_{ij}$  for particle–particle transport, see Table 9). In almost all cases examined,  $h_T$  rapidly reaches a constant value as indicated by the slopes of the heating curves shown in Figure 41. The  $h_T$  values and the correlation coefficients for the linear regressions in Figure 41 are shown in Table 9. The only  $h_T$  value that exhibits a significant dependence on time is that of the low value of Péclet with high wall resistance. Even then, a relatively constant value is expected after approximately the first revolution (10 seconds). Interestingly, the apparent  $h_T$  values obtained for cases  $H_{c_{WP}}/H_{c_{PP}} = 0.01$  and  $H_{c_{WP}}/H_{c_{PP}} = 1.0$  are almost exactly proportional to the prescribed  $H_{c_{WP}}/H_{c_{PP}}$  in the case of high Péclet value, but show no such dependence

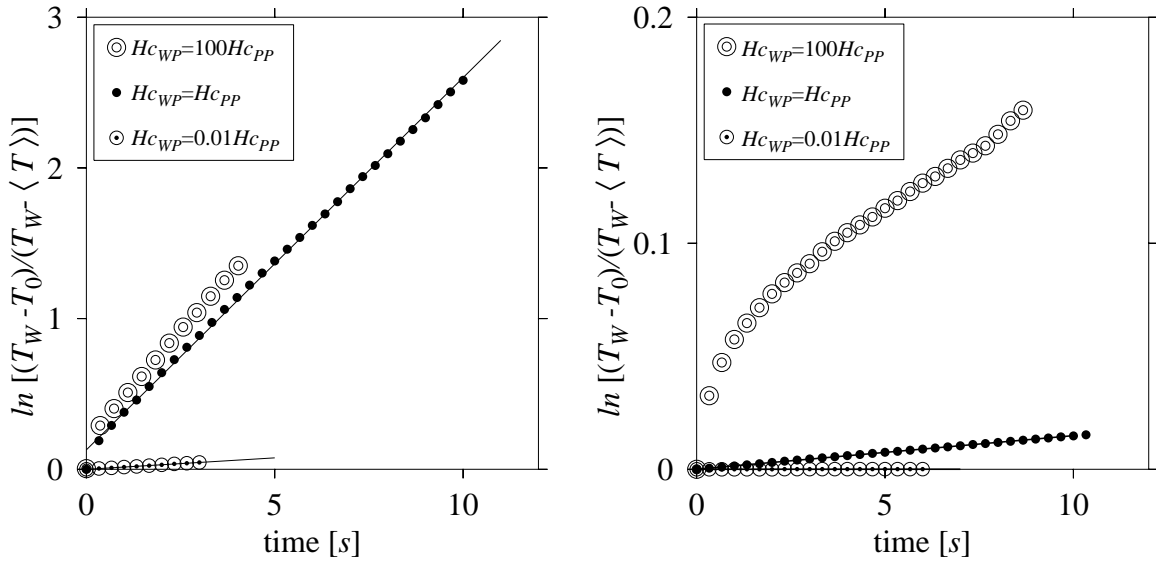


Figure 41: Logarithmic heating curves for systems with low (left) and high (right) values of Péclet. This figure shows cases where the conductance between the bed particles and the wall is negligible ( $H_{c_{WP}}/H_{c_{PP}} = 0.01$ ), comparable to ( $H_{c_{WP}}/H_{c_{PP}} = 1$ ) and larger than ( $H_{c_{WP}}/H_{c_{PP}} = 100$ ) the conductance between in-bed particles.

Table 9: Regression values for correlations of curves in Figure 41.

<b>Pe = 0.0356</b>			<b>Pe = 35.6</b>		
$\frac{H_{cWP}}{H_{cPP}}$	$h_T, [W/m^2K]$	$R^2$	$\frac{H_{cWP}}{H_{cPP}}$	$h_T, [W/m^2K]$	$R^2$
0.01	240	0.99	0.01	0.25	0.99
1	3900	0.99	1	23	0.99

in the case of low Péclet number. This suggests that the apparent value of  $h_T$  can, in fact, be used as a discriminator for the relative importance of the mixing rate. Moreover, as we will allow the transport rate between the wall and the bed to be determined “naturally” from the contacts between wall-based and moving particles (i.e.,  $H_{cWP}/H_{cPP} = 1$ ), we expect that time variation of  $h_T$  will not significantly impact our results.

#### 6.1.4 Heating and mixing rate

In order to analyze the relationship between mixing and heating, several simulations were run for two different materials: glass and aluminum. Glass and aluminum have been chosen as the pure materials because they exhibit thermal diffusivity values differing by almost a factor of 100 ( $\alpha_{TAl} = 7.4 \times 10^{-5} m^2/s$  and  $\alpha_{TGlass} = 7.9 \times 10^{-7} m^2/s$ ). The differences in mechanical properties, however, are not as dramatic, so mixing rates for both systems are expected to be comparable. The tumbler rotation speed is varied, as is the tumbler cross-sectional shape, leading to a range of mixing rates. For each case, the apparent heat transfer coefficient and the mixing rate are calculated as described in the previous sections. Schlünder [162] studied the transfer of heat in a stirred particle system by assuming that the process occurs in two steps: first, the heat needs to be captured from the hot walls to the granular phase; second, the heat needs to be re-dispersed within the whole bed. He noted that each of these steps have to overcome different heat transfer resistances and either of them could become the process bottleneck. Each of those resistances were then estimated from a continuous penetration model introducing one empirical parameter to describe the

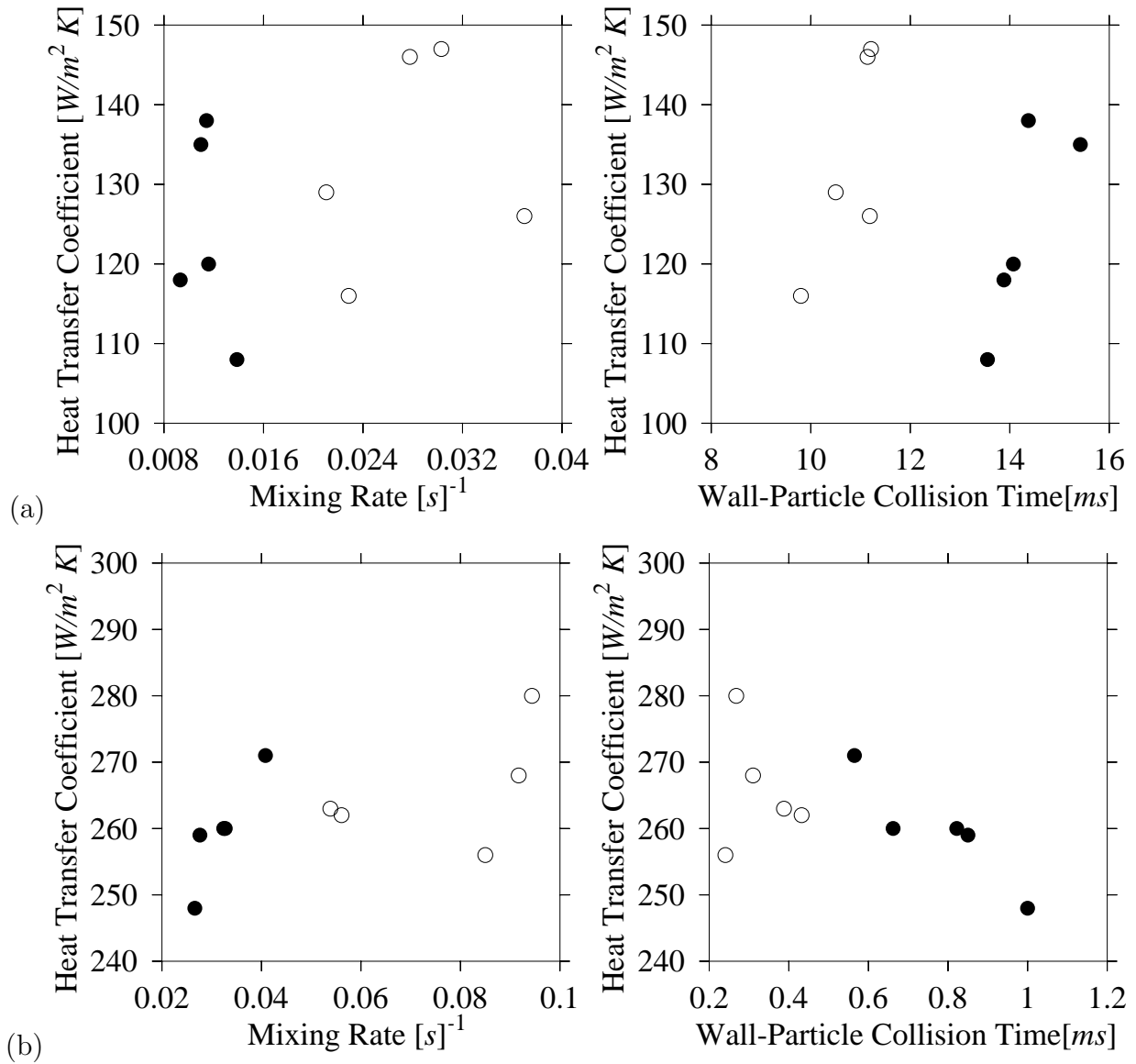


Figure 42: Apparent heat transfer coefficient for (a) glass and (b) aluminum particle simulations as a function of the mixing rate (left) and the wall-particle collision time (right). Two different tumbler rotation rates are shown: 5 [rpm] ( $\circ$ ) and 18 [rpm] ( $\bullet$ ), as are several tumbler geometries (see symbol shape; noting that the ellipse with a vertical line has an axis ratio of 0.7, with a horizontal line has a ratio of 0.5, and no line corresponds to a ratio of 0.6).

particle motion—the mixing number. The work of Kwapinska *et al.* aimed to bridge a discrete modeling approach to this continuous model where the local resistances were chosen to mimic an effective equivalent thermal conductivity of the granular bed. In order to understand the results of the previous section (See Figure 40) it is useful to note that, while increased mixing rates clearly impact this second step, they also have a non-negligible impact on the particle-wall contact duration and perhaps even the size of the particle-wall contact area. As evidence of this explanation first, we attempt to directly correlate the mixing and heating rates for the glass particle simulations. Figure 42a (left) shows that no clear relation can be drawn between the heat transfer coefficient and the mixing rate of each system studied. This suggests that the second step is not the rate limiting step. In contrast, Figure 42a (right), shows the relationship between the apparent heat transfer coefficient and wall-particle collision time and we find that for a fixed rotation rate, the longer the wall-particle collisions, the higher the heating rate.

In contrast to glass, where particle collisions need to be relatively long to allow heat to flow between the particles, a highly conductive material (like aluminum) can effectively transmit heat during a collision of significantly shorter time. Figure 42b shows the relationship between the heat transfer coefficient and the mixing rates and it can be seen that in this set of simulations increasing the rate of mixing leads to faster heating. Meanwhile, the relationship with the collision time is not clear. This suggests that the redistribution of heated particles is the rate limiting step in the aluminum cases studied.

### 6.1.5 A scaling attempt

Next, in this work, we attempt to draw a correlation between the calculated Péclet number and the rate of transfer of heat. In fluid systems, it is common to relate the rate of heat transfer using the Nusselt number and correlations of the general form

$$Nu = \xi_0 Pe_1^{\xi_1} \tag{6.4}$$

can often be found (with varying values of  $\xi_0$  and  $\xi_1$ ). While rates of thermal diffusion needed to estimate the Péclet number are expected to be proportional to the thermal diffusivity of

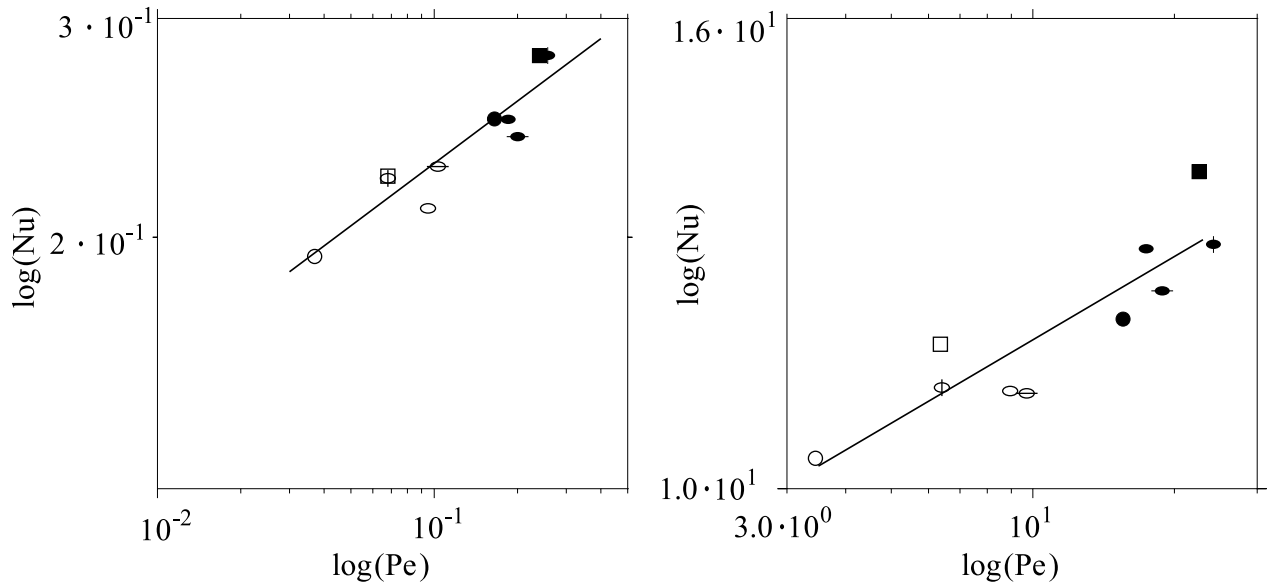


Figure 43: Nusselt vs. Péclet number for aluminum (left) and glass (right) particle systems for a tumbler rotation rate of 5 and 18 [rpm] and several tumbler geometries (see symbol shape).

Table 10: Apparent heat transfer coefficient,  $h_T$  in  $[W/m^2K]$ , and Péclet numbers for both glass and aluminum particle simulations at 5 and 18 [rpm].

Tumbler Shape	Glass Simulations				Aluminum Simulations			
	5 [rpm]		18 [rpm]		5 [rpm]		18 [rpm]	
	$h_T$	$Pe$	$h_T$	$Pe$	$h_T$	$Pe$	$h_T$	$Pe$
circle	116	3	135	16	230	0.037	295	0.17
square	118	6	142	23	238	0.068	297	0.24
ellipse $\bar{B} = 0.5$	110	10	123	18	239	0.103	253	0.20
ellipse $\bar{B} = 0.6$	112	9	130	17	225	0.095	264	0.18
ellipse $\bar{B} = 0.7$	113	6	133	24	240	0.068	302	0.26

the material used, when calculating these dimensionless numbers for heterogeneous systems, the main difficulty resides in estimating the effective properties of the granular bed. Here, the density and specific heat have been calculated as  $\rho = \rho_S(1 - \varepsilon)$  and  $c \sim c_S$ , where  $\rho_S$  and  $c_S$  are the pure material density and specific heat, respectively. Analogously, the conductivity is estimated by  $k = k_S(1 - \varepsilon)$ . Not surprisingly, despite the system heterogeneity, the Péclet numbers for the glass particle simulations ( $Pe > 1$ ) are found to be significantly higher than those for aluminum ( $< 0.5$ ) (See Table 10).

In Figure 43, the measured  $Nu$  numbers are plotted versus  $Pe$  for the variety of systems studied thus far. From the analysis presented here, no universal dependency encloses the whole data set; however, for each data set the Nusselt number is linearly dependent on the Péclet when the data is presented in a log-log plot (where the slope corresponds to  $b$  in equation 6.4). A more accurate estimation of the effective properties of the agitated granular materials—that considers the effect of their microstructure—could reconcile the results for different materials.

Table 11: TPD simulation parameters and mixing rates.

Tumbler Shape	Mixing Rates, [ $s^{-1}$ ]		No. of Particles		Tumbler Dimensions	
	5 [rpm]	18 [rpm]	wall	total	length [ $d_p$ ]	
circle	$2.7 \times 10^{-4}$	$1.2 \times 10^{-3}$	704	8940	diameter	50
square	$4.0 \times 10^{-4}$	$1.4 \times 10^{-3}$	1000	10455	side	50
ellipse $\bar{B} = 0.5$	$6.0 \times 10^{-4}$	$1.2 \times 10^{-3}$	1008	9540	major axis	80
ellipse $\bar{B} = 0.6$	$5.7 \times 10^{-4}$	$1.1 \times 10^{-3}$	908	9200	major axis	72
ellipse $\bar{B} = 0.7$	$4.1 \times 10^{-4}$	$1.7 \times 10^{-3}$	832	9020	major axis	66

## 6.2 MIXING TOPOLOGY AND HEAT TRANSFER

Similar to their continuum fluid counterparts, non-cohesive granular materials under flow can display chaotic advection [156, 7, 123, 158]. The nature of these patterns depends on a host of factors, including among others the filling level and geometry of the boundaries. When chaotic advection takes place inside a rotating vessel, the mixing rate can be dramatically enhanced with little or no impact on the particle-level mixing rate. The impact of this type of flow on heat transfer in granular materials has not been explored.

In all of the systems studied, it is expected that the mixing patterns/topology interacts in a nontrivial way with the heat transfer process. When the granular material is heated from the tumbler walls, no heat is expected to be transferred into the islands by an advective flow and increases in temperature of the particles in these regions are the result of a thermal diffusive flux only. Therefore, in systems where the  $Pe$  is large such that the conductive flow of heat is the limiting step in the heat transfer process, the presence of these islands in the mixing topology should be more pronounced in the temperature profiles/contours as the convective transport rapidly distributes heat in the chaotic regions (i.e., outside these islands). Snapshots of the per-particle temperature profile—for a mean non-wall particle

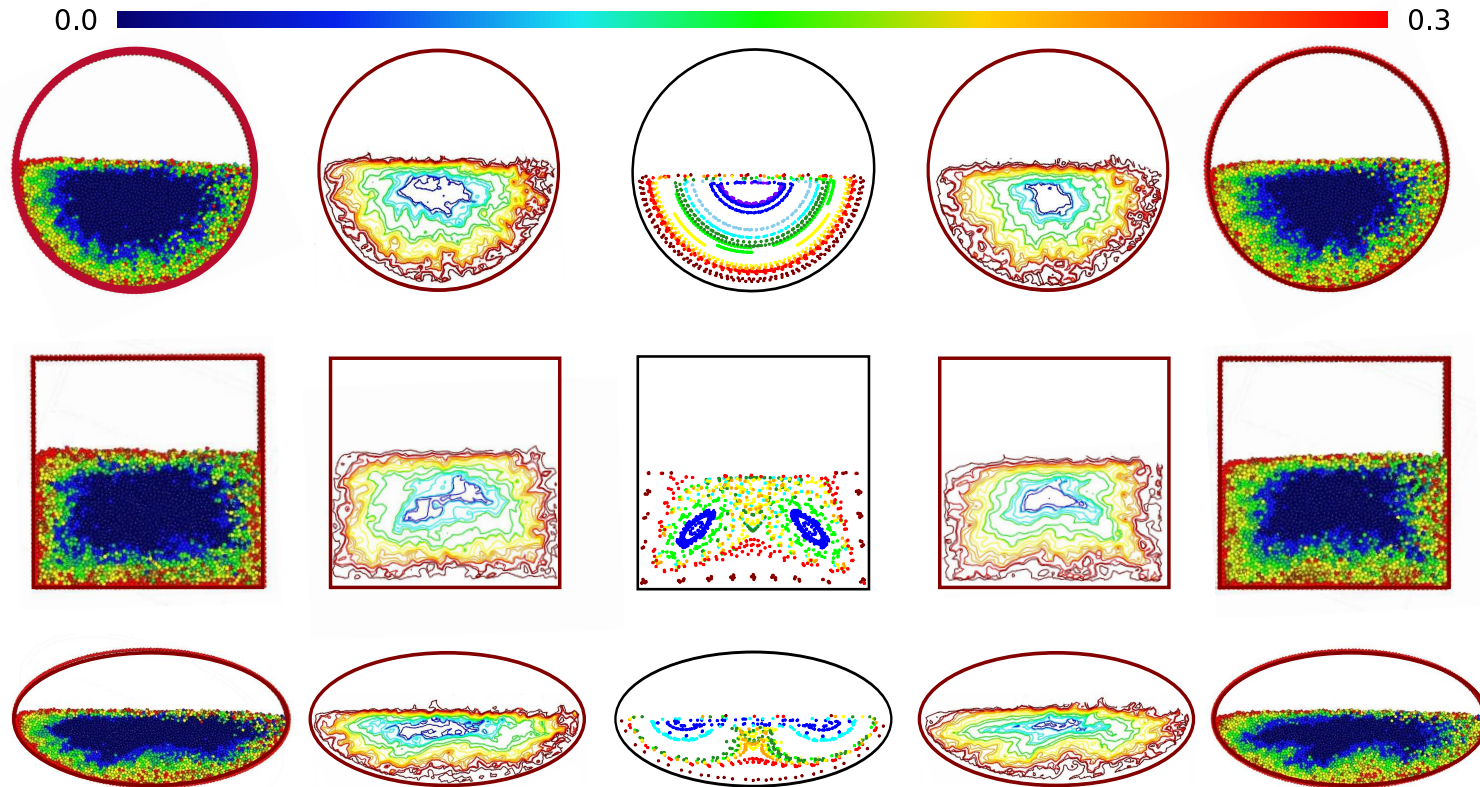


Figure 44: Mixing and heat conduction in drums with different cross section. Poincaré sections from continuum model (center column). Computational heat transfer snapshots and contour plots using TPD for glass particles (right columns) and aluminum particles (left columns). Note that the colors in all thermal plots denote varying dimensionless particle temperature (see top scale).

dimensionless temperature equal to 0.1—are also shown in Figure 44 for three tumbler geometries and two materials—aluminum (left) and glass (right)—as well as the corresponding depth-averaged temperature contour plots. Differences in the glass and aluminum cases can be observed even for the simplest case, a circular cross-sectional tumbler. Flow lines are symmetrical with respect to the tumbler rotation center and the glass system follows this pattern more closely, exhibiting a temperature profile that is almost perfectly symmetric. In contrast, in the aluminum-filled tumbler, several hot spots can be observed in the right half of the perispherical region of the aluminum tumbler, however, in the left half the temperature profile is more uniform. This is because the aluminum particles yield a low  $Pe$  so that any redistribution of heat from the particle-level mixing (during a single layer pass) is quickly diffused to neighboring particles during the course of a half-revolution (i.e., as the particle rotate from right to left). At the same time, a larger cold core of particles can be seen in the aluminum snapshot to compensate for the hot spots while achieving the same mean non-wall particle temperature. In the square cross-sectional tumbler, two eye-shaped cold cores are expected in the temperature profile based on observation of the Poincaré sections. As expected, the shape of these regions is better defined in the temperature plots of the glass system when compared to the aluminum case, with a characteristic “hill” in the center of the wall span being evident. Similarly, in the elliptical tumbler there is a difference between the systems. While in the glass simulations the two cold cores—*islands*—are clearly delimited and separated by a slightly higher temperature zone, in the aluminum simulation the islands are not easily identified from each other and the temperature seems to be almost rotationally symmetric. As further quantitative evidence of the impact of mixing topology, Figure 45 highlights the presence or lack of rotational symmetry by showing the average particle temperature along a radial arm projecting from the tumbler center at three different angles with respect to the free surface. These angles have been chosen to determine planes that intersect different structures in the respective—circular, square or elliptical—Poincaré sections. The mean temperature is obtained by averaging the temperature of all particles within a distance of one particle diameter from the planes, and it is plotted against the radial distance scaled by the particle diameter. As in the previous figure, both the glass and aluminum results are shown at a time that corresponds to when the mean dimensionless temperature in the

granular bed is approximately 0.1 and the surface of the material is parallel to one of the axes of the cross section shape. In the case of a circular tumbler, all three radial profiles ( $a$ ,  $b$  and  $c$ ) pass first through the warm shear layer and next across one central cold structure. After this cold core, the temperature increases as the planes approach the hot wall. Due to the rotational symmetry of the circular mixer’s Poincaré section, all three planes yield roughly the same result for both glass and aluminum (see Figure 45 (left)). Next, in the square tumbler, the Poincaré section suggests that the three temperature profiles must differ: profiles  $a$  and  $c$  each diagonally cross one of the two big cold cores, while profile  $b$  passes across the well-mixed region. This is confirmed by 45 (center) where curves  $a$  and  $c$  coincide in the size and location of these cold cores and profile  $b$  indicates the presence of a reduced low temperature region. Finally, the elliptical case presents this same kind of asymmetry: two of the profiles intersect the unmixed regions—and, therefore, diminished heat transferred by convection of particles—while the third one passes only a very minor region of cold particles due to the higher rate of mixing along that plane. As expected, the profiles  $a$  and  $c$  are quite similar and show a much larger cold core than profile  $b$ .

### 6.3 CONCLUSIONS

We have shown that, depending on the limiting step in the transfer of heat through the media, increasing mixing rates may be detrimental to the heating of the granular bed, rather than enhance it. This is because higher mixing rates often imply shorter collision times, which negatively impacts the transport of heat from the walls to low-conductivity particles. Making an analogy to fluid transport, we propose a Péclet number to distinguish between these cases. Higher values of the Péclet number are associated with already fast-mixing beds, where the heat conduction between particles in contact is governing the rate of heating. In these cases, decreasing the mixing rate—by operating at a lower tumbler rotation rate, for example—could provide longer particle contacts and, therefore, faster heating. In the opposite case, for lower Péclet numbers, the conduction times are short enough not to be affected by the diminishing collision times associated with higher mixing rates, and enhanced

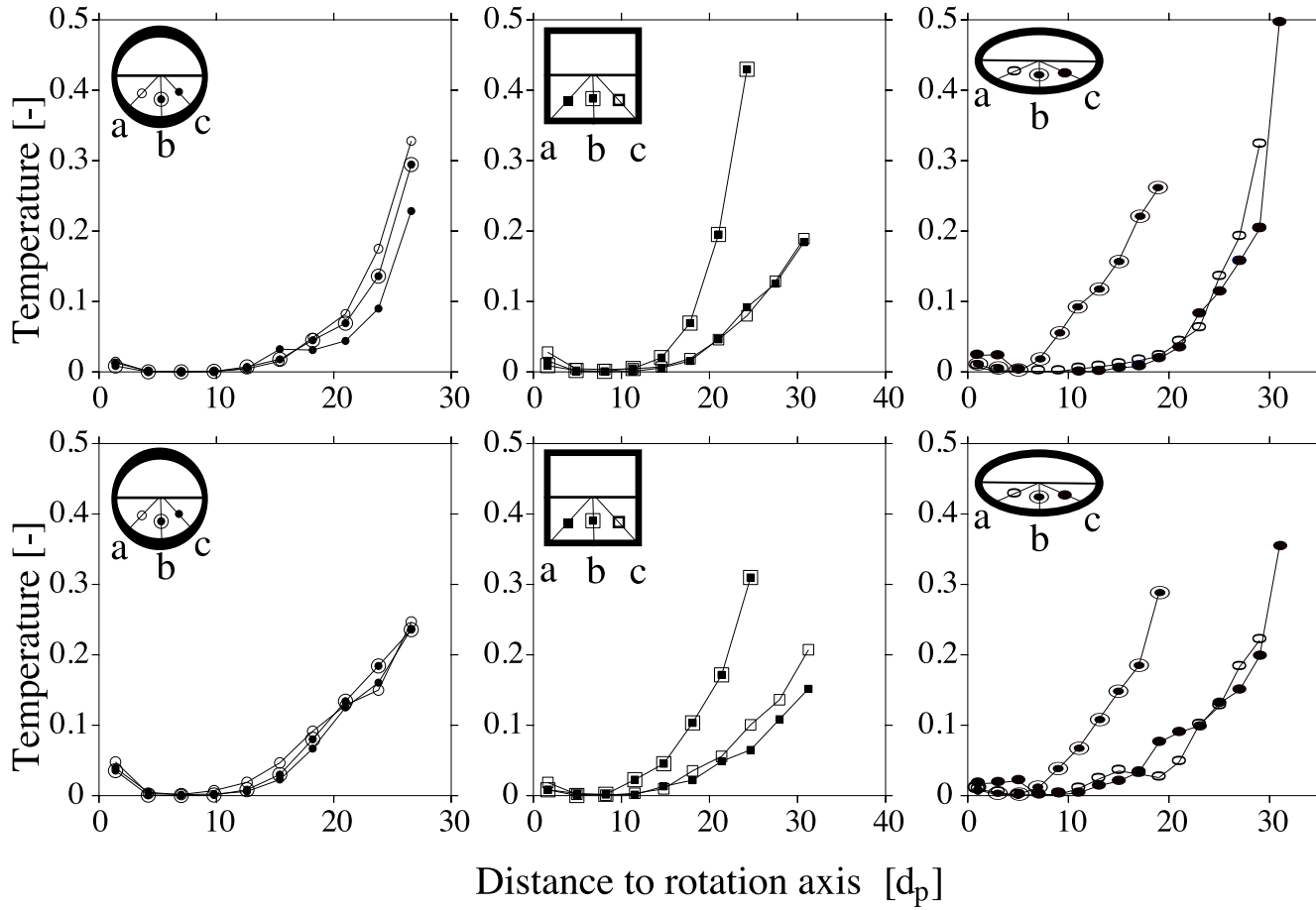


Figure 45: Temperature profile along three different tumbler radial planes for aluminum (top) and glass (bottom) particle simulations. The combination symbol (open and filled) denotes a plane perpendicular to the free surface (i.e., vertical); while the open and filled symbols, respectively, denote planes  $\pm 45^\circ$  (circle and square) or  $\pm 60^\circ$  (ellipse) with respect to the free surface.

mixing (via higher rotation rate) actually leads to more rapid transfer of heat to the bed. These conclusions seem independent of particle type, mixer geometry, and mixer rotation rate. As a potential method of avoiding this “mixing pitfall”, we also studied the mixing and thermal topologies obtained in chaotic/non-chaotic tumblers. The results of our TPD simulations for different tumbler cross-sectional shapes reveal a close relationship between patterns observed in the Poincaré section of the flow generated by a continuum model and the observed temperature field. Regions of cold particles are present inside the unmixed regions observed in the the Poincaré sections, and this tendency is more pronounced for high Péclet number systems. This suggests that higher mixing rates, even in high  $Pe$  tumblers, may be possible without the subsequent thermal penalty provided they are achieved via advection rather than increasing solely particle-level mixing (through higher rotation rates).

## 7.0 SUMMARY AND OUTLOOK

Granular materials are ubiquitous in the chemical industry. Because of their heterogeneous nature no universal set of equation can describe them. Furthermore, the intuition we have built from our knowledge of continuous media frequently misleads us when we try to predict their behavior. Nevertheless, while a direct application of fluid system approaches are often unsuccessful, much can be learned through analogies between these disparate systems. In this dissertation, we studied the behavior of granular materials and compared them with that of fluids with the aim of exploiting analogies to established fluid-fluid processing techniques/theory whenever possible. In Chapters 3 and 4 we focused on predicting and controlling mixing/segregation of dry adhesive granular materials. Chapter 5 explored how to control the flowability of granular materials. In Chapter 6, we studied the effects of heating mechanisms on the overall heat transfer rate in a granular bed.

Most of the work presented in this dissertation was carried out using a DEM simulation technique: Particle Dynamics (PD). PD is based on following each particle's position, velocities, angular velocities, orientation and temperature and updating them each time step according to (particle-particle or wall-particle) interactions. The essence of PD is dependent on the nature and accuracy of these interactions. Our PD is capable of computing dry-adhesive forces (JKR theory), following non-symmetric particle orientation (quaternions) and modeling exchange of heat.

In this Chapter, we summarize our contributions in each of the topics approached in this dissertation and outline possible directions for future work in these areas—mixing & segregation, heat transfer and flowability of powders.

## 7.1 MIXING & SEGREGATION

Many of the industries that handle granular material rely on the preparation of good mixtures along their production lines. Segregation can cause product rejection, quality/effectiveness loss, operational problems, etc. In Chapter 3, we have focussed on granular materials where dry adhesive forces are predominant such as fine powders commonly used in the pharmaceutical industry. We developed a characterization tool, the Granular Bond Number ( $Bo_{ij}$ ) to predict the relative strength of inter-particle interactions. This tool is used to build phase-space diagrams where regions of mixing/segregation—miscible/immiscible—regions are present as a function of the physical properties of the system. The mixing/segregation criteria is based on comparing the relative magnitudes of the  $Bo_{ij}$ s in the system (e.g. for binary case:  $Bo_{11}$ ,  $Bo_{22}$ ,  $Bo_{12}$ ) and arguing that whenever the interaction between dissimilar particles is the predominant interaction, the system will mix. When the dominant interaction is one between particles of the same kind ( $Bo_{11}$  or  $Bo_{22}$ ), the result will be a segregated asymptotic state. We tested our predictions by simulating a variety of powder mixture conditions and observing their tendencies to mix/segregate in tumblers. Our results show that the asymptotic state of these systems agree with the phase diagrams predictions.

Additionally, we have proposed the use of Janus particles to control these asymptotic states when in a region of the phase-space diagram that would “naturally” lead to an undesired asymptotic state. A Janus particle can act as a bridge and strengthen interactions that would be very weak otherwise. We call a ‘surfactant’ a particle that helps mix a system that would segregate otherwise and an ‘extractant’ a particle that has the opposite function, in analogy with fluids. We extend the Bond number to interactions that are bridged by Janus particles ( $Bo_{1J1}$ ) and determine, using scaling arguments, if a given system that can potentially be controlled by using Janus particles. Systems with extractant and surfactant particles were simulated. We showed how extractants can be used to induce segregation in initially mixed systems and how the use of Janus particles can improve the degree of mixture in systems that tend to segregate.

Future directions in exploiting cohesion to control mixing/segregation could explore the impact of particle-wall interactions. For example, if the particle-wall interactions ( $Bo_{i-wall}$ )

of the components ( $i = 1, 2$ ) of a granular mixture differ significantly, this difference could be used for particle separation. Following our analogy with fluids, this idea can be conceived as ‘granular chromatography’. In a simple test, a sample of particles, initially mixed, is dropped on a inclined plane and travel downhill with an average velocity that mostly depends on the angle with the horizontal and friction forces. If the wall vertically vibrates and cohesive interactions exist in the system—because of liquid bridges, for example—the interactions between the wall and the particles will determine how fast each type of particle can move downhill as well as the particle retention time. As cohesive forces (in terms of the  $Bo_{i-wall}$ ) become stronger, wall collisions will retard the traveling particles and the originally mixed sample can exit the device separated by component in increasing order of wall-cohesion interaction strength.

Another area that could be explored using a concept inspired by the physics of fluids is separation of granular material based on the ‘granular temperature’. A device that provides a ‘granular temperature gradient’ can provoke the separation of a free-flowing system. An example of such a device is one where the bottom wall of a granular bed oscillates with different amplitudes along its horizontal length. This can be achieved by pivoting one extreme while the other extreme is moved up and downwards at a certain frequency. If the wall acceleration is higher than gravity, all particles in the granular bed will be vibrated and migrate from the high amplitude (granular temperature) to the low amplitude end of the device. The traveling velocity in this case again depends on the particle properties and those particles that can reach a higher temperature will have a higher driving force and reside for a shorter time in the device.

## 7.2 HEAT TRANSFER

Many of the industrial applications of granular materials also involve heat transfer. Granular solids come into contact with cooling or heating surfaces as in processes such as drying, chemical reactions, product preservation, etc. Heat is exchanged between particles and/or particles and surfaces during their contact. The amount of heat that is being transferred

depends on the flow of granular materials: the bed conductivity is a function of its microstructure. On the other hand, heat redistribution depends on particle mixing/segregation because of the convective motion that it is associated with it. In Chapter 6, we studied the effect of the mixing rate on the heating rate of a granular material. We used the Péclet number to determine the dominant heating mechanism—conduction or convection—and to predict conditions that will favor more rapid flow of thermal energy in the granular bed. The rate of heat transport is characterized using the Nusselt number and a fluids-inspired relationship correlating this quantity with the Péclet values is attempted. A mixing continuum model is also used in this section to compare mixing patterns and temperature contours and better agreement was found for the convection dominated cases as expected.

The fact that the governing heat transfer mechanism in a system can determine macroscopic quantities such as heating rates and temperature contours calls for a more fundamental approach in our future work. The goal is to explore the effect of these mechanisms in the overall ability of a granular flow to conduct heat. Although heating and mixing tumblers are devices that have a wide industrial applicability, they limit our possibilities to control which mechanism dominates the transfer of heat. A periodic shear flow seems to be a more appropriate choice, because of the wide range of solid fractions and shear rates that are physically feasible. High shear rates and low solid fractions provide conditions where most heat should be transferred by convection—particles carry their energy as they move from one place to another—and collisions between particles are short and infrequent. In contrast, low shear rates and high solid fraction will hinder the convective movement of particles and promote frequent and long lasting collisions, suggesting that conduction should be the dominant mechanism.

For fluids, higher shear rates imply higher heat transfer rates and therefore higher effective conductivity values. In the case of conduction-dominated heat transfer, higher shear rates can cause shorter collision times and thus reduced transfer of heat. A heat transfer study in a system like this one could enable us to identify regions where the granular material behaves as a fluid (higher shear rate, higher heat transfer) from other where the opposite behavior can be observed. At the same time, the momentum fluxes can be computed. However, we do not expect that the transfer of momentum exhibit the same kind

of mechanism-dependent trend, since momentum is rapidly transferred during collisions and the amount of momentum transferred from one particle to another is independent of the duration of a collision.

### 7.3 FLOWABILITY

Another critical point for those industries that process and handle adhesive granular material is its flow properties. A common practice to improve the flowability properties of a powder is to use flow aids. These are micro or nano-sized particles that have shown in practice to have this ability. The selection of the aid particle properties is currently done mostly by trial and error. In Chapter 5, we use our  $Bo_{ij}$  tool to design and assess the performance of these particles. In order to be efficient, the interactions between the host powder that are bridged by aid particles ( $Bo_{1a1}$ ) must be significantly weaker than the interactions between host particles,  $Bo_{11}$ —although the interaction  $Bo_{1a}$  is also preferably stronger than  $Bo_{11}$ . Under this criteria, we selected and simulated systems with and without aids and assessed their flowability in terms of their angle of repose. The static angle of repose was measured in the remaining heaps after hopper discharge and the dynamic case in a rotating tumbler. Systems with low value of  $Bo_{1a1}/Bo_{11}$  were shown to have improved flow properties with respect to those cases of high  $Bo_{1a1}/Bo_{11}$  and those containing no aids.

## APPENDIX

### NOTATION

#### English symbols

---

$a$	radius of the contact area
$A$	Hamaker constant
$A_E, B_E$	major and minor semixes of the geometry
$A_r$	rotation matrix
$A_T$	area heat transfer
$\bar{B}$	ellipse aspect ratio
$Bo, Bo_{vdw}$	granular bond number
$c$	specific heat capacity
$C$	particle concentration
$C_0$	fitting parameter
$d_p$	particle diameter
$D_0$	interfacial contact separation
$E^*$	effective Young's modulus
$f$	tumbler filling level
$F$	force magnitude
$F^*$	peeling/sliding force criteria
$F_c$	pull-off force
$F_1$	equivalent hertzian force
$\vec{F}$	contact force between particles
$g, \vec{g}$	gravity
$G^*$	effective shear modulus

## English symbols

---

$h_T$	heat transfer coefficient
$H_C$	thermal conductance
$H_{CPP}$	thermal conductance between particles
$H_{CWP}$	thermal conductance between a particle and tumbler wall
$I_p$	particle moment of inertia
$k$	thermal conductivity
$k_n, k_t$	normal/tangential adhesive stiffness
$k_{mix}$	mixing constant
$L$	shear layer length
$\bar{L}$	dimensionless shear layer length
$m_p$	particle mass
$n$	number of particles
$N$	number of concentration measurements
$Pe$	Péclet number
$q_0, q_1, q_2, q_3$	quaternion components
$Q$	quaternion
$Q_{ij}$	heat flux between particles $i$ and $j$
$R^*$	effective particle radius
$\vec{R}$	lever arm vector
$t$	time
$t_{mix}$	mixing time
$T$	bed temperature
$T_W$	temperature at the wall
$F_t^*, F_t^{**}$	tangential force at the 1 <sup>st</sup> and 2 <sup>nd</sup> load reverse points
$\bar{v}_x, \bar{v}_y, \bar{v}_z$	dimensionless velocity
$\vec{v}_p$	particle velocity
$V_B$	volume granular bed
$W$	weight
$x, y, z$	space coordinates
$\bar{x}, \bar{y}, \bar{z}$	dimensionless space coordinate

## Greek symbols

---

$\alpha$	particle density ratio
$\alpha_T$	thermal diffusivity
$\beta$	particle size ratio
$\Gamma, \Gamma_{ij}$	surface energy
$\delta$	tangential displacement
$\epsilon_0$	interatomic equilibrium distance
$\varepsilon$	solid fraction
$\zeta$	shear layer thickness
$\eta$	normal approach
$\theta$	tangential force flag
$\vartheta$	rotation angle
$\kappa$	maximum midlayer thickness
$\lambda$	characteristic length
$\mu$	friction coefficient
$\mu_T$	Tabor parameter
$\nu$	Poisson ratio
$\xi$	free surface angle
$\rho$	density
$\sigma$	standard deviation
$\sigma_y$	yield stress
$\nu$	phase angle
$\phi$	surface energy ratio
$\phi_e, \theta_e, \psi_e$	Euler angles
$\omega_p, \vec{\omega}_p$	particle angular velocity
$\Omega$	tumbler rotation speed
$\mathfrak{R}_1, \mathfrak{R}_2, \mathfrak{R}_3$	bond number ratio

## Subscripts and superscripts

---

<i>a</i>	aid particle
<i>e, p</i>	elastic, plastic
<i>ff</i>	free-flowing
<i>J</i>	Janus particle
<i>L, U, R</i>	loading, unloading and reloading
<i>ma</i>	more adhesion
<i>max</i>	maximum value
<i>n, t</i>	normal, tangential
<i>old</i>	previous time step
<i>P</i>	point of contact breakage
<i>S</i>	pure solid material
<i>W</i>	tumbler wall
<i>y</i>	yield point

## Abbreviations

---

AOR	Angle of repose
DEM	Discrete Element Method
<i>DMT</i>	B. Derjaguin, V. Muller and Y. Toporov theory [75]
<i>IS</i>	Intensity of Segregation
<i>JKR</i>	K. L. Johnson, K. Kendall and A. D. Robert theory [74]
PD	Particle Dynamics
TPD	Thermal Particle Dynamics

## BIBLIOGRAPHY

- [1] R. M. Nedderman. *Statics and Kinematics of Granular Materials*. Cambridge University Press, 1992.
- [2] K. Gotoh. *Powder Technology Handbook*. Marcel Dekker, Inc., New York, second edition, 1997.
- [3] F. J. Muzzio, C. L. Goodridge, A. Alexander, P. Arratia, H. Yang, O. Sudah, and G. Mergen. Sampling and characterization of pharmaceutical powders and granular blends. *International Journal of Pharmaceutics*, 250:51–64, 2003.
- [4] P. P. Thomas and Y. B. G. Varma. Fluidised bed frying of granular floe. *Powder Technology*, 69:213–222, 1992.
- [5] Dennis R. Van Puyvelde. Simulating the mixing and segregation of solids in the transverse section of a rotating kiln. *Powder Technology*, 164:1–12, 2005.
- [6] A. Ngadi and J. Rajchenbach. Intermittencies in the compression process of a model granular medium. *Phys. Rev. Lett.*, 80(2):273–276, Jan 1998.
- [7] K. M. Hill, D. V. Khakhar, J. F. Gilchrist, J. J. McCarthy, and J. M. Ottino. Segregation-driven organization in chaotic granular flows. *PNAS*, 96:11701–11706, 1999.
- [8] H. A. Makse, S. Havlin, P. R. King, and H. E. Stanley. Spontaneous stratification in granular mixtures. *Nature*, 386:379–381, 1997.
- [9] J. T. Jenkins and S. B. Savage. A theory for the rapid flow of identical, smooth, nearly elastic spherical particles. *J. Fluid Mech.*, 130:187–202, 1983.
- [10] S. B. Savage and D. J. Jeffrey. The stress tensor in a granular flow at high shear rates. *Journal of Fluid Mechanics Digital Archive*, 110(-1):255–272, 1981.
- [11] M. L. Hunt and S. S. Hsiau. Thermal conductivity of granular flows. *Heat Transfer*, 5:177–182, 1990.
- [12] S. S. Hsiau and M. L. Hunt. Kinetic theory analysis of flow-induced particle diffusion and thermal conduction in granular material flows. *J. Heat Trans.*, 115:541–548, 1993.

- [13] D. Gidaspow. Collisional viscosity of FCC particles in a CFB. *AIChE Journal*, 42(9):2503–2510, 1996.
- [14] D. Gidaspow. *Multiphase Flow and Fluidization: Continuum and Kinetic Theory Descriptions*. Academic Press, 1994.
- [15] P. Tang and V. M. Puri. Methods for minimizing segregation: A review. *Particulate Science and Technology*, 22:321–337, 2004.
- [16] S. B. Savage and C. K. K. Lun. Particle size segregation in inclined chute flow of cohesionless granular solids. *J. Fluid Mech.*, 189:311–335, 1988.
- [17] J. B. Knight, H. M. Jaeger, and S. R. Nagel. Vibration-induced size separation in granular media: The convection connection. *Phys. Rev. Lett.*, 70:3728–3730, 1993.
- [18] J. M. Ottino and R. M. Lueptow. Materials science - On mixing and demixing. *Science*, 319:912–913, 2008.
- [19] H. M. Jaeger and S. R. Nagel R. P. Behringer. Granular solids, liquids and gases. *Rev. Mod. Phys.*, 68:1259–1273, 1996.
- [20] C. Srinivasakannan and N. Balasubramanian. An analysis on modeling of fluidized bed drying of granular material. *Advanced Powder Technology*, 19(1):73 – 82, 2008.
- [21] Z. Hui Wang and G. Chen. Heat and mass transfer in batch fluidized-bed drying of porous particles. *Chemical Engineering Science*, 55(10):1857–1869, 2000.
- [22] F. Di Natale, A. Lancia, and R. Nigro. A single particle model for surface-to-bed heat transfer in fluidized beds. *Powder Technology*, 187(1):68 – 78, 2008.
- [23] Y. Behjat, S. Shahhosseini, and S. H. Hashemabadi. CFD modeling of hydrodynamic and heat transfer in fluidized bed reactors. *International Communications in Heat and Mass Transfer*, 35(3):357–368, 2008.
- [24] A. Schmidt and U. Renz. Numerical prediction of heat transfer in fluidized beds by a kinetic theory of granular flows. *International Journal of Thermal Sciences*, 39(9-11):871–885, 2000.
- [25] Z. F. Sun, C. G. Carrington, J. A. Anderson, and Q. Sun. Air flow patterns in dehumidifier wood drying kilns. *Chemical Engineering Research and Design*, 82(10):1344 – 1352, 2004.
- [26] Z. F. Sun, C. G. Carrington, and P. Bannister. Dynamic modelling of the wood stack in a wood drying kiln. *Chemical Engineering Research and Design*, 78(1):107 – 117, 2000.
- [27] G. R. S. Wildhagen, L. A. Calcada, and G. Massarani. Drying of porous particles in fluidized beds: modeling and experiments. *J. Porous Media*, 2:123–133, 2002.

- [28] P. Porion, N. Sommer, A. M. Faugere, and P. Evesque. Dynamics of size segregation and mixing of granular materials in a 3d-blender by nmr imaging investigation. *Powder Technology*, 141(1-2):55–68, 2004.
- [29] B. Voglauer and H. P. Jörgl. Dynamic model of a roast process for simulation and control. *Mathematical and Computer Modelling of Dynamical Systems*, 10(3/4):217–230, 2004.
- [30] M. D. Heydenrych, P. Greeff, A. B. M. Heesink, and G. F. Versteeg. Mass transfer in rolling rotary kilns: a novel approach. *Chemical Engineering Science*, 57(18):3851–3859, 2002.
- [31] P. S. Ghoshdastidar, G. Bhargava, and R. P. Chhabra. Computer simulation of heat transfer during drying and preheating of wet iron ore in a rotary kiln. *Drying Technology*, 20(1):19, 2002.
- [32] A. R. Khan and A. Elkamel. Mathematical model for heat transfer mechanism for particulate system. *Appl. Math. Comput.*, 2-3:295–316, 2002.
- [33] R. A. Dekhtyar, D. P. Sikovsky, A. V. Gorine, and V. A. Mukhin. Heat transfer in a packed bed at moderate values of the Reynolds number. *High Temp. USSR*, 5(693–700), 2002.
- [34] B. Peters, E. Schroder, C. Bruch, and T. Nussbaumer. Measurements and particle resolved modelling of heatup and drying of a packed bed. *Biomass Bioenergy*, 23:291–306, 2002.
- [35] E. U. Schlünder. Heat transfer to moving spherical packings at short contact times. *International Chemical Engineering*, 20:550–554, 1980.
- [36] Y. L. Ding, R. N. Forster, J. P. K. Seville, and D. J. Parker. Some aspects of heat transfer in rolling mode rotating drums operated at low to medium temperatures. *Powder Technology*, 121:168–181, 2001.
- [37] T. Shinbrot and F. J. Muzzio. Nonequilibrium patterns in granular mixing and segregation. *Physics Today*, 53(3):25, 2000.
- [38] J. M. Ottino and D. V. Khakhar. Fundamental research in heaping, mixing, and segregation of granular materials: challenges and perspectives. *Powder Technology*, 121:117–122, 2001.
- [39] J. P. Bardet. Introduction to computational granular mechanics. In B. Cambou, editor, *Behavior of granular materials*, pages 99–169. Springer-Verlag, 1998.
- [40] C. S. Campbell. Rapid granular flows. *Ann. Rev. Fluid Mech.*, 22:57–90, 1990.
- [41] H. J. Herrmann and S. Luding. Modeling granular media on the computer. *Continuum Mech. Thermodyn.*, 10:189–231, 1998.

- [42] Y. Kaneko, T. Shiojima, and M. Horio. Dem simulation of fluidized beds for gas-phase olefin polymerization. *Chemical Engineering Science*, 54:5809–5821, 1999.
- [43] K. Kuwagi, T. Mikami, and M. Horio. Numerical simulation of metallic solid bridging particles in a fluidized bed at high temperature. *Powder Technology*, 109 (1):27–40, 2000.
- [44] M. Satake. Constitution of mechanics of granular materials through the graph theory. In S.C. Cowin and M. Satake, editors, *U.S.-Japan Seminar in Continuum Mechanics and Statistical Approaches in the Mechanics of Granular Materials*, pages 47–62, 1978.
- [45] T. Ng and E. Petrakis. Small-strain response of random arrays of spheres using discrete element method. *J. Eng. Mech.*, 122:239–244, 1996.
- [46] Q. M. Tai and M. H. Sadd. A discrete element study of the relationship of fabric to wave propagational behaviours in granular material. *Int. J. Numer. Anal. Meth. Geomech.*, 21:295–311, 1997.
- [47] C. Thornton. Numerical simulations of deviatoric shear deformation of granular media. *Geotechnique*, 50:43–53, 2000.
- [48] C. Thornton. Numerical simulations of discrete particle systems. *Powder Technology*, 109(2):2, 2000.
- [49] C. Thornton and C. W. Randall. Applications of theoretical contact mechanics to solid particle system simulation. In M. Satake and J. T. Jenkins, editors, *Micromechanics of Granular Material*, pages 133–142. Elsevier Science Publishers, Amsterdam, 1988.
- [50] Y. Tsuji, T. Kawaguchi, and T. Tanaka. Discrete particle simulation of two-dimensional fluidized bed. *Powder Technology*, 77:79–87, 1993.
- [51] O. R. Walton and R. L. Braun. Viscosity, granular-temperature, and stress calculations for shearing assemblies of inelastic, frictional disks. *J. Rheol.*, 30:949–980, 1986.
- [52] K. Z. Y. Yen and T. K. Chaki. A dynamic simulation of particle rearrangement in powder packings with realistic interactions. *Journal of Applied Physics*, 71:3164–3173, 1992.
- [53] C. Thornton. Force transmission in granular media. *KONA*, 15:81–90, 1997.
- [54] C. Thornton, K. K. Yin, and M. J. Adams. Numerical simulation of the impact fracture and fragmentation of agglomerates. *Journal of Physics D: Applied Physics*, 29:424–435, 1996.
- [55] D. V. Khakhar, J. J. McCarthy, and J. M. Ottino. Radial segregation of granular materials in rotating cylinders. *Phys. Fluids*, 9:3600–3614, 1997.

- [56] C. S. Campbell. Computer simulation of rapid granular flows. *Proc. US Natl. Congr. Appl. Mech. 10th*, 10:327–338, 1986.
- [57] P. A. Cundall and O. D. L. Strack. A discrete numerical model for granular assemblies. *Géotechnique*, 29:47–65, 1979.
- [58] J. Lee and H. J. Herrmann. Angle of repose and angle of marginal stability: molecular dynamics of granular particles. *Journal of Physics A*, 26:373–383, 1993.
- [59] J. T. Oden and J. A. C. Martins. Computer methods for dynamic friction phenomena. *Computer Methods in Applied Mechanics and Engineering*, 1984.
- [60] C. Thornton. Coefficient of restitution for collinear collisions of elasti-perfectly plastic spheres. *Journal of Applied Mechanics*, 64:383–386, 1997.
- [61] H. Hertz. Ueber die berührungsfester elastischer körper. *J. reine ange. Math.*, 92:1–15, 1881.
- [62] C. Thornton. Coefficient of restitution for collinear collisions of elasti-perfectly plastic spheres. *J. Appl. Mech.*, 64:383–386, 1997.
- [63] O. R. Walton. Numerical simulation of inclined chute flows of monodisperse, inelastic, frictional spheres. *Mech. Mat.*, 16:239–247, 1993.
- [64] R. D. Mindlin. Compliance of elastic bodies in contact. *J. Appl. Mech.*, 16:256–270, 1949.
- [65] B. Chaudhuri, A. Mehrotra, F. J. Muzzio, and M. S. Tomassone. Cohesive effects in powder mixing in a tumbling blender. *Powder Technology*, 165(2):105–114, 2006.
- [66] M. W. Weber and C. M. Hrenya. Square-well model for cohesion in fluidized beds. *Chemical Engineering Science*, 61(14):4511 – 4527, 2006.
- [67] A. W. Alexander, B. Chaudhuri, A. Faqih, F. J. Muzzio, Clive Davies, and M. S. Tomassone. Avalanching flow of cohesive powders. *Powder Technology*, 164(1):13–21, 2006.
- [68] M. A. Gilbertson and I. Eames. The influence of particle size on the flow of fluidised powders. *Powder Technology*, 131(2-3):197–205, 2003.
- [69] M. J. Rhodes, X. S. Wang, M. Nguyen, P. Stewart, and K. Liffman. Onset of cohesive behaviour in gas fluidized beds: a numerical study using dem simulation. *Chemical Engineering Science*, 56(14):4433–4438, 2001.
- [70] D. Geldart. Types of gas fluidization. *Powder Technology*, 7(285–292), 1973.
- [71] P. G. Rognon, J. N. Roux, D. Wolf, M. Naaim, and F. Chevoir. Rheophysics of cohesive granular materials. *EPL (Europhysics Letters)*, 74(4):644–650, 2006.

- [72] R. Brewster, G. S. Grest, J. W. Landry, and A. J. Levine. Plug flow and the breakdown of bagnold scaling in cohesive granular flows. *Phys. Rev. E*, 72(6):061301, 2005.
- [73] B. L. Severson, L. M. Keer, J. M. Ottino, and R. Q. Snurr. Mechanical damping using adhesive micro or nano powders. *Powder Technology*, 191(1-2):143–148, 2009.
- [74] K. L. Johnson, K. Kendall, and A. D. Robert. Surface energy and the contact of elastic solids. *Proceedings of the Royal Society of London, A*, 324:301–313, 1971.
- [75] B. V. Derjaguin, V. M. Muller, and Y. U. P. Toporov. Effect of contact deformation on the adhesion of particles. *Journal of colloid and interface science*, 52:105–108, 1975.
- [76] D. Tabor. Surface forces and surface interactions. *Journal of Colloid and Interface Science*, 58:2–13, 1977.
- [77] G. V. Dedkov. Experimental and theoretical aspects of the modern nanotribology. *Phys. Stat. Sol. (a)*, 179:3–75, 2000.
- [78] J. N. Israelachvili. *Intermolecular and Surface Forces*. Academic Press, 1991.
- [79] A. R. Savkoor and G. A. D. Briggs. The effect of tangential force on the contact of elastic solids in adhesion. *Proc. R. Soc. Lond. A*, 356:103–114, 1977.
- [80] C. Thornton and K. K. Yin. Impact of elastic spheres with and without adhesion. *Powder Technology*, 65:153–166, 1991.
- [81] C. Thornton and Z. Ning. A theoretical model for the stick/bounce behavior of adhesive, elastic-plastic spheres. *Powder Technology*, 99:154–162, 1998.
- [82] K. K. Yin. *Numerical modelling of agglomerate degradation*. PhD thesis, The University of Aston in Birmingham, 1992.
- [83] J. Sun and M. M. Chen. A theoretical analysis of heat transfer due to particle impacts. *Int. J. Heat Mass Transfer*, 31:969–975, 1988.
- [84] W. L. Vargas and J. J. McCarthy. Heat conduction in granular materials. *AIChE Journal*, 47:1052–1059, 2001.
- [85] W. L. Vargas. *Discrete Modeling of Heat Conduction in Granular Media*. PhD thesis, Pitt, 2002.
- [86] W. L. Vargas and J. J. McCarthy. Conductivity of granular media with stagnant interstitial fluids via thermal particle dynamics simulation. *International Journal of Heat and Mass Transfer*, 45:4847–4856, 2002.
- [87] Y. Tsuji, T. Tanaka, and T. Ishida. Lagrangian numerical simulation of plug flow of cohesionless particles in a horizontal pipe. *Powder Technology*, 71:239–250, 1992.

- [88] J. Li and D. J. Mason. A computational investigation of transient heat transfer in pneumatic transport of granular particles. *Powder Technology*, 112:273–282, 2000.
- [89] B. Chaudhuri, F. J. Muzzio, and M. S. Tomassone. Modeling of heat transfer in granular flow in rotating vessels. *Chemical Engineering Science*, 61:6348–6360, 2006.
- [90] Y. Shimizu. Three-dimensional simulation using fixed coarse-grid thermal-fluid scheme and conduction heat transfer scheme in distinct element method. *Powder Technology*, 165:140–152, 2006.
- [91] D. Shi, W. L. Vargas, and J. J. McCarthy. Heat transfer in rotary kilns with interstitial gases. *Chemical Engineering Science*, 63:4506–4516, 2008.
- [92] A. Dziugys and B. Peters. An approach to simulate the motion of spherical and non-spherical fuel particles in combustion chambers. *Granular Matter*, 3:231–265, 2001.
- [93] P. A. Langston, M.A. Al-Awamleh, F. Y. Fraige, and B. N. Asmar. Distinct element modelling of non-spherical frictionless particle flow. *Chemical Engineering Science*, 59:425–435, 2004.
- [94] L. Meister and H. Schaeben. A concise quaternion geometry of rotations. *Mathematical Methods in the Applied Sciences*, 28:101–126, 2005.
- [95] D. Evans. On the representation of orientation space. *Molecular Physics*, 34:317–325, 1977.
- [96] D. Evans and S. Murad. Singularity free algorithm for Molecular Dynamics simulation of rigid polyatomics. *Molecular Physics*, 34:327–331, 1977.
- [97] S. R. De Silva, A. Dyroy, and G. G. Enstad. Segregation mechanism and their quantification using segregation testers. In A. D. Rosato and D. L. Blackmore, editors, *Segregation in Granular Flows*, IUTAM Symposium Series, pages 11–29. Kluwer Academic Press, 2000.
- [98] A. C. Hoffmann, L. P. B. M. Janssen, and J. Prins. Particle segregation in fluidised binary mixtures. *Chem. Eng. Sci.*, 48:1583–1592, 1993.
- [99] W. Pietsch. *Agglomeration Processes: Phenomena, Technologies, Equipment*. WILEY-VCH, 2002.
- [100] H. Venables and J. Wells. Powder mixing. *Drug Development and Industrial Pharmacy*, 27(7):599–, 2001.
- [101] J. C. Williams and M. I. Khan. The mixing and segregation of particulate solids of different particle size. *Chem. Eng.*, 269:19–25, 1973.
- [102] J. Mosby, S. R. de Silva, and G. G. Enstad. Segregation of particulate materials—Mechanisms and testers. *KONA*, 14:31–42, 1996.

- [103] J. A. Drahn and J. Bridgwater. The mechanisms of free surface segregation. *Powder Technology*, 36(1):39 – 53, 1983.
- [104] J. F. G. Harris and A. M. Hildon. Reducing segregation in binary powder mixtures with particular reference to oxygenated washing powders. *Industrial & Engineering Chemistry Process Design and Development*, 9(3):363–367, 2002.
- [105] J. R. Johanson. Predicting segregation of bimodal particle mixtures using the flow properties of bulk solid. *Pharm. Technol. Eur.*, 8(1):38–44, 1996.
- [106] H. Li and J.J McCarthy. Controlling cohesive particle mixing and segregation. *Phys. Rev. Lett.*, 90:184301, 2003.
- [107] K. Clague and H. Wright. Minimizing segregation in bunkers. *J. Eng. Ind. (B)*, 95(1):81–85, 1973.
- [108] K. Shinohara. *Powder Technology Handbook*, volume Segregation of particles. New York: Marcel Dekker, 1997.
- [109] T. W. Garve. Segregation in bins. *J. Am. Ceram. Soc.*, 8:666, 1925.
- [110] H. M. Peacock. The design or adaptation of storage bunkers to prevent size segregation of solids. *J. Instit. Fuel.*, 11:230–239, 1938.
- [111] J. K. Prescott and R. J. Hossfield. Maintaining product uniformity and uninterrupted flow to direct-compression tableting presses. *Pharm. Technol.*, 18:99–114, 1994.
- [112] L. Bates. *User Guide to Segregation*. Cheshire, U.K.; British Materials Handling Board, 1998.
- [113] J. F. Van Denburg and W. C. Bauer. Segregation of particles in the storage of materials. *Chem. Eng.*, pages 135–142, 1964.
- [114] Deliang Shi, Adetola A. Abatan, Watson L. Vargas, and J. J. McCarthy. Eliminating segregation in free-surface flows of particles. *Physical Review Letters*, 99:148001, 2007.
- [115] D. V. Khakhar, J. J. McCarthy, and J. M. Ottino. Mixing and segregation of granular materials in chute flows. *Chaos*, 9:594–610, 1999.
- [116] J. A. Hersey. Ordered mixing: A new concept in powder mixing practice. *Pow. Technol.*, 11:41–44, 1975.
- [117] A. Samadani and A. Kudrolli. Segregation transitions in wet granular matter. *Phys. Rev. Lett.*, 85:5102–5105, 2000.
- [118] D. Geromichalos, M. M. Kohonen, F. Mugele, and S. Herminghaus. Mixing and condensation in a wet granular medium. *Physical Review Letters*, 90:168702, 2003.

- [119] S. S. Hsiau and S. C. Yang. Numerical simulation of self-diffusion and mixing in a vibrated granular bed with the cohesive effect of liquid bridges. *Chemical Engineering Science*, 58(2):339–351, 2003.
- [120] S. R. Hutton, A. J. Forsyth, M. J. Rhodes, and C. F. Osborne. Effect of interparticle force on mixing and segregation of dry granular materials. *Physical Review E (Statistical, Nonlinear, and Soft Matter Physics)*, 70(3):031301, 2004.
- [121] P. V. Danckwerts. The definition and measurement of some characteristics of mixtures. *Appl. Sci. Res.*, A3:279–296, 1952.
- [122] J. M. Ottino. *The kinematics of mixing: stretching, chaos, and transport*. Cambridge University Press, New York, 1989.
- [123] D. V. Khakhar, J. J. McCarthy, J. F. Gilchrist, and J. M. Ottino. Chaotic mixing of granular materials in two-dimensional tumbling mixers. *Chaos*, 9:195–205, 1999.
- [124] H. Li and J. J. McCarthy. Phase diagrams for cohesive particle mixing and segregation. *Physical Review E*, 71:021305, 2005.
- [125] A. Samadani and A. Kudrolli. Angle of repose and segregation in cohesive granular matter. *Physical Review E*, 64(5), 2001.
- [126] K. L. Johnson. *Contact Mechanics*. Cambridge University Press, Cambridge, 1987.
- [127] R. D. Mindlin and H. Deresiewicz. Compliance of elastic bodies in contact. *J. Appl. Mech.*, 20:327, 1953.
- [128] H. Li and J. J. McCarthy. Cohesive particle mixing and segregation under shear. *Powder Technology*, 164:58–64, 2006.
- [129] O. Walton. Application of molecular dynamics to macroscopic particles. *International Journal of Engineering Science*, 22:1097–1107, 1984.
- [130] K. Jain, D. Shi, and J. J. McCarthy. Discrete characterization of cohesion in gas-solid flows. *Powder Technol.*, 146(1):160–167, 2004.
- [131] J. Visser. An invited review: Van der waals and other cohesive forces affecting powder fluidization. *Powder Technology*, 58:1–10, 1989.
- [132] I. Figueroa, H. Li, and J. J. McCarthy. Predicting the impact of adhesive forces on particle mixing and segregation. *Powder Technology*, 195(3):203–212, 2009.
- [133] J. P. K. Seville, U. Tüzün, and R. Clift. *Processing of Particulate Solids*. Blackie Academic and Professional, London, 1997.
- [134] E. C. Abdullah and D. Geldart. The use of bulk density measurements as flowability indicators. *Powder Technology*, 102(2):151–165, 1999.

- [135] H. H. Hausner. Friction conditions in a mass of metal powder. *International Journal of Powder Metallurgy*, 3:7–13, 1967.
- [136] A. Dutta and L.V. Dullea. Comparative evaluation of negatively and positively charged submicron particles as flow conditioners for a cohesive powder. volume 86, pages 26–40, 1990.
- [137] H. Abe, S. Yasui, A. Kuwata, and H. Takeuchi. Improving powder flow properties of a direct compression formulation using a two-step glidant mixing process. *Chemical & Pharmaceutical Bulletin*, 57:647–652, 2009.
- [138] G. Gold, R. N. Duvall, B. T. Palermo, and J. G. Slater. Powder flow studies ii. Effect of glidants on flow rate and angle of repose. *Journal of Pharmaceutical Sciences*, 55(11):1291–1295, 1966.
- [139] S. Jonat, S. Hasenzahl, A. Gray, and P. C. Schmidt. Mechanism of glidants: Investigation of the effect of different colloidal silicon dioxide types on powder flow by atomic force and scanning electron microscopy. *Journal of Pharmaceutical Sciences*, 93:2635–2644, 2004.
- [140] C. C. Lai, S. G. Gilbert, and C. H. Mannheim. Effect of flow conditioners on water sorption and flow properties of egg powder. *Journal of Food Engineering*, 5(4):321–333, 1986.
- [141] H. O. Kono, C. C. Huang, and M. Xi. Function and mechanism of flow conditioners under various loading pressure conditions in bulk powders. *Powder Technology*, 63(1):81–86, 1990.
- [142] P. York. The use of glidants to improve the flowability of fine lactose powder. *Powder Technology*, 11(2):197 – 198, 1975.
- [143] D. W. Howell, R. P. Behringer, and C. T. Veje. Fluctuations in granular media. *Chaos: An Interdisciplinary Journal of Nonlinear Science*, 9(3):559–572, 1999.
- [144] T. S. Majmudar and R. P. Behringer. Contact force measurements and stress-induced anisotropy in granular materials. *Nature*, 435(1079):1079–1082, 2005.
- [145] W. L. Vargas and J. J. McCarthy. Stress effects on the conductivity of particulate beds. *Chemical Engineering Science*, 57:3119–3131, 2002.
- [146] A. A. Boateng and P. V. Barr. Granular flow behaviour in the transverse plane of a partially filled rotating cylinder. *Journal of Fluid Mechanics*, 330:233–249, 1997.
- [147] S. B. Savage. Analyses of slow high-concentration flows of granular materials. *Journal of Fluid Mechanics*, 377(-1):1–26, 1998.
- [148] J. S. M. Botterill. *Fluid-bed heat transfer*. Academic Press, N. Y., 1975.

- [149] O. Molerus. Heat transfer in moving beds with a stagnant interstitial gas. *International Journal of Heat and Mass Transfer*, 40:4151–4159, 1997.
- [150] M. Kwapinska, G. Saage, and E. Tsotsas. Continuous versus discrete modelling of heat transfer to agitated beds. *Powder Technology*, 181:331–342, 2008.
- [151] J. Mu and D. D. Perlmutter. The mixing of granular solids in a rotary cylinder. *AIChEJ*, 26:928–934, 1980.
- [152] R. Hogg and D. W. Fuerstenau. Transverse mixing in rotating cylinders. *Powder Technology*, 6:139–147, 1972.
- [153] R. Hogg, G. Mempel, and D. W. Fuerstenau. The mixing of trace quantities into particulate solids. *Powder Technology*, 2:223–228, 1968/69.
- [154] A. A. Boateng and B. V. Barr. Modelling of particle mixing and segregation in the transverse plane of a rotary kiln. *Chemical Engineering Science*, 51(17):4167–4181, 1996.
- [155] G. J. Finnie, N.P. Kruyt, M. Ye, C. Zeilstra, and J. A. M. Kuipers. Longitudinal and transverse mixing in rotary kilns: A discrete element method approach. *Chemical Engineering Science*, 60:4083–4091, 2005.
- [156] K. M. Hill, J. F. Gilchrist, J. M. Ottino, D. V. Khakhar, and J. J. McCarthy. Mixing of granular materials a test-bed dynamical system for pattern formation. *International J. of Bifurcation and Chaos*, 9:1467–1484, 1999.
- [157] N. Jain, J. M. Ottino, and R. M. Lueptow. Regimes of segregation and mixing in combined size and density granular systems: An experimental study. *Granular Matter*, 7:69–81, 2005.
- [158] S. E. Cisar, P. B. Umbanhowar, and J. M. Ottino. Radial granular segregation under chaotic flow in two-dimensional tumblers. *Phys. Rev. E*, 73:031304, 2006.
- [159] J. J. McCarthy, T. Shinbrot, G. Metcalfe, J. E. Wolf, and J. M. Ottino. Mixing of granular materials in slowly rotated containers. *AIChE Journal*, 42:3351–3363, 1996.
- [160] D. V. Khakhar, J. J. McCarthy, T. Shinbrot, and J. M. Ottino. Transverse flow and mixing of granular materials in a rotating cylinder. *Phys. Fluids*, 9:31–43, 1997.
- [161] J. Lehmberg, M. Hehl, and K. Schügerl. Transverse mixing and heat transfer in horizontal rotary drum reactors. *Powder Technology*, 18:149–163, 1977.
- [162] E. U. Schlünder. Heat transfer to packed and stirred beds from the surface of immersed bodies. *Chem. Eng. Process*, 18:31–53, 1984.